

PL-TR-93-2070

AD-A265 035



2

QUANTIFICATION OF m_{Lg} FOR SMALL EXPLOSIONS

R. B. Herrmann
K. Hutchensen

Department of Earth and Atmospheric Sciences
St. Louis University
3507 Laclede Avenue
St. Louis, MO 63103

12 March 1993

Final Report
July 5, 1990 - December 31, 1992



Approved for public release; distribution unlimited

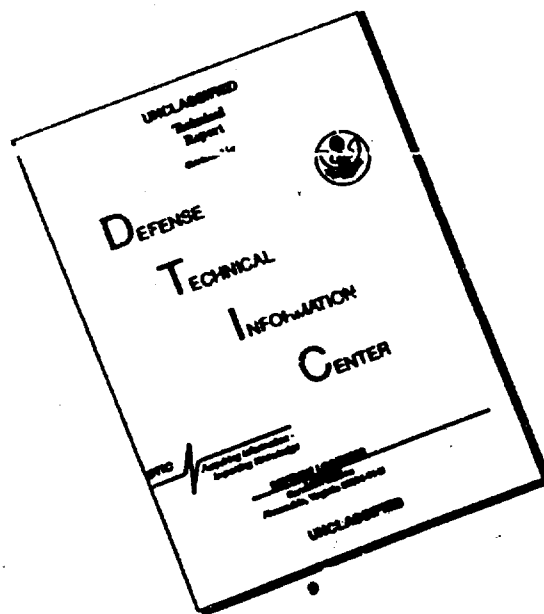
93 5 20 029

93-11320



PHILLIPS LABORATORY
Directorate of Geophysics
AIR FORCE MATERIEL COMMAND
HANSCOM AIR FORCE BASE, MA 01731-3010

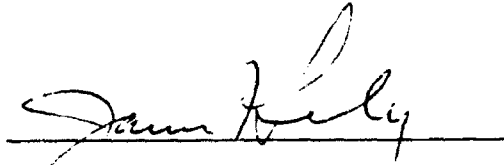
DISCLAIMER NOTICE



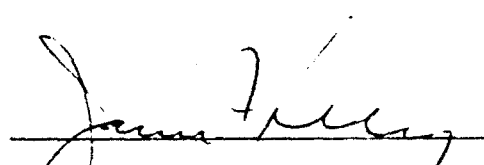
THIS DOCUMENT IS BEST
QUALITY AVAILABLE. THE COPY
FURNISHED TO DTIC CONTAINED
A SIGNIFICANT NUMBER OF
PAGES WHICH DO NOT
REPRODUCE LEGIBLY.

The views and conclusions contained in this document are those of the authors and should not be interpreted as representing the official policies, either expressed or implied, of the Air Force or the U.S. Government.

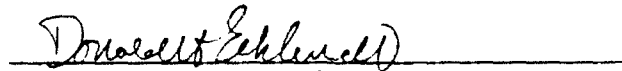
This technical report has been reviewed and is approved for publication.



JAMES F. LEWKOWICZ
Contract Manager
Solid Earth Geophysics Branch
Earth Sciences Division



JAMES F. LEWKOWICZ
Branch Chief
Solid Earth Geophysics Branch
Earth Sciences Division


DONALD H. ECKHARDT, Director
Earth Sciences Division

This document has been reviewed by the ESD Public Affairs Office (PA) and is releasable to the National Technical Information Service (NTIS).

Qualified requestors may obtain additional copies from the Defense Technical Information Center. All others should apply to the National Technical Information Service.

If your address has changed, or if you wish to be removed from the mailing list, or if the addressee is no longer employed by your organization, please notify PL/TSI, Hanscom AFB MA 01731-3010. This will assist us in maintaining a current mailing list.

Do not return copies of this report unless contractual obligations or notices on a specific document requires that it be returned.

REPORT DOCUMENTATION PAGE			Form Approved OMB No. 0704-0188	
<small>Public reporting burden for this collection of information is estimated to average 1 hour per response, including the time for reviewing instructions, searching existing data sources, gathering and maintaining the data needed, and completing and reviewing the collection of information. Send comments regarding this burden estimate or any other aspect of this collection of information, including suggestions for reducing this burden, to Washington Headquarters Services, Directorate for Information Operations and Reports, 1215 Jefferson Davis Highway, Suite 1204, Arlington, VA 22202-4302, and to the Office of Management and Budget, Paperwork Reduction Project (0704-0188), Washington, DC 20503.</small>				
1. AGENCY USE ONLY (Leave blank)	2. REPORT DATE 12 March 1993	3. REPORT TYPE AND DATES COVERED Final Report (5 July 1990-31 Dec 1992)		
4. TITLE AND SUBTITLE Quantification of m_{Lg} for Small Explosions		5. FUNDING NUMBERS PE 62101F PR 7600 TA 09 WU BC Contract F19628-90-K-0040		
6. AUTHOR(S) R. B. Herrmann K. Hutchensen				
7. PERFORMING ORGANIZATION NAME(S) AND ADDRESS(ES) Department of Earth and Atmospheric Sciences Saint Louis University 3507 Laclede Avenue St. Louis, MO 63103		8. PERFORMING ORGANIZATION REPORT NUMBER		
9. SPONSORING/MONITORING AGENCY NAME(S) AND ADDRESS(ES) Phillips Laboratory 29 Randolph Road Hanscom AFB, MA 01731-3010 Contract Manager: James Lewkowicz/GPIEH		10. SPONSORING/MONITORING AGENCY REPORT NUMBER PL-TR-93-2070		
11. SUPPLEMENTARY NOTES				
12a. DISTRIBUTION / AVAILABILITY STATEMENT Approved for public release; Distribution unlimited		12b. DISTRIBUTION CODE		
13. ABSTRACT (Maximum 200 words) This report focuses on regional wave propagation with application to the discrimination problem between explosions and earthquakes. Since discrimination is not trivial for small events, understanding of seismic wave propagation and seismic sources is essential. The report begins by completely presenting seismic wave propagation theory for plane layers in an isotropic media. Topics such as propagator matrix stability, wavenumber integration and periodicity of the discrete Fourier transform are addressed. The next topic discusses the differences between small explosions and earthquakes of the same magnitude. The investigation indicates that chemical mining explosions have low excitation of high frequencies compared to point sources, such as earthquakes. Finally, the use of the short-period surface wave as a depth indicator is discussed.				
14. SUBJECT TERMS Explosions, Earthquakes, Seismic Wave Theory, Seismic Moment			15. NUMBER OF PAGES 104	
			16. PRICE CODE	
17. SECURITY CLASSIFICATION OF REPORT Unclassified	18. SECURITY CLASSIFICATION OF THIS PAGE Unclassified	19. SECURITY CLASSIFICATION OF ABSTRACT Unclassified	20. LIMITATION OF ABSTRACT SAR	

TABLE OF CONTENTS

Preface	v
Elastic Wave Green's Functions for Isotropic Layered Media	1
Introduction	1
Functional Form of the Solution	2
Wholespace Solution	7
Halfspace Solution	12
Plane Layered Media	15
Liquid Layer	22
Time Histories	29
Wavenumber Integration	34
Numerical issues in Evaluating Propagator Matrices	44
References	46
Appendix	48
 Spectral Examination of the 16 June 1992 Earthquake and Quarry Blast near Evansville, Indiana	 57
Introduction	57
Description of the Study Area	60
Data Processing and Results	60
Discussion and Conclusions	76
Acknowledgments	79
References	79
 Discourse on the Use of Short Period Surface Waves as a Depth Discriminant	 85
Introduction	85
Depth Constraints	86
Discussion	88
References	89

DEPT OF AEROSPACE AND NAUTICS

Accession For	
NTIS GRA&I	<input checked="" type="checkbox"/>
DTIC TAB	<input type="checkbox"/>
Unannounced	<input type="checkbox"/>
Justification	
By	
Distribution/	
Availability Codes	
Dist	Avail and/or Special
A-1	

(This Page Blank)

Preface

This report focuses on regional wave propagation with application to the discrimination problem between explosions and earthquakes. Since discrimination is not trivial for small events, no one single technique will resolve the problem. This implies that one must understand seismic wave propagation in all its complexity. There are limits to this both in computation and theory and in knowledge of true three dimensional real earth model.

As a step toward understanding wave propagation, the first part of this report presents a complete review of wave propagation in layered, isotropic, homogeneous media. Analytic solutions for wave generation in a wholespace due to moment tensor and point forces is given in the $r - \omega$ domain, where r is the radial distance between the source and receiver. This is followed by explicit expressions for the solution to the same problem in the $k - \omega$ domain, where k is wavenumber. The reason for these two representations is to permit validation of numerical integration techniques used to obtain time histories as a function of distance. The solutions in the $k - \omega$ domain are extended for the halfspace and a generalized layered medium. The solution to the layered media problem is given in terms of propagator matrices. The general solution permits a variety of boundary conditions at the top and bottom of the layered stack that permits the same methodology to be used for reflectivity computations of P-wave first arrivals. The subjects of wavenumber integration, propagator matrix stability and consequences of using discrete Fourier transforms are also discussed. The algorithms presented and the tutorial on their use are being used to understand regional wave propagation.

The second subject discussed partially addresses the real problems of discrimination: that of distinguishing shallow earthquakes, shallow delayed chemical explosions and shallow point explosions. The real problem is that data sets containing all three of these phenomena are not readily available. This section compares a shallow earthquake and a delayed explosion of similar magnitude near Evansville, Indiana in 1992. Differences in the two sources are seen in the P-wave spectra, where the strip mining explosions have a lower corner frequency and significantly less high frequency signal above 10 Hz results for the Lg phase are similar. This may lead to a discriminant between spatially distributed chemical explosions and point earthquake or explosion sources.

The final topic touches upon depth discriminant information contained in the Rg wave. Under the conditions of a relatively uniform waveguide and with broadband recording, the short period surface wave may be a useful quantifiable indicator of depth. The presence or absence of a short period surface wave does not give any direct depth information, unless additional

independent information is available, such as knowledge of regional velocity and Q models and absolute source size. Given these constraints a family of curves can be created to indicate the moment required to generate an observed signal of a given amplitude as a function of depth. If a suite of curves, generated under other assumptions of earth structure, is used, a "fuzzy" estimate of source depth can be made simply on the basis of whether a surface wave of a given amplitude is observed.

The implication of this research to the task of event discrimination is that a systematic attempt has been made to develop the tools for understanding regional wave propagation and for their use in analyzing events that are not confidently rejected from consideration on the basis of exhibiting strong earthquake or delayed explosion characteristics. To classify these remaining events, the entire recorded waveform must be understood. From the theoretical point of view, broadband signals above the noise level are preferred to accomplish this.

ELASTIC WAVE GREEN'S FUNCTIONS FOR ISOTROPIC LAYERED MEDIA

Robert B. Herrmann

ABSTRACT

The Haskell (1964) formulation for the elastic wave field due to point sources in a plane layered medium is revised for the purpose of generalizing the boundary conditions at the top and bottom of the layer stack and for permitting the receiver to be at any depth in the medium. Because of the usefulness and also complexity of the problem, explicit solutions are given for wholespace and halfspace problems. The numerical implementation is discussed in detail, demonstrating needed tricks to ensure quality, noise-free solutions.

INTRODUCTION

In testing seismogram synthesis programs, it is necessary to compare the program results to analytic solutions or to previous numerical solutions. This has led to several papers by the author and students at Saint Louis University (Wang and Herrmann, 1980; Herrmann and Wang, 1985; Herrmann and Mandal, 1986). These solutions were for center of expansion and double couple sources in a wholespace and in a halfspace observed at the free surface. Recently the author found it necessary to consider the case of a buried receiver, for which a stable algorithm was required. In addition closed form solutions for point forces were also required because of their use as sources in seismic exploration sources and because of interest in the non-isotropic signal associated with underground explosions. Because of the author's familiarity with the Haskell (1963, 1964) papers, this presentation will continue using that notation in a cylindrical coordinate system because of the assumption of isotropic, laterally homogeneous layering. Other representations of the solutions are possible, especially the reflectivity coefficients of Kennett (1983).

Given the assumption of a laterally homogeneous isotropic medium and because the Green's functions will be given for point sources, it is convenient to construct the solution in a cylindrical coordinate system (r, ϕ, z) and in terms of angular frequency. The specific definition of the Fourier transform, $H(\omega)$, of the time series $h(t)$ is taken to be

$$H(\omega) = \int_{-\infty}^{\infty} h(t) e^{-i\omega t} dt$$

with the inverse transform defined as

$$h(t) = \frac{1}{2\pi} \int_{-\infty}^{\infty} H(\omega) e^{i\omega t} d\omega$$

FUNCTIONAL FORM OF THE SOLUTION

Haskell (1963) built the solution for the displacement field due to point couples in a wholospace by starting with the analytic solution for the displacement field due to a point force given in a cartesian coordinate system. Solutions for point single couples were obtained, and the solution was cast into a cylindrical coordinate system, through the use of partial derivatives of the Sommerfeld integral. Haskell (1964) extended the Haskell (1963) work to a layered halfspace, including double-couple, dipole and point forces. The equations below cast the Haskell (1963) derivations into the Green's functions for dislocation and explosive sources, originally given by Herrmann and Wang (1985). The Green's functions are defined as follow:

$$ZDD = \int_0^{\infty} F_1(k, \omega) J_0(kr) dk \quad (1a)$$

$$RDD = - \int_0^{\infty} F_2(k, \omega) J_1(kr) k dk \quad (1b)$$

$$ZDS = \int_0^{\infty} F_3(k, \omega) J_1(kr) dk \quad (1c)$$

$$RDS = \int_0^{\infty} F_4(k, \omega) J_0(kr) k dk \quad (1d)$$

$$- \frac{1}{r} \int_0^{\infty} [F_4(k, \omega) + F_{13}(k, \omega)] J_1(kr) dk$$

$$TDS = \int_0^{\infty} F_{12}(k, \omega) J_0(kr) k dk \quad (1e)$$

$$- \frac{1}{r} \int_0^{\infty} [F_4(k, \omega) + F_{13}(k, \omega)] J_1(kr) dk$$

$$ZSS = \int_0^{\infty} F_5(k, \omega) J_2(kr) dk \quad (1f)$$

$$RSS = \int_0^{\infty} F_6(k, \omega) J_1(kr) k dk \quad (1g)$$

$$-\frac{2}{r} \int_0^{\infty} [F_6(k, \omega) + F_{14}(k, \omega)] J_2(kr) dk$$

$$TSS = \int_0^{\infty} F_{14}(k, \omega) J_1(kr) k dk \quad (1h)$$

$$-\frac{2}{r} \int_0^{\infty} [F_6(k, \omega) + F_{14}(k, \omega)] J_2(kr) dk$$

$$ZEP = \int_0^{\infty} F_7(k, \omega) J_0(kr) dk \quad (1i)$$

$$REP = - \int_0^{\infty} F_8(k, \omega) J_1(kr) k dk \quad (1j)$$

$$ZVF = \int_0^{\infty} F_9(k, \omega) J_0(kr) dk \quad (1k)$$

$$RVF = - \int_0^{\infty} F_{10}(k, \omega) J_1(kr) k dk \quad (1l)$$

$$ZHF = \int_0^{\infty} F_{11}(k, \omega) J_1(kr) dk \quad (1m)$$

$$RHF = \int_0^{\infty} F_{12}(k, \omega) J_0(kr) k dk \quad (1n)$$

$$-\frac{1}{r} \int_0^{\infty} [F_{12}(k, \omega) + F_{15}(k, \omega)] J_1(kr) dk$$

$$THF = \int_0^{\infty} F_{15}(k, \omega) J_0(kr) k dk \quad (1o)$$

$$-\frac{1}{r} \int_0^{\infty} [F_{12}(k, \omega) + F_{15}(k, \omega)] J_1(kr) dk$$

$$\text{PEP} = \int_0^{\infty} F_{16}(k, \omega) J_0(kr) dk \quad (1p)$$

In an isotropic medium, an arbitrarily oriented double couple without moment source model with vector $\mathbf{n} = (n_1, n_2, n_3)$ normal to the fault and $\mathbf{f} = (f_1, f_2, f_3)$ in the direction of the dislocation (Haskell, 1963; Haskell, 1964) has the following Fourier transformed displacements for a source at depth h and the receiver at a distance r from the origin and at a depth z :

$$\begin{aligned} u_z(r, z, h, \omega) = & \text{ZSS}[(f_1 n_1 - f_2 n_2) \cos 2\phi + (f_1 n_2 + f_2 n_1) \sin 2\phi] \\ & + \text{ZDS}[(f_1 n_3 + f_3 n_1) \cos \phi + (f_2 n_3 + f_3 n_2) \sin \phi] \\ & + \text{ZDD}[f_3 n_3] \end{aligned} \quad (2a)$$

$$\begin{aligned} u_r(r, z, h, \omega) = & \text{RSS}[(f_1 n_1 - f_2 n_2) \cos 2\phi + (f_1 n_2 + f_2 n_1) \sin 2\phi] \\ & + \text{RDS}[(f_1 n_3 + f_3 n_1) \cos \phi + (f_2 n_3 + f_3 n_2) \sin \phi] \\ & + \text{RDD}[f_3 n_3] \end{aligned} \quad (2b)$$

$$\begin{aligned} u_\phi(r, z, h, \omega) = & \text{TSS}[(f_1 n_1 - f_2 n_2) \sin 2\phi - (f_1 n_2 + f_2 n_1) \cos 2\phi] \\ & + \text{TDS}[(f_1 n_3 + f_3 n_1) \sin \phi - (f_2 n_3 + f_3 n_2) \cos \phi] \end{aligned} \quad (2c)$$

The vertical displacement u_z is defined positive upward, the radial displacement is positive away from the source, and the tangential displacement u_ϕ is positive in a direction clockwise from north when looking downward from above the source. The vectors \mathbf{n} and \mathbf{f} are still defined in a local coordinate system at the source in which the cartesian x, y, z axes are in the north ($\phi = 0^\circ$), east ($\phi = 90^\circ$) and downward directions, respectively. Following Herrmann (1975) the components of these vectors can be expressed in terms of the fault plane parameters of strike, dip and rake. The strike, ϕ_f , is measured clockwise from north, the dip, δ_f , is measured in a positive sense from the horizontal direction perpendicular to strike, and the rake, λ_f , is measured on the fault plane in a counterclockwise sense from the horizontal direction of strike. These angles are indicated in Figure 1.

With these conventions, all possible fault planes are encompassed by the ranges in the angles of $0^\circ \leq \phi_f < 360^\circ$, $0^\circ \leq \delta_f \leq 90^\circ$, and $-180^\circ \leq \lambda_f < 180^\circ$. With this notation, the sense of P-wave first motion at the center of the focal sphere is positive for positive values of λ_f and negative for negative values. The components of the vectors (Pujol and Herrmann, 1990) are

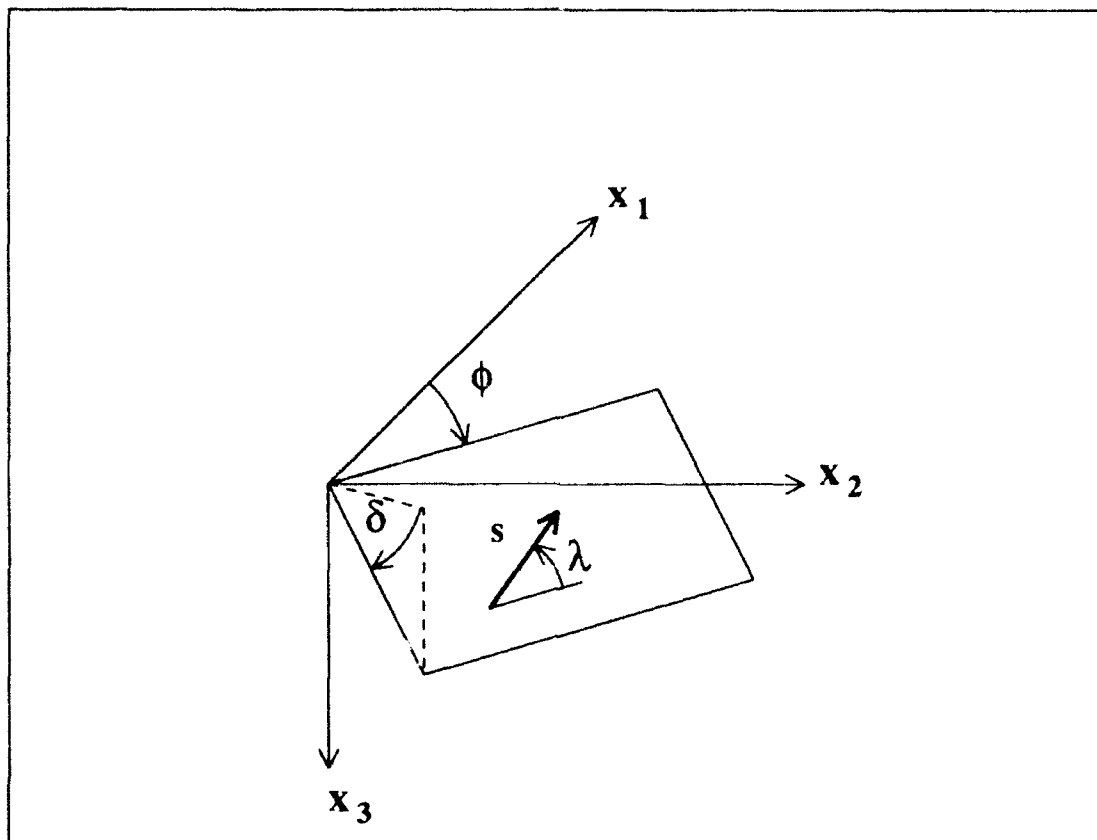


Fig. 1. Fault plane angle convention. The x_1 , x_2 and x_3 axes are in the north, east and down directions. ϕ is the strike, measured north, δ is the dip, measured downward from a horizontal direction perpendicular to the strike, and λ is the rake angle indicating the direction of motion on the fault, given by the vector \mathbf{s} . The side of the fault nearest the viewer will move in the \mathbf{s} direction.

$$f_1 = \cos \lambda_f \cos \phi_f + \sin \lambda_f \cos \delta_f \sin \phi_f$$

$$f_2 = \cos \lambda_f \sin \phi_f - \sin \lambda_f \cos \delta_f \cos \phi_f$$

$$f_3 = -\sin \lambda_f \sin \delta_f$$

$$n_1 = -\sin \phi_f \sin \delta_f$$

$$n_2 = \cos \phi_f \sin \delta_f$$

$$n_3 = -\cos \delta_f$$

Another way to combine the Green's functions is to use a moment tensor representation. Jost and Herrmann (1989) related the Green's functions in the formulation of Herrmann and Wang (1985) to a moment tensor source representation. An error entered into the Jost and Herrmann (1989) equations A5.4 - A 5.6, which were correct only for a pure deviatoric source or for a pure isotropic source. The correct expressions are as follow:

$$\begin{aligned}
 u_z(r, z, h, \omega) = & M_{xx} \left[\frac{ZSS}{2} \cos(2\phi) - \frac{ZDD}{6} + \frac{ZEP}{3} \right] \\
 & + M_{yy} \left[\frac{-ZSS}{2} \cos(2\phi) - \frac{ZDD}{6} + \frac{ZEP}{3} \right] \\
 & + M_{zz} \left[\frac{ZDD}{3} + \frac{ZEP}{3} \right] \\
 & + M_{xy} [ZSS \sin(2\phi)] \\
 & + M_{xz} [ZDS \cos(\phi)] \\
 & + M_{yz} [ZDS \sin(\phi)]
 \end{aligned} \tag{2a}$$

$$\begin{aligned}
 u_r(r, z, h, \omega) = & M_{xx} \left[\frac{RSS}{2} \cos(2\phi) - \frac{RDD}{6} + \frac{REP}{3} \right] \\
 & + M_{yy} \left[\frac{-RSS}{2} \cos(2\phi) - \frac{RDD}{6} + \frac{REP}{3} \right] \\
 & + M_{zz} \left[\frac{RDD}{3} + \frac{REP}{3} \right] \\
 & + M_{xy} [RSS \sin(2\phi)] \\
 & + M_{xz} [RDS \cos(\phi)]
 \end{aligned} \tag{2b}$$

$$\begin{aligned}
& + M_{yz} \left[RDS \sin(\phi) \right] \\
u_{\phi}(r, z, h, \omega) = & M_{xx} \left[\frac{TSS}{2} \sin(2\phi) \right] \\
& + M_{yy} \left[\frac{-TSS}{2} \sin(2\phi) \right] \\
& + M_{xy} \left[-TSS \cos(2\phi) \right] \\
& + M_{xz} \left[TDS \sin(\phi) \right] \\
& + M_{yz} \left[-TDS \cos(\phi) \right].
\end{aligned} \tag{2c}$$

Here the moment tensor elements are with respect to a coordinate system that has x-north, y-east and z-down.

The displacements corresponding to Green's functions for an arbitrarily oriented point force, given by the vector $\mathbf{f} = (f_1, f_2, f_3)$, are

$$u_z(r, z, h, \omega) = (f_1 \cos \phi + f_2 \sin \phi)ZHF + f_3ZVF$$

$$u_r(r, z, h, \omega) = (f_1 \cos \phi + f_2 \sin \phi)RHF + f_3RVF$$

and

$$u_{\phi}(r, z, h, \omega) = (f_1 \sin \phi - f_2 \cos \phi)THF,$$

where the 1, 2 and 3 indices refer to the north, east and down directions, and the angle ϕ is positive from north to and east direction. The meaning of the u_z , u_r and u_{ϕ} is the same as above.

Finally the PEP solution is the pressure field in a fluid due to an explosive source somewhere in the model.

WHOLESPACE SOLUTION

Explicit expressions for the $F_j(k, \omega)$ functions for a point buried source in a constant velocity wholespace with compressional velocity, α , shear velocity, β , and density, ρ , are derived from Haskell (1963, 1964) as follow:

Define the vertical wavenumbers for P- and S- waves as

$$v_\alpha = \begin{cases} \sqrt{k^2 - k_\alpha^2} & k \geq k_\alpha \\ i\sqrt{k_\alpha^2 - k^2} & k < k_\alpha \end{cases}$$

and

$$v_\beta = \begin{cases} \sqrt{k^2 - k_\beta^2} & k \geq k_\beta \\ i\sqrt{k_\beta^2 - k^2} & k < k_\beta \end{cases}$$

For this case, the important parameter is the vertical distance between the source and the receiver. Define this distance to be $h = h - z$. A negative value of h indicates that the receiver is beneath the source; a positive value indicates that the source is beneath the receiver. The functions appearing in the integrands of equation (1) are as follow:

$$F_1(k, \omega) = \frac{k}{4\pi\rho\omega^2} [(2k_\alpha^2 - 3k^2)e^{-v_\alpha|h|} + 3k^2e^{-v_\beta|h|}] \operatorname{sgn}(h) \quad (3a)$$

$$F_2(k, \omega) = -\frac{k}{4\pi\rho\omega^2} [(2k_\alpha^2 - 3k^2) \frac{e^{-v_\alpha|h|}}{v_\alpha} + 3v_\beta e^{-v_\beta|h|}] \quad (3b)$$

$$F_3(k, \omega) = \frac{k^2}{4\pi\rho\omega^2} [2v_\alpha e^{-v_\alpha|h|} - (2k^2 - k_\beta^2) \frac{e^{-v_\beta|h|}}{v_\beta}] \quad (3c)$$

$$F_4(k, \omega) = -\frac{1}{4\pi\rho\omega^2} [2k^2 e^{-v_\alpha|h|} - (2k^2 - k_\beta^2) e^{-v_\beta|h|}] \operatorname{sgn}(h) \quad (3d)$$

$$F_5(k, \omega) = \frac{-k^3}{4\pi\rho\omega^2} [e^{-v_\alpha|h|} - e^{-v_\beta|h|}] \operatorname{sgn}(h) \quad (3e)$$

$$F_6(k, \omega) = \frac{k}{4\pi\rho\omega^2} [\frac{k^2}{v_\alpha} e^{-v_\alpha|h|} - v_\beta e^{-v_\beta|h|}] \quad (3f)$$

$$F_7(k, \omega) = \frac{k}{4\pi\rho\alpha^2} e^{-v_\alpha|h|} \operatorname{sgn}(h) \quad (3g)$$

$$F_8(k, \omega) = \frac{-k}{4\pi\rho\alpha^2 v_\alpha} e^{-v_\alpha|h|} \quad (3h)$$

$$F_9(k, \omega) = \frac{k}{4\pi\rho\omega^2} [v_\alpha e^{-v_\alpha|h|} - \frac{k^2}{v_\beta} e^{-v_\beta|h|}] \quad (3i)$$

$$F_{10}(\mathbf{k}, \omega) = \frac{-\mathbf{k}}{4\pi\rho\omega^2} [e^{-\nu_\alpha |\mathbf{h}|} - e^{-\nu_\beta |\mathbf{h}|}] \operatorname{sgn}(\mathbf{h}) \quad (3j)$$

$$F_{11}(\mathbf{k}, \omega) = \frac{-\mathbf{k}^2}{4\pi\rho\omega^2} [e^{-\nu_\alpha |\mathbf{h}|} - e^{-\nu_\beta |\mathbf{h}|}] \operatorname{sgn}(\mathbf{h}) \quad (3k)$$

$$F_{12}(\mathbf{k}, \omega) = \frac{1}{4\pi\rho\omega^2} \left[\frac{\mathbf{k}^2}{\nu_\alpha} e^{-\nu_\alpha |\mathbf{h}|} - \nu_\beta e^{-\nu_\beta |\mathbf{h}|} \right] \quad (3l)$$

$$F_{13}(\mathbf{k}, \omega) = \frac{1}{4\pi\rho\beta^2} e^{-\nu_\beta |\mathbf{h}|} \operatorname{sgn}(\mathbf{h}) \quad (3m)$$

$$F_{14}(\mathbf{k}, \omega) = \frac{-\mathbf{k}}{4\pi\rho\beta^2\nu_\beta} e^{-\nu_\beta |\mathbf{h}|} \quad (3n)$$

$$F_{15}(\mathbf{k}, \omega) = \frac{-1}{4\pi\rho\beta^2\nu_\beta} e^{-\nu_\beta |\mathbf{h}|} \quad (3o)$$

$$F_{16}(\mathbf{k}, \omega) = \frac{\mathbf{k}}{4\pi\alpha^2\nu_\alpha} e^{-\nu_\alpha |\mathbf{h}|} \quad (\text{assumes a fluid wholespace}) \quad (3p)$$

The function $\operatorname{sgn}(x)$ is defined as

$$\operatorname{sgn}(x) = \begin{cases} -1 & x < 0 \\ 0 & x = 0 \\ 1 & x > 0 \end{cases}$$

Following Haskell (1963), it is possible to obtain analytic closed form solutions of the wholespace Green's functions corresponding to (1a) through (1j) by taking partial derivatives of the Sommerfeld integral F_v :

$$F_v = \frac{1}{R} e^{\frac{-i\omega R}{v}} = \int_0^\infty \frac{k}{\nu_v} e^{-\nu_v |\mathbf{h}|} J_0(kr) dk$$

where

$$R^2 = r^2 + h^2$$

and

$$\nu_v^2 = k^2 - \left(\frac{\omega}{v} \right)^2$$

The closed form solutions are as follow:

$$ZDD = \frac{1}{4\pi\rho\omega^2} \left[3 \frac{\partial^3 F_\alpha}{\partial h^3} + k_\alpha^2 \frac{\partial F_\alpha}{\partial h} - 3 \frac{\partial^3 F_\beta}{\partial h^3} - 3k_\beta^2 \frac{\partial F_\beta}{\partial h} \right] \quad (4a)$$

$$RDD = \frac{1}{4\pi\rho\omega^2} \left[3 \frac{\partial^3 F_\alpha}{\partial h^2 \partial r} - 3 \frac{\partial^3 F_\beta}{\partial h^2 \partial r} + k_\alpha^2 \frac{\partial F_\alpha}{\partial r} \right] \quad (4b)$$

$$ZDS = -\frac{1}{4\pi\rho\omega^2} \left[2 \frac{\partial^3 F_\alpha}{\partial h^2 \partial r} - 2 \frac{\partial^3 F_\beta}{\partial h^2 \partial r} - k_\beta^2 \frac{\partial F_\beta}{\partial r} \right] \quad (4c)$$

$$RDS = -\frac{1}{4\pi\rho\omega^2} \left[2 \frac{\partial^3 F_\alpha}{\partial r^2 \partial h} - 2 \frac{\partial^3 F_\beta}{\partial r^2 \partial h} - k_\beta^2 \frac{\partial F_\beta}{\partial h} \right] \quad (4d)$$

$$TDS = \frac{1}{4\pi\rho\omega^2} \left[\frac{2}{r} \left(\frac{\partial^2 F_\alpha}{\partial r \partial h} - \frac{\partial^2 F_\beta}{\partial r \partial h} \right) - k_\beta^2 \frac{\partial F_\beta}{\partial h} \right] \quad (4e)$$

$$ZSS = \frac{1}{4\pi\rho\omega^2} \left[2 \frac{\partial^3 F_\alpha}{\partial r^2 \partial h} + \frac{\partial^3 F_\alpha}{\partial h^3} + k_\alpha^2 \frac{\partial F_\alpha}{\partial h} - 2 \frac{\partial^3 F_\beta}{\partial r^2 \partial h} - \frac{\partial^3 F_\beta}{\partial h^3} - k_\beta^2 \frac{\partial F_\beta}{\partial h} \right] \quad (4f)$$

$$RSS = \frac{1}{4\pi\rho\omega^2} \left[2 \frac{\partial^3 F_\alpha}{\partial r^3} + \frac{\partial^3 F_\alpha}{\partial h^2 \partial r} + k_\alpha^2 \frac{\partial F_\alpha}{\partial r} - 2 \frac{\partial^3 F_\beta}{\partial r^3} - \frac{\partial^3 F_\beta}{\partial h^2 \partial r} - 2k_\beta^2 \frac{\partial F_\beta}{\partial r} \right] \quad (4g)$$

$$TSS = \frac{1}{4\pi\rho\omega^2} \left[2 \frac{\partial^3 F_\alpha}{\partial r^3} + 2 \frac{\partial^3 F_\alpha}{\partial h^2 \partial r} + 2k_\alpha^2 \frac{\partial F_\alpha}{\partial r} - 2 \frac{\partial^3 F_\beta}{\partial r^3} - 2 \frac{\partial^3 F_\beta}{\partial h^2 \partial r} - k_\beta^2 \frac{\partial F_\beta}{\partial r} \right] \quad (4h)$$

$$ZEP = -\frac{1}{4\pi\rho\alpha^2} \frac{\partial F_\alpha}{\partial h} \quad (4i)$$

$$REP = -\frac{1}{4\pi\rho\alpha^2} \frac{\partial F_\beta}{\partial r} \quad (4j)$$

$$ZVF = \frac{1}{4\pi\rho\omega^2} \left[\frac{\partial^2 F_\alpha}{\partial h^2} - \frac{\partial^2 F_\beta}{\partial h^2} - k_\beta^2 F_\beta \right] \quad (4k)$$

$$RVF = \frac{1}{4\pi\rho\omega^2} \left[\frac{\partial^2 F_\alpha}{\partial r \partial h} - \frac{\partial^2 F_\beta}{\partial r \partial h} \right] \quad (4l)$$

$$ZHF = -\frac{1}{4\pi\rho\omega^2} \left[\frac{\partial^2 F_\alpha}{\partial r \partial h} - \frac{\partial^2 F_\beta}{\partial r \partial h} \right] \quad (4m)$$

$$RHF = -\frac{1}{4\pi\rho\omega^2} \left[\frac{\partial^2 F_\alpha}{\partial r^2} - \frac{\partial^2 F_\beta}{\partial r^2} - k_\beta^2 F_\beta \right] \quad (4n)$$

$$THF = \frac{1}{4\pi\rho\omega^2} \left[\frac{1}{r} \left[\frac{\partial F_\alpha}{\partial r} - \frac{\partial F_\beta}{\partial r} \right] - k_\beta^2 F_\beta \right] \quad (4o)$$

$$PEP = \frac{1}{4\pi\rho\omega^2} F_\alpha \quad (4p)$$

where the partial derivatives are evaluated using the following analytic expressions:

$$\frac{\partial F_v}{\partial h} = -e^{-\frac{i\omega R}{v}} \left[\frac{h}{R^3} + \left(\frac{i\omega}{v} \right) \frac{h}{R^2} \right]$$

$$\frac{\partial F_v}{\partial r} = -e^{-\frac{i\omega R}{v}} \left[\frac{r}{R^3} + \left(\frac{i\omega}{v} \right) \frac{r}{R^2} \right]$$

$$\frac{\partial^2 F_v}{\partial r \partial h} = -e^{-\frac{i\omega R}{v}} \left[\left(\frac{-3rh}{R^5} \right) + \left(\frac{i\omega}{v} \right) \left(\frac{-3rh}{R^4} \right) + \left(\frac{i\omega}{v} \right)^2 \left(\frac{-rh}{R^3} \right) \right]$$

$$\frac{\partial^2 F_v}{\partial h^2} = +e^{-\frac{i\omega R}{v}} \left[\left(\frac{3h^2}{R^5} - \frac{1}{R^3} \right) + \left(\frac{i\omega}{v} \right) \left(\frac{3h^2}{R^4} - \frac{1}{R^2} \right) + \left(\frac{i\omega}{v} \right)^2 \left(\frac{h^2}{R^3} \right) \right]$$

$$\frac{\partial^2 F_v}{\partial r^2} = +e^{-\frac{i\omega R}{v}} \left[\left(\frac{3r^2}{R^5} - \frac{1}{R^3} \right) + \left(\frac{i\omega}{v} \right) \left(\frac{3r^2}{R^4} - \frac{1}{R^2} \right) + \left(\frac{i\omega}{v} \right)^2 \left(\frac{r^2}{R^3} \right) \right]$$

$$\frac{\partial^3 F_v}{\partial r^3} = -e^{-\frac{i\omega R}{v}} \left[\left(-\frac{9r}{R^5} + \frac{15r^3}{R^7} \right) + \left(\frac{i\omega}{v} \right) \left(-\frac{9r}{R^4} + \frac{15r^3}{R^6} \right) + \right]$$

$$\begin{aligned}
& \left(\frac{i\omega}{v} \right)^2 \left(-\frac{3r}{R^3} + \frac{6r^3}{R^5} \right) + \left(\frac{i\omega}{v} \right)^3 \left(\frac{r^3}{R^4} \right) \Bigg] \\
\frac{\partial^3 F_v}{\partial h^3} = & -e^{\frac{-i\omega R}{v}} \left[\left(-9\frac{h}{R^5} + \frac{15h^3}{R^7} \right) + \left(\frac{i\omega}{v} \right) \left(-9\frac{h}{R^4} + \frac{15h^3}{R^6} \right) + \right. \\
& \left. \left(\frac{i\omega}{v} \right)^2 \left(-3\frac{h}{R^3} + \frac{6h^3}{R^5} \right) + \left(\frac{i\omega}{v} \right)^3 \left(\frac{h^3}{R^4} \right) \right] \\
\frac{\partial^3 F_v}{\partial r^2 \partial h} = & -e^{\frac{-i\omega R}{v}} \left[\left(-3\frac{h}{R^5} + \frac{15r^2 h}{R^7} \right) + \left(\frac{i\omega}{v} \right) \left(-3\frac{h}{R^4} + \frac{15r^2 h}{R^6} \right) + \right. \\
& \left. \left(\frac{i\omega}{v} \right)^2 \left(-\frac{h}{R^3} + \frac{6r^2 h}{R^5} \right) + \left(\frac{i\omega}{v} \right)^3 \left(\frac{r^2 h}{R^4} \right) \right] \\
\frac{\partial^3 F_v}{\partial h^2 \partial r} = & -e^{\frac{-i\omega R}{v}} \left[\left(-\frac{3r}{R^5} + \frac{15rh^2}{R^7} \right) + \left(\frac{i\omega}{v} \right) \left(-\frac{3r}{R^4} + \frac{15rh^2}{R^6} \right) + \right. \\
& \left. \left(\frac{i\omega}{v} \right)^2 \left(-\frac{r}{R^3} + \frac{6rh^2}{R^5} \right) + \left(\frac{i\omega}{v} \right)^3 \left(\frac{rh^2}{R^4} \right) \right]
\end{aligned}$$

HALFSPACE SOLUTION

The $F_j(k, \omega)$ functions for a point buried source in a constant velocity halfspace with compressional velocity, α , shear velocity, β , and density, ρ , are derived from Haskell (1963, 1964). Let h and z be the depths of the source and receiver beneath the free surface, respectively. In the coordinate system used, both are positive quantities. Define the following functions:

Rayleigh wave period equation:

$$F_R = (\gamma - 1)^2 - \gamma^2 v_\alpha v_\beta / k^2$$

where

$$\gamma = 2k^2 / k_\beta^2.$$

Free surface reflection coefficients:

$$\mathbf{R}_{PP}^Z = [(\gamma - 1)^2 + \gamma^2 \nu_\alpha \nu_\beta / k^2] / F_R$$

$$\mathbf{R}_{PP}^R = -\mathbf{R}_{PP}^Z$$

$$\mathbf{R}_{PS}^Z = -2\gamma(\gamma - 1) / F_R$$

$$\mathbf{R}_{PS}^R = [2\gamma(\gamma - 1)\nu_\alpha \nu_\beta / k^2] / F_R$$

$$\mathbf{R}_{SP}^Z = \mathbf{R}_{PS}^R$$

$$\mathbf{R}_{SP}^R = \mathbf{R}_{PS}^Z$$

$$\mathbf{R}_{SS}^Z = -\mathbf{R}_{PP}^Z$$

$$\mathbf{R}_{SS}^R = -\mathbf{R}_{SS}^Z$$

where the superscript indicates either the vertical or radial component of motion, and the subscript indicates the incident and reflected wave types, e.g., PS indicates an incident P reflected as S. The integrands used in (1) are as follow:

we have the following expressions:

$$F_1(k, \omega) = \frac{k}{4\pi\rho\omega^2} [\quad \quad \quad] \quad (5a)$$

$$(2k_\alpha^2 - 3k^2)(e^{-\nu_\alpha|h-z|} \text{sgn}(h-z) + \mathbf{R}_{PP}^Z e^{-\nu_\alpha(h+z)} + \mathbf{R}_{PS}^Z e^{-(\nu_\alpha h + \nu_\beta z)}) \\ + 3k^2(e^{-\nu_\beta|h-z|} \text{sgn}(h-z) + \mathbf{R}_{SS}^Z e^{-\nu_\beta(h+z)} + \mathbf{R}_{SP}^Z e^{-(\nu_\beta h + \nu_\alpha z)})]$$

$$F_2(k, \omega) = -\frac{k}{4\pi\rho\omega^2} [\quad \quad \quad] \quad (5b)$$

$$\frac{(2k_\alpha^2 - 3k^2)}{\nu_\alpha} (e^{-\nu_\alpha|h-z|} + \mathbf{R}_{PP}^R e^{-\nu_\alpha(h+z)} + \mathbf{R}_{PS}^R e^{-(\nu_\alpha h + \nu_\beta z)}) \\ + 3\nu_\beta (e^{-\nu_\beta|h-z|} + \mathbf{R}_{SS}^R e^{-\nu_\beta(h+z)} + \mathbf{R}_{SP}^R e^{-(\nu_\beta h + \nu_\alpha z)})]$$

$$F_3(k, \omega) = \frac{k^2}{4\pi\rho\omega^2} [\quad \quad \quad] \quad (5c)$$

$$2\nu_\alpha (e^{-\nu_\alpha|h-z|} + \mathbf{R}_{PP}^Z e^{-\nu_\alpha(h+z)} + \mathbf{R}_{PS}^Z e^{-(\nu_\alpha h + \nu_\beta z)})$$

$$-\frac{(2k^2 - k_\beta^2)}{v_\beta} (e^{-v_\beta |h-z|} + R_{SS}^Z e^{-v_\beta (h+z)} + R_{SP}^Z e^{-(v_\beta h + v_\alpha z)})]$$

$$F_4(k, \omega) = -\frac{1}{4\pi\rho\omega^2} [\quad (5d)$$

$$2k^2(e^{-v_\alpha |h-z|} \operatorname{sgn}(h-z) + R_{PP}^R e^{-v_\alpha (h+z)} + R_{PS}^R e^{-(v_\alpha h + v_\beta z)}) \\ - (2k^2 - k_\beta^2)(e^{-v_\beta |h-z|} \operatorname{sgn}(h-z) + R_{SS}^R e^{-v_\beta (h+z)} + R_{SP}^R e^{-(v_\beta h + v_\alpha z)})]$$

$$F_5(k, \omega) = \frac{-k^3}{4\pi\rho\omega^2} [\quad (5e)$$

$$(e^{-v_\alpha |h-z|} \operatorname{sgn}(h-z) + R_{PP}^Z e^{-v_\alpha (h+z)} + R_{PS}^Z e^{-(v_\alpha h + v_\beta z)}) \\ - (e^{-v_\beta |h-z|} \operatorname{sgn}(h-z) + R_{SS}^Z e^{-v_\beta (h+z)} + R_{SP}^Z e^{-(v_\beta h + v_\alpha z)})]$$

$$F_6(k, \omega) = \frac{k}{4\pi\rho\omega^2} [\quad (5f)$$

$$\frac{k^2}{v_\alpha} (e^{-v_\alpha |h-z|} + R_{PP}^R e^{-v_\alpha (h+z)} + R_{PS}^R e^{-(v_\alpha h + v_\beta z)}) \\ - v_\beta (e^{-v_\beta |h-z|} + R_{SS}^R e^{-v_\beta (h+z)} + R_{SP}^R e^{-(v_\beta h + v_\alpha z)})]$$

$$F_7(k, \omega) = \frac{k}{4\pi\rho\alpha^2} (e^{-v_\alpha |h-z|} \operatorname{sgn}(h-z) + R_{PP}^Z e^{-v_\alpha (h+z)} + R_{PS}^Z e^{-(v_\alpha h + v_\beta z)}) \quad (5g)$$

$$F_8(k, \omega) = \frac{-k}{4\pi\rho\alpha^2 v_\alpha} (e^{-v_\alpha |h-z|} + R_{PP}^R e^{-v_\alpha (h+z)} + R_{PS}^R e^{-(v_\alpha h + v_\beta z)}) \quad (5h)$$

$$F_9(k, \omega) = \frac{k}{4\pi\rho\omega^2} [\quad (5i)$$

$$v_\alpha (e^{-v_\alpha |h-z|} + R_{PP}^Z e^{-v_\alpha (h+z)} + R_{PS}^Z e^{-(v_\alpha h + v_\beta z)}) \\ - \frac{k^2}{v_\beta} (e^{-v_\beta |h-z|} + R_{SS}^Z e^{-v_\beta (h+z)} + R_{SP}^Z e^{-(v_\beta h + v_\alpha z)})]$$

$$F_{10}(k, \omega) = \frac{-k}{4\pi\rho\omega^2} [\quad (5j)$$

$$\begin{aligned} & (e^{-\nu_\alpha|h-z|} \operatorname{sgn}(h-z) + R_{PP}^R e^{-\nu_\alpha(h+z)} + R_{PS}^R e^{-(\nu_\alpha h + \nu_\beta z)}) \\ & - (e^{-\nu_\beta|h-z|} \operatorname{sgn}(h-z) + R_{SS}^R e^{-\nu_\beta(h+z)} + R_{SP}^R e^{-(\nu_\beta h + \nu_\alpha z)}) e^{-\nu_\beta|h|}] \end{aligned}$$

$$F_{11}(k, \omega) = \frac{-k^2}{4\pi\rho\omega^2} [\quad (5k)$$

$$\begin{aligned} & (e^{-\nu_\alpha|h-z|} \operatorname{sgn}(h-z) + R_{PP}^Z e^{-\nu_\alpha(h+z)} + R_{PS}^Z e^{-(\nu_\alpha h + \nu_\beta z)}) \\ & - (e^{-\nu_\beta|h-z|} \operatorname{sgn}(h-z) + R_{SS}^Z e^{-\nu_\beta(h+z)} + R_{SP}^Z e^{-(\nu_\beta h + \nu_\alpha z)})] \end{aligned}$$

$$F_{12}(k, \omega) = \frac{1}{4\pi\rho\omega^2} [\quad (5l)$$

$$\begin{aligned} & \frac{k^2}{\nu_\alpha} (e^{-\nu_\alpha|h-z|} \operatorname{sgn}(h-z) + R_{PP}^R e^{-\nu_\alpha(h+z)} + R_{PS}^R e^{-(\nu_\alpha h + \nu_\beta z)}) \\ & - \nu_\beta (e^{-\nu_\beta|h-z|} \operatorname{sgn}(h-z) + R_{SS}^R e^{-\nu_\beta(h+z)} + R_{SP}^R e^{-(\nu_\beta h + \nu_\alpha z)})] \end{aligned}$$

$$F_{13}(k, \omega) = \frac{1}{4\pi\rho\beta^2} (e^{-\nu_\beta|h-z|} \operatorname{sgn}(h-z) + e^{-\nu_\beta(h+z)}) \quad (5m)$$

$$F_{14}(k, \omega) = \frac{-k}{4\pi\rho\beta^2\nu_\beta} (e^{-\nu_\beta|h-z|} + e^{-\nu_\beta(h+z)}) \quad (5n)$$

$$F_{15}(k, \omega) = \frac{-1}{4\pi\rho\beta^2\nu_\beta} (e^{-\nu_\beta|h-z|} + e^{-\nu_\beta(h+z)}) \quad (5o)$$

$$F_{16}(k, \omega) = \frac{k}{4\pi\alpha^2\nu_\alpha} (e^{-\nu_\alpha|h-z|} - e^{-\nu_\alpha(h+z)}) \quad (\text{assumes a fluid halfspace}) \quad (5p)$$

PLANE LAYERED MEDIA

The formulation for the seismic wave field for a buried source and a buried receiver will be presented for a medium consisting of a stack of layers within two halfspaces. This formulation will be general enough to encompass the boundary conditions of rigid or free boundary surfaces and also elastic or liquid halfspaces.

The more difficult P-SV problem will be discussed first, with a simple extension to the SH problem presented next. The major difference between

the two is the use of 4x4 matrices and compound matrices rather than 2x2 matrices. Within each section, the elastic problem will be discussed first, together with a simple extension to a liquid. The only restriction of the liquid model with respect to the elastic model, is that a liquid layer sandwiched between two solid layers will not be permitted.

Wang and Herrmann (1980) showed that the Haskell (1964) formulation for a wavefield due to a buried point source in cylindrical coordinates could be expressed as

$$\mathbf{B}_{N-1} = \mathbf{a}_{N-1}(d_{N-1})\mathbf{a}_{N-2}(d_{N-2}) \cdots \mathbf{a}_m(d_m - h_m)\Delta\mathbf{B} \\ + \mathbf{a}_{N-1}(d_{N-1})\mathbf{a}_{N-2}(d_{N-2}) \cdots \mathbf{a}_1(d_1)\mathbf{B}_0 \quad (6)$$

where the layering convention of Haskell (1964) is followed. The transformed motion-stress vector \mathbf{B}_k is evaluated at the k 'th interface. For P-SV waves $\mathbf{B}_k = (U_r, U_z, T_z, T_r)^T$ and for SH waves $\mathbf{B}_k = (U_\phi, T_\phi)^T$. The medium properties of the k 'th layer are between the $k-1$ 'th and k 'th interfaces. The layer thickness of the k 'th layer is d_k , the compressional and shear wave velocities are α_k and β_k , respectively, and the density is ρ_k . The source is at a depth of h_m in the m 'th layer. This is indicated in Figure 2. Equation (6) states that the wavefield at some position beneath the source is a function of the wavefield discontinuity at the source and also the wavefield at the top boundary. There is nothing in this formulation restricting the 0'th interface to be a free surface, or the N 'th medium to be a halfspace. The source is at a depth h_m in the m 'th layer.

Haskell (1964) expressed (1) in terms of upgoing and downgoing P- and SV- potential coefficients, giving a total of four coefficients for each layer. At the top and bottom boundaries, the boundary conditions require only two unknowns. This observation is used below.

P-SV Problem

Let us assume that there are matrices \mathbf{G} and \mathbf{H} such that

$$\begin{bmatrix} 0 \\ 0 \\ a \\ b \end{bmatrix} = \mathbf{G}\mathbf{B}_{N-1} \quad (7)$$

and

$$\mathbf{B}_0 = \mathbf{H}(c, d, 0, 0)^T \quad (8)$$

Multiplying (6) on the left by \mathbf{G} and defining

$$\mathbf{X} = \mathbf{G}\mathbf{a}_{N-1}(d_{N-1})\mathbf{a}_{N-2}(d_{N-2}) \cdots \mathbf{a}_m(d_m - h_m)$$

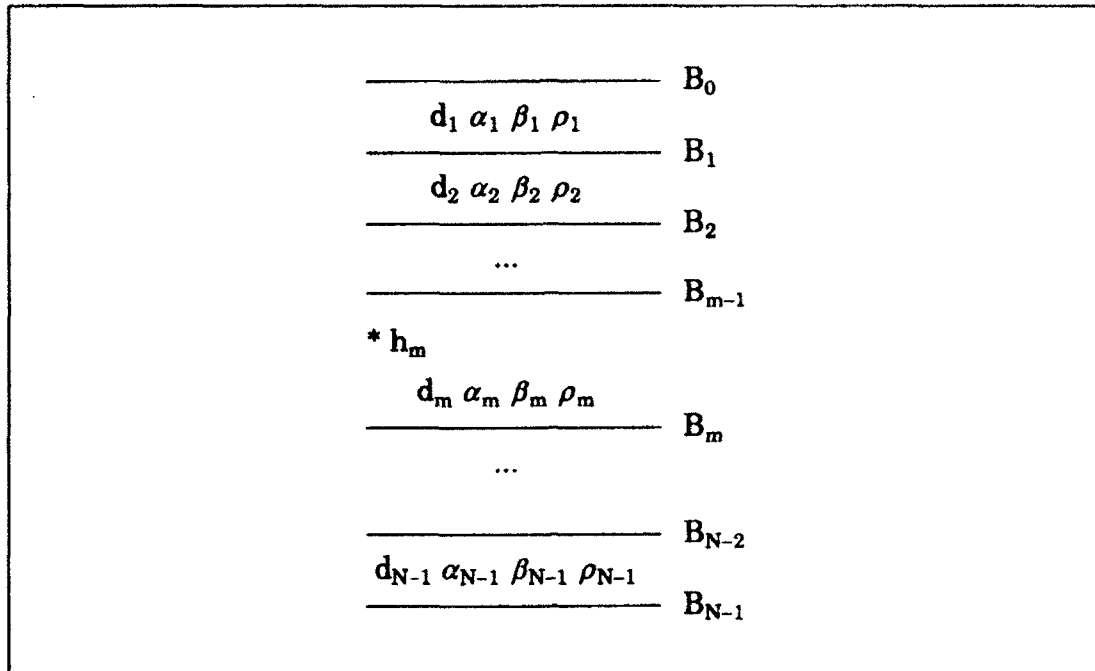


Fig. 2. Model of layered medium, showing the stress-displacement vectors at the interfaces and the medium parameters within the layers.

and

$$\mathbf{R} = \mathbf{G}a_{N-1}(d_{N-1})a_{N-2}(d_{N-2}) \cdots a_1(d_1)\mathbf{H},$$

and using (7) and (8)

$$\begin{bmatrix} 0 \\ 0 \\ a \\ b \end{bmatrix} = \mathbf{XS} + \mathbf{R} \begin{bmatrix} c \\ d \\ 0 \\ 0 \end{bmatrix} \quad (9)$$

where we have set $\mathbf{S} = \Delta\mathbf{B}$.

Consider the first two equations in this linear system of four equations. The left side is zero, and we can solve directly for the unknowns c and d :

$$\begin{bmatrix} c \\ d \end{bmatrix} = \frac{-1}{R_{11}R_{22} - R_{12}R_{21}} \begin{bmatrix} R_{22} & -R_{12} \\ -R_{21} & R_{11} \end{bmatrix} \begin{bmatrix} X_{1i}S_i \\ X_{2i}S_i \end{bmatrix} \quad (10)$$

$$= \frac{-1}{R|_{12}^{12}} \begin{bmatrix} R_{22}X_{1i}S_i - R_{12}X_{2i}S_i \\ R_{21}X_{1i}S_i - R_{11}X_{2i}S_i \end{bmatrix} \quad (11)$$

$$= \frac{-1}{R|_{12}^{12}} \begin{bmatrix} X_{2j}Z_{j2}X_{1i}S_i - X_{1j}Z_{j2}X_{2i}S_i \\ -X_{2j}Z_{j1}X_{1i}S_i + X_{1j}Z_{j1}X_{2i}S_i \end{bmatrix} \quad (12)$$

$$= \frac{-1}{R|_{12}^{12}} \begin{bmatrix} S_i X|_{ij}^{12} Z_{j2} \\ -S_i X|_{ij}^{12} Z_{j1} \end{bmatrix} \quad (13)$$

where we have used $\mathbf{R} = \mathbf{XZ}$, and the compound matrix definition $R|_{kl}^{ij} = R_{ik}R_{jl} - R_{il}R_{jk}$. Note that the repeated indices represent summations in the range 1 - 4.

This is essentially the derivation given in Wang and Herrmann (1980), where the \mathbf{G} matrix was designed to give the upward and downward potentials in the halfspace, and the \mathbf{H} matrix was such to make the free surface stress free, with $c = U_r$, and $d = U_z$, the displacements at the top boundary.

The formulation of (13) has proven to be numerically stable. To get the wavefield at points above the source, it is obvious through the use of propagator matrices that at a depth h_k in the k 'th layer, which is above the source,

$$\mathbf{B}_k = a_k(h_k) \cdots a_1(d_1) \mathbf{H} \begin{bmatrix} c \\ d \\ 0 \\ 0 \end{bmatrix} \quad (14)$$

$$= \mathbf{y} \begin{bmatrix} c \\ d \\ 0 \\ 0 \end{bmatrix}. \quad (15)$$

One may be tempted to use (11) first, and then (12) to evaluate the wavefield of a buried receiver directly, but this is not numerically stable, due to possibly increasing exponential terms in \mathbf{y} . (In the extreme case of a layered wholespace, the whole space solutions indicate that an exponentially decreasing solution is required in the z -direction away from the source).

To work around this problem, we note that $\mathbf{R} = \mathbf{XZ} = \mathbf{X}\mathbf{x}\mathbf{y}$, where we define

$$\mathbf{x} = a_m(h_m) \cdots a_k(d_k - h_k) \quad (16)$$

and

$$\mathbf{y} = a_k(h_k) \cdots a_1(d_1) \mathbf{H}, \quad (17)$$

where the propagator matrix property $a(h_1) \cdot a(h_2) = a(h_1 + h_2)$ is used. Combining equations (13 - 17), we have, after some algebra,

$$\mathbf{B}_k = \begin{bmatrix} U_r \\ U_z \\ T_z \\ T_{r,k} \end{bmatrix} = \frac{-1}{R|_{12}^{12}} \begin{bmatrix} S_i X|_{il}^{12} x_{lm} y|_{12}^{1m} \\ S_i X|_{il}^{12} x_{lm} y|_{12}^{2m} \\ S_i X|_{il}^{12} x_{lm} y|_{12}^{3m} \\ S_i X|_{il}^{12} x_{lm} y|_{12}^{4m} \end{bmatrix} \quad (18)$$

If this is written in terms of a matrix multiplication, and using the properties of the compound matrix that $A|_{kl}^{\bar{ij}} = -A|_{kl}^{ji} = -A|_{lk}^{\bar{ij}}$, and that $A|_{kl}^{\bar{ij}} = 0$ for $i=j$ or $j=k$,

$$[U_r, U_z, T_z, T_{r,k}]_k = \frac{-1}{R|_{12}^{12}} [S_1, S_2, S_3, S_4] \quad (19)$$

$$\begin{bmatrix} 0 & X|_{12}^{12} & X|_{13}^{12} & X|_{14}^{12} \\ -X|_{12}^{12} & 0 & X|_{23}^{12} & X|_{24}^{12} \\ -X|_{13}^{12} & -X|_{23}^{12} & 0 & X|_{34}^{12} \\ -X|_{14}^{12} & -X|_{24}^{12} & -X|_{34}^{12} & 0 \end{bmatrix}$$

$$\begin{bmatrix} X_{11} & X_{12} & X_{13} & X_{14} \\ X_{21} & X_{22} & X_{23} & X_{24} \\ X_{31} & X_{32} & X_{33} & X_{34} \\ X_{41} & X_{42} & X_{43} & X_{44} \end{bmatrix}$$

$$\begin{bmatrix} 0 & -y|_{12}^{12} & -y|_{12}^{13} & -y|_{12}^{14} \\ y|_{12}^{12} & 0 & -y|_{12}^{23} & -y|_{12}^{24} \\ y|_{12}^{13} & y|_{12}^{23} & 0 & -y|_{12}^{34} \\ y|_{12}^{14} & y|_{12}^{24} & y|_{12}^{34} & 0 \end{bmatrix}$$

Noting that the compound matrix indices comprise six doublets, we can further simplify the expression (14) by expressing the compound matrix elements associating the the compound matrix doublets (12, 13, 14, 23, 24, 34), with the indices { 1, 2, 3, 4, 5, 6 }, respectively, defining, for example, $X_{12} = X|_{13}^{12}$. Thus (14) becomes

$$[U_r, U_z, T_z, T_{r,k}]_k = \frac{-1}{R|_{12}^{12}} (S_1, S_2, S_3, S_4) \quad (20)$$

$$\begin{bmatrix} 0 & X_{11} & X_{12} & X_{13} \\ -X_{11} & 0 & X_{14} & X_{15} \\ -X_{12} & -X_{14} & 0 & X_{16} \\ -X_{13} & -X_{15} & -X_{16} & 0 \end{bmatrix}$$

$$\begin{bmatrix} X_{11} & X_{12} & X_{13} & X_{14} \\ X_{21} & X_{22} & X_{23} & X_{24} \\ X_{31} & X_{32} & X_{33} & X_{34} \\ X_{41} & X_{42} & X_{43} & X_{44} \end{bmatrix}$$

$$\begin{bmatrix} 0 & -y_{11} & -y_{21} & -y_{31} \\ y_{11} & 0 & -y_{41} & -y_{51} \\ y_{21} & y_{41} & 0 & -y_{61} \\ y_{31} & y_{51} & y_{61} & 0 \end{bmatrix}$$

Form of the G matrices for various bottom layer conditions.

Bottom Halfspace Free

$$G = \begin{bmatrix} 0 & 0 & 1 & 0 \\ 0 & 0 & 0 & 1 \\ 1 & 0 & 0 & 0 \\ 0 & 1 & 0 & 0 \end{bmatrix} \quad (21)$$

for which $a = U_r$, $b = U_z$, and we force $T_z = 0$ and $T_r = 0$ at the N-1'st interface.

Bottom Halfspace Rigid

$$G = \begin{bmatrix} 1 & 0 & 0 & 0 \\ 0 & 1 & 0 & 0 \\ 0 & 0 & 1 & 0 \\ 0 & 0 & 0 & 1 \end{bmatrix} \quad (22)$$

for which $a = T_z$, $b = T_r$, and we force $U_z = 0$ and $U_r = 0$ at the N-1'st interface.

Bottom Halfspace Elastic

$$G = \begin{bmatrix} -\rho\gamma & \rho(\gamma-1)/v_\alpha & 1 & -k^2/v_\alpha \\ -\rho(\gamma-1)/v_\beta & \rho\gamma/k^2 & 1/v_\beta & -1 \\ -\rho\gamma & -\rho(\gamma-1)/v_\alpha & 1 & k^2/v_\alpha \\ \rho(\gamma-1)/v_\beta & \rho\gamma/k^2 & -1/v_\beta & -1 \end{bmatrix} \quad (23)$$

where $a = 2A'$, $b = 2B'$ in the Haskell (1964) notation, and we force $2A'' = 0$ and $2B'' = 0$. This guarantees only downwardly propagating wavefields in the halfspace.

To form the compound the elements of the **R** and **X** we need only the first row of the 6x6 compound **G** matrix. The necessary compound matrix elements of the **G** matrix are

$G _{ij}^{12}$	Free	Rigid	Elastic
$G _{12}^{12}$	0	1	$\rho^2 \left(-\gamma^2 / k^2 + (\gamma - 1)^2 / v_\alpha v_\beta \right)$
$G _{13}^{12}$	0	0	$-\rho / v_\beta$
$G _{14}^{12}$	0	0	$\rho \left(\gamma - k^2 (\gamma - 1) / v_\alpha v_\beta \right)$
$G _{23}^{12}$	0	0	$\rho \left(-\gamma / k^2 + (\gamma - 1) / v_\alpha v_\beta \right)$
$G _{24}^{12}$	0	0	ρ / v_α
$G _{34}^{12}$	1	0	$k^2 / v_\alpha v_\beta - 1$

Form of the **H** matrices at the top interface

Top Surface Free

$$\mathbf{H} = \begin{bmatrix} 1 & 0 & 0 & 0 \\ 0 & 1 & 0 & 0 \\ 0 & 0 & 1 & 0 \\ 0 & 0 & 0 & 1 \end{bmatrix} \quad (24)$$

for which $c = U_r$, $d = U_z$, and we force $T_z = 0$ and $T_r = 0$ at the 0'th interface.

Top Surface Rigid

$$\mathbf{H} = \begin{bmatrix} 0 & 0 & 1 & 0 \\ 0 & 0 & 0 & 1 \\ 1 & 0 & 0 & 0 \\ 0 & 1 & 0 & 0 \end{bmatrix} \quad (25)$$

for which $c = T_z$, $d = T_r$, and we force $U_z = 0$ and $U_r = 0$ at the 0'th interface.

Elastic Medium above top surface

$$2\mathbf{H} = \begin{bmatrix} -1/\rho & v_\beta/\rho & -1/\rho & -v_\beta/\rho \\ -v_\alpha/\rho & k^2/\rho & v_\alpha/\rho & k^2/\rho \\ -(\gamma-1) & \gamma v_\beta & -(\gamma-1) & -\gamma v_\beta \\ -\gamma v_\alpha/k^2 & \gamma-1 & \gamma v_\alpha/k^2 & \gamma-1 \end{bmatrix} \quad (26)$$

for which $c = 2A''$, $d = 2B''$, and we force $2A' = 0$ and $2B' = 0$ at the 0'th interface. This guarantees only upwardly propagating wavefields.

The necessary compound matrix elements of the \mathbf{H} matrix are

$H _{12}^0$	Free	Rigid	Elastic
$H _{12}^{12}$	1	0	$(v_\alpha v_\beta - k^2)/4\rho^2$
$H _{12}^{13}$	0	0	$-v_\beta/4\rho$
$H _{12}^{14}$	0	0	$(\gamma v_\alpha v_\beta/k^2 - (\gamma-1))/4\rho$
$H _{12}^{23}$	0	0	$(k^2(\gamma-1) - \gamma v_\alpha v_\beta)/4\rho$
$H _{12}^{24}$	0	0	$v_\alpha/4\rho$
$H _{12}^{34}$	0	1	$(\gamma^2 v_\alpha v_\beta/k^2 - (\gamma-1)^2)/4$

LIQUID LAYER

The inclusion of a liquid layer in the model complicates the formulation, since only P-potentials are required and the Haskell matrix formulation in terms of P- and SV-arrivals does not simply reduce to the fluid problem. The 4x4 propagator matrices in the elastic medium must then be connect to 2x2 propagator matrices in the fluid. This complicates the structure of the program.

If a simplifying assumption is made, *that the liquid layer is not between two elastic layers*, the mathematics is simplified. This restriction, means that the 4x4 matrix computations will be maintained, but with a slightly different meaning for the propagator matrix. Basically, in a fluid, only U_z and T_z must be computed, since only these two quantities are continuous at boundaries. In a fluid T_r is by definition zero, and U_r is discontinuous at boundaries.

Let the $l+1$ 'st layer be elastic and the l 'th layer be fluid. Let the elastic displacements at the top of the elastic layer be related to the fluid displacements at the top of the fluid layer by the following *pseudo*-propagator matrix relation:

$$\begin{bmatrix} U_r \\ U_z \\ T_z \\ T_r \end{bmatrix}_l = \begin{bmatrix} 1 & 0 & 0 & 0 \\ 0 & \cosh v_\alpha d & -v_\alpha \sinh v_\alpha d / \rho & 0 \\ 0 & -\rho \sinh v_\alpha d / v_\alpha & \cosh v_\alpha d & 0 \\ 0 & 0 & 0 & 1 \end{bmatrix} \begin{bmatrix} (U_r)_{l-1} \\ (U_z)_{l-1} \\ (T_z)_{l-1} \\ (T_r)_{l-1} \end{bmatrix} \quad (27)$$

This *pseudo*-propagator propagates the vertical displacement and stress downward to the top of the elastic layer for future use, while placing no constraint upon the radial displacement or stress. This was first used by Hudson (1969). For example, the requirement that $(T_r)_l = 0$ can be met after multiplying by the 4×4 matrix in (27). The restriction that the fluid layer cannot be between two solid layers, arises from the fact that four free parameters, radial displacement and stress at the two elastic fluid boundaries, must be saved, but this formalism permits only two free parameters to be retained. To compute U_r in the fluid, we note that it is proportional to T_z in the fluid.

Given this preface, the following matrices are used to meet the possible boundary conditions if a fluid layer is at the surface or the lower halfspace of the model:

The **G** matrix for the halfspace.

Bottom Halfspace Free

$$\mathbf{G} = \begin{bmatrix} 0 & 0 & 1 & 0 \\ 0 & 0 & 0 & 1 \\ 1 & 0 & 0 & 0 \\ 0 & 1 & 0 & 0 \end{bmatrix} \quad (28)$$

for which $a = U_r$, $b = U_z$, and we force $T_z = 0$ and $T_r = 0$ at the $N-1$ 'st interface.

Bottom Halfspace Fluid

$$\mathbf{G} = \begin{bmatrix} 0 & 0 & 0 & 1 \\ 0 & -\rho/2v_\alpha & 1/2 & 0 \\ 0 & \rho/2v_\alpha & 1/2 & 0 \\ 1 & 0 & 0 & 0 \end{bmatrix} \quad (29)$$

where $a = A'$, $b = U_r$, and we force $A'' = 0$ and $T_r = 0$. This guarantees only downwardly propagating wavefields in the halfspace.

The necessary compound matrix elements of the **G** matrix are

$G _{ij}^{12}$	Free	Elastic
$G _{12}^{12}$	0	0
$G _{13}^{12}$	0	0
$G _{14}^{12}$	0	0
$G _{23}^{12}$	0	0
$G _{24}^{12}$	0	$\rho/2v_a$
$G _{34}^{12}$	1	-1/2

Form of the **H** matrix at the top interface

Top Surface Free

$$\mathbf{H} = \begin{bmatrix} 1 & 0 & 0 & 0 \\ 0 & 1 & 0 & 0 \\ 0 & 0 & 1 & 0 \\ 0 & 0 & 0 & 1 \end{bmatrix} \quad (30)$$

for which $c = U_r$ at top of closest elastic layer beneath the fluid, $d = U_z$ at the top of the fluid, and we force $T_z = 0$ at the top of the fluid and $T_r = 0$ at the top of the closest elastic layer underneath. The top of the fluid is the 0'th interface.

Fluid halfspace above top layer

$$2\mathbf{H} = \begin{bmatrix} 1 & 0 & 0 & 0 \\ 0 & -v_a/\rho & v_a/\rho & 0 \\ 0 & 1 & 1 & 0 \\ 0 & 0 & 0 & 1 \end{bmatrix} \quad (31)$$

for which $c = U_r$ at the closest elastic interface, $d = A''$, and we force $A' = 0$ at the 0'th interface and $T_r = 0$ at the top of the nearest elastic boundary. This guarantees only upwardly propagating wavefields into the upper halfspace.

The necessary compound matrix elements of the **H** matrix are

$$\overline{\mathbf{H}}|_{12}^{ij} \quad \text{Free} \quad \text{Elastic}$$

$H _{12}^{12}$	1	$-v_a/\rho$
$H _{12}^{13}$	0	1
$H _{12}^{14}$	0	0
$H _{12}^{23}$	0	0
$H _{12}^{24}$	0	0
$H _{12}^{34}$	0	0

SH Problem

The SH development uses the same formalism as (6), except that the a_k matrices are now 2x2 rather than 4x4. To represent the boundary conditions at the top and bottom boundaries, we assume that there are g and h matrices such that

$$\begin{bmatrix} 0 \\ e \end{bmatrix} = gB_N \quad (32)$$

and

$$B_0 = h \begin{bmatrix} f \\ 0 \end{bmatrix} \quad (33)$$

Here $B = [U_\phi, T_\phi]^T$. Multiplying (32) on the left by G and using (6), and defining

$$x = g a_{N-1}(d_{N-1}) a_{N-2}(d_{N-2}) \cdots a_m(d_m - h_m)$$

and

$$r = g a_{N-1}(d_{N-1}) a_{N-2}(d_{N-2}) \cdots a_1(d_1) h,$$

we have

$$\begin{bmatrix} 0 \\ e \end{bmatrix} = xs + r \begin{bmatrix} f \\ 0 \end{bmatrix} \quad (34)$$

where we have set $s = \Delta B$.

The coefficient f is quickly found by the relation

$$f = -\left(\frac{x_{11}s_1 + x_{12}s_2}{r_{11}}\right) \quad (35)$$

To find the displacement field anywhere between the top boundary and the source depth, we use the propagator matrix

$$B_k = a_k(h_k) \cdots a_1(d_1) h \begin{bmatrix} f \\ 0 \end{bmatrix} \quad (36)$$

$$= y \begin{bmatrix} f \\ 0 \end{bmatrix}. \quad (37)$$

Thus the transformed tangential displacement is just

$$U_\phi = -y_{11} \left(\frac{x_{11}s_1 + x_{12}s_2}{r_{11}} \right), \quad (38)$$

which is a stable numerical function.

Form of the g matrix for various bottom layer conditions

Bottom Boundary Free Surface

$$g = \begin{bmatrix} 0 & 1 \\ 1 & 0 \end{bmatrix} \quad (39)$$

Bottom Elastic Halfspace

$$g = \begin{bmatrix} \rho v_\beta & \frac{1}{\beta^2} \\ \rho v_\beta & \frac{-1}{\beta^2} \end{bmatrix} \quad (40)$$

(The true expression should have terms like ω^2 / β^2 instead of $1 / \beta^2$, but the source expressions are either of the form $[a \ 0]^T$ or $[0 \ b / \omega^2]^T$. Thus the multiplications required for (38) will eliminate the ω^2 terms, and the apparent $\omega = 0$ singularity is numerically avoided by using this form for the g matrix and $[0 \ b]^T$ for the source expression.)

Bottom Halfspace Rigid

$$g = \begin{bmatrix} 1 & 0 \\ 0 & 1 \end{bmatrix} \quad (41)$$

Form of the \mathbf{h} matrix for various top layer conditions

Top surface free

$$\mathbf{h} = \begin{bmatrix} 1 & 0 \\ 0 & 1 \end{bmatrix} \quad (42)$$

Top surface elastic

$$\mathbf{h} = \begin{bmatrix} \frac{1}{2} & \frac{1}{2} \\ \frac{1}{2} \rho \beta^2 \nu_\beta & -\frac{1}{2} \rho \beta^2 \nu_\beta \end{bmatrix} \quad (43)$$

Top surface rigid

$$\mathbf{h} = \begin{bmatrix} 0 & 1 \\ 1 & 0 \end{bmatrix} \quad (44)$$

Source Terms

The source terms, \mathbf{S} , representing the discontinuity in the displacement-stress values across the source layer are given in the following table for different source representations. The S_i values are the P-SV source terms used in equations (10-13, 18, 19) while the s_i are the SH source terms given in Table 1.

Table 1. Source Term Coefficients						
Term	S_1	S_2	S_3	S_4	s_1	s_2
DD	0	$\frac{4kk_\alpha^2}{4\pi\rho\omega^2}$	0	$\frac{2k((2\beta/\alpha)^2 - 3)}{4\pi\omega^2}$	0	0
DS	$\frac{2k_\beta^2}{4\pi\rho\omega^2}$	0	0	0	$\frac{-2}{4\pi\rho\beta^2}$	0
SS	0	0	0	$\frac{-2k}{4\pi\omega^2}$	0	$\frac{2k}{4\pi}$
EP	0	$\frac{2kk_\alpha^2}{4\pi\rho\omega^2}$	0	$\frac{4kk_\alpha^2}{4\pi\omega^2 k_\beta^2}$	0	0
VF	0	0	$\frac{-2k}{4\pi\omega^2}$	0	0	0
HF	0	0	0	$\frac{-2}{4\pi\omega^2}$	0	$\frac{2}{4\pi}$

To obtain the required integrand in (1), the above source coefficients are used with (20) for U_z and U_r and (38) for U_ϕ to yield the following F_j factors. By taking the negative of the U_z terms, we guarantee that the corresponding Green's functions yield positive ground motion in an upward direction.

F_j	Source Term
$F_1 = -U_z$	S_{DD}
$F_2 = U_r$	S_{DD}
$F_3 = -U_z$	S_{DS}
$F_4 = U_r$	S_{DS}
$F_5 = -U_z$	S_{SS}
$F_6 = U_r$	S_{SS}
$F_7 = -U_z$	S_{EP}
$F_8 = U_r$	S_{EP}
$F_9 = -U_z$	S_{VF}
$F_{10} = U_r$	S_{VF}
$F_{11} = -U_z$	S_{HF}
$F_{12} = U_r$	S_{HF}
$F_{13} = U_\phi$	s_{DS}
$F_{14} = U_\phi$	s_{SS}
$F_{15} = U_\phi$	s_{HF}
$F_{16} = \rho F_8$	(receiver in fluid)

Evaluation for receiver beneath the source.

The matrices used for the general solution, (20) and (38) were derived for the source position beneath the receiver. It was because of this assumption that the relatively simple expression were obtained. If the source is above the receiver, then an alternative derivation is required, first to obtain the coefficients c, d or e . From these, B_{N-1} is found, and then the propagator matrices can be used. The problem with this technique is that extra computational steps must be placed into the coding. The alternative approach is to invert the order of the layered model by reversing the sense of the z axis, to note the source and receiver positions in the new model, and then to evaluate the solution using (20) and (38). Finally, care is taken to preserve the sense of positive positive displacements of the original model. This last task is accomplished in two stages. First the S_2, S_4 and s_2 coefficients are replaced by $-S_2, -S_4$, and $-s_2$, since these are the source coefficients that depend on the direction of the local vertical. Once the final displacements are computed, the vertical displacements are inverted, while the radial and transverse time histories are unchanged. This sequence of steps is tested by looking the the P- and S-wave particle motions for receivers above and beneath the source.

TIME HISTORIES

Evaluation of the inverse Fourier tranfrom to yield a time series is usually accomplished by an inverse Fast Fourier Transform (Brigham, 1974)

which approximates the true inverse transform

$$g(t) = \int_{-\infty}^{\infty} G(f) e^{i2\pi ft} df$$

by the inverse Discrete Fourier Transform

$$g(k\Delta t) = \sum_{n=0}^{N-1} G(n\Delta f) e^{i2\pi n k \Delta t \Delta f} \Delta f \quad \text{for } k = 0, \dots, N-1$$

where $\Delta f = \frac{1}{N\Delta t}$. (Note that this is related to the original Fourier transform definition defined in the introduction if $h(t)=g(t)$ and $G(f)=H(2\pi f)$). This approximation to the continuous Fourier Transform introduces concerns about finite frequency and time windows and periodicity in the time and frequency domains. This will always be present when the discrete Fourier transform pair is used, but can be controlled so that the discrete Fourier transform result is a reasonable approximation to the desired Fourier transform solution.

The first problem considered concerns the effect of the finite frequency window in the resultant time histories. The function $H(f)$ is sampled in the range $(-f_N, f_N)$ where $f_N = \frac{1}{2\Delta t}$. Frequencies outside this range are effectively set to zero. If the transitions through the frequency points $f = \pm f_N$ are not smooth, high frequency ripples will be seen in the time domain. This effect can be significantly reduced in synthetic seismograms by choosing source time functions that have zeros at the Nyquist frequencies $\pm f_N$. Two possible functions that have this property are the triangular and parabolic pulses.

Triangular:

$$s(t) = \frac{1}{\tau} \begin{cases} 0 & t \leq 0 \\ \frac{t}{\tau} & 0 \leq t \leq \tau \\ 1 - \frac{t}{\tau} & \tau \leq t \leq 2\tau \\ 0 & t \geq 2\tau \end{cases}$$

which has the Fourier transform

$$e^{-i\omega\tau} \left[\frac{\sin \pi f \tau}{\pi f \tau} \right]^2$$

This is a positive pulse with unit area and a corner frequency $f_c = 1/\pi\tau$. If

$\tau = 2M\Delta t$ and $M \geq 1$, this function has spectral zeros at frequencies $\frac{1}{M} f_N$, $\frac{2}{M} f_N, \dots, f_N$, where f_N is the Nyquist frequency defined as $f_N = \frac{1}{2\Delta t}$. Thus if we sample the Fourier transform of this pulse and apply the inverse discrete Fourier Transform, we will see a nice sampled triangular pulse without any ripples in the time domain.

Parabolic:

$$s(t) = \frac{1}{2\tau} \begin{cases} 0 & t \leq 0 \\ 1/2(t/\tau)^2 & 0 < t \leq \tau \\ -1/2(t/\tau)^2 + 2(t/\tau) - 1 & \tau \leq t \leq 3\tau \\ 1/2(t/\tau)^2 - 4(t/\tau) + 8 & 3\tau < t \leq 4\tau \\ 0 & t > 4\tau \end{cases}$$

The Fourier transform of this function is

$$e^{-i\omega 2\tau} \frac{[2 \sin \omega \tau - \sin 2\omega \tau]}{(\omega \tau)^3} = e^{-i\omega 2\tau} \frac{4 \sin^2 \frac{\omega \tau}{2} \sin \omega \tau}{(\omega \tau)^3}.$$

This time function has a unit area and a corner frequency $f_c = 1/4.575\tau$. In addition, it has spectral zeros at certain frequencies. If $\tau = M\Delta t$, where $M > 1$, then spectral zeros are at frequencies $\frac{1}{M} f_N, \frac{2}{M} f_N, \dots, f_N$. By choosing τ and Δt such that one of the spectral zeros occurs at the Nyquist frequency, the pulses can be synthesized and propagated through the model without the rippling introduced by an arbitrary, sharp high frequency spectral cutoff. Note that the parabolic pulse with $\tau = \Delta t$ will give the same sample values at the triangular pulse with $\tau = 2\Delta t$.

The other problem to be addressed is that of the periodicity of the discrete Fourier transform pair. This can be addressed by introducing complex frequencies.

Consider the the Fourier transform pair

$$G(\omega) = \int_{-\infty}^{\infty} g(t)e^{-i\omega t} dt \quad g(t) = \frac{1}{2\pi} \int_{-\infty}^{\infty} G(\omega)e^{i\omega t} d\omega$$

or symbolically

$$g(t) \Longleftrightarrow G(\omega)$$

From this definition, we see that

$$e^{-\alpha t} g(t) \Longleftrightarrow G(\omega - i\alpha)$$

This is equivalent to stating that

$$g(t) = e^{\alpha t} \frac{1}{2\pi} \int_{-\infty}^{\infty} G(\omega - i\alpha) e^{i\omega t} d\omega$$

The convolution theorem states that given

$$x(t) \Longleftrightarrow X(\omega)$$

$$y(t) \Longleftrightarrow Y(\omega)$$

then

$$z(t) = x(t) * y(t) \Longleftrightarrow X(\omega)Y(\omega)$$

and

$$e^{-\alpha t} z(t) = \left(e^{-\alpha t} x(t) \right) * \left(e^{-\alpha t} y(t) \right) \Longleftrightarrow X(\omega - i\alpha) Y(\omega - i\alpha)$$

The time shift theorem states that

$$g(t - t_0) \Longleftrightarrow G(\omega) e^{-i\omega t_0}$$

and hence

$$e^{-\alpha(t-t_0)} g(t - t_0) \Longleftrightarrow G(\omega - i\alpha) e^{-i\omega t_0}$$

or, by using the linearity of the Fourier transform,

$$e^{-\alpha t} g(t - t_0) \Longleftrightarrow G(\omega - i\alpha) e^{-i(\omega - i\alpha)t_0}$$

This indicates how a time shift is formed in the frequency domain and the proper de-attenuation factor in the time time.

The value of using the time domain attenuation is obvious when attempting to propagate a simple pulse, e.g., to evaluate the inverse transform of $H(\omega) e^{-i\frac{\omega}{c}x}$ as x increases. As x increases, the pulse will arrive at later times. However, it will eventually wrap around to appear at zero time. This periodicity effect can be reduced by using the time domain attenuation technique. Upon wrap around, the pulse will be attenuated in amplitude by $e^{-\alpha N\Delta t}$. Obviously the larger the value of α , the lower the amplitude of this effect.

An important added advantage of this technique is that it will remove the surface wave poles and branch point singularities from the real wavenumber axis for a perfectly elastic problem, so that contour integration is not required in the wavenumber domain (Phinney, 1965).

An example of this technique is given in Figure 3. For computational speed, the RDD Green's function for a wholespace (4b) is evaluated. The P-

wave and S-wave velocities are 6.0 and 3.5 km/s, respectively, the density is 2.8 gm/cm³, the receiver is a height 5 km above the source, and synthetics are computed to distances of 300 km. All traces start at -5.0 and terminate at 58 seconds. The sampling interval is 1.0 s, and the triangular pulse has a base of 4.0 s, e.g., $\tau = 2.0$ s. Figure 3a shows the result of using $\alpha = 0.0$. In this case the wrap around of the S-wave arrival beyond 175 km is obvious. By using $\alpha = 0.04$ in Figure 3b, the amplitude of the wrapped S-wave is reduced. Of course, if the P-wave wraps around, the traces will look different, and the P-wave amplitude will be significantly reduced.

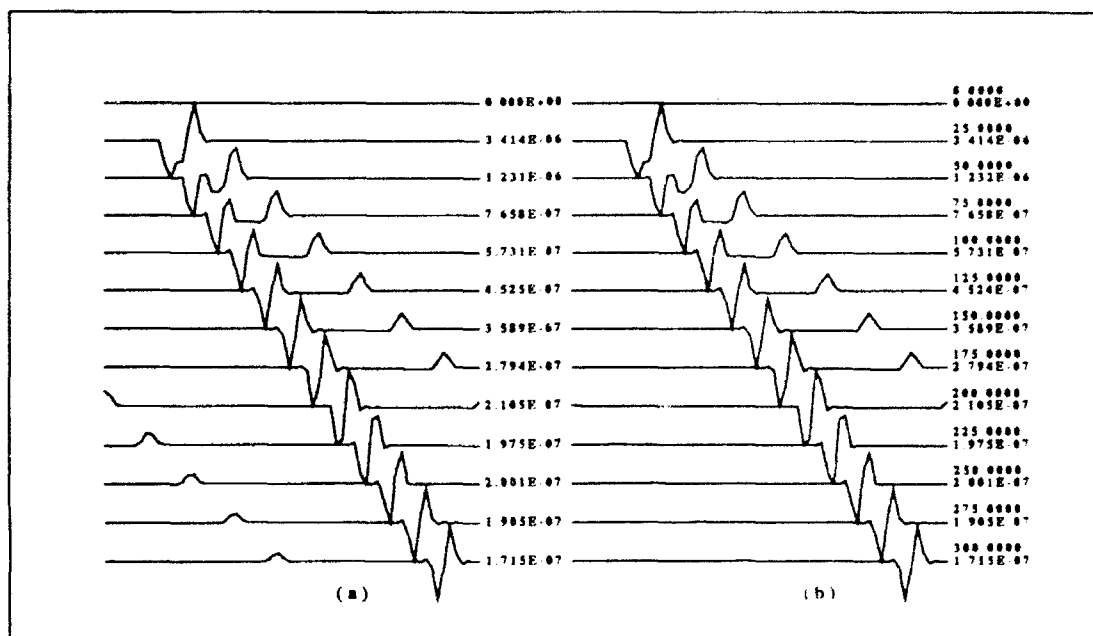


Fig. 3. Demonstration of the effect of the time domain damping factor, α : (a) $\alpha = 0.0$; (b) $\alpha = 0.04$. The RDD Green's function for a wholespace with $V_P = 6.0$ km/s, $V_S = 3.5$ km/s and $\rho = 2.8$ gm/cm³. The velocity traces (peak velocity in cm/s is shown) show the Green's functions at distances of 0 to 300 km for a source buried at 5 km beneath the receiver. All traces start at -5.0 seconds and end at 58.0 seconds. A triangular pulse with base of 4.0 seconds is used as the source wavelet.

The choice of α is not simple. First, if α is not large enough, then the wrapped signals will not be significantly reduced in amplitude. On the other hand, if α is too large, then the wavenumber integrands in Figure 1 may be so smoothed, that numerical integration noise may become important. For models without significant reverberations, e.g., thin surface water layers, reducing the wrapped amplitude by a factor of 10 will suffice. Thus if the time

window is $N\Delta t$ seconds long, choose α such that $\alpha N\Delta t = 2.3$. In the example just run, this product was 2.52.

WAVENUMBER INTEGRATION

The evaluation of the wavenumber integrals in (1) is complicated numerically. Numerical evaluation introduces error through the finite integration limits and through the particular integration rule used. These errors may appear in the time-distance domain as propagating arrivals or as noise unrelated to distance. Items of concern are the infinite limit of integration in wavenumber, the integration scheme used, and phase velocity filtering.

Infinite Limits

The problem is to approximate the infinite integral by a finite one. The obvious approach is to truncate the integral so that

$$\int_0^{\infty} f(k, r) dk \approx \int_0^{k_{\max}} f(k, r) dk,$$

but now the choice of k_{\max} becomes important, especially when the function $f(k, r)$ is significantly different from zero for $k > k_{\max}$.

To illustrate this, consider the REP function for an elastic wholespace (1j, 3h, and 4j)

$$\begin{aligned} \text{REP} &= -\frac{1}{4\pi\rho\alpha^2} \frac{\partial F_{\beta}}{\partial r} \\ &= \frac{1}{4\pi\rho\alpha^2} e^{-i\omega R/\alpha} \left[\frac{r}{R^3} + \left(\frac{i\omega}{v}\right) \frac{r}{R^2} \right] \\ &= \int_0^{\infty} \frac{k}{4\pi\rho\alpha^2 v_{\alpha}} e^{-v_{\alpha}|h|} J_1(kr) k dk \end{aligned}$$

The consideration in choosing k_{\max} is it must be large enough to give the desired signals. If the $|h|$ is not zero, then there will be some value of k_{\max} that together with the $|h|$ will reduce the integrand significantly so that the rest of the integral from $k = k_{\max}$ to $k = \infty$ can be successfully ignored.

Unfortunately, this cannot be done practically when $|h|$ is small. To handle this, one can make use of the asymptotic value of the integrand. Returning to the expression for REP, note that for large values of the wavenumber, that $v_{\alpha} \approx k$ and that the integral

$$\int_0^{\infty} \frac{1}{4\pi\rho\alpha^2} e^{-k|h|} J_1(kr) k dk = \frac{1}{4\pi\rho\alpha^2} \left[\frac{r}{R^3} \right].$$

This is just the expression for REP evaluated at $\omega = 0$. Note that for large values of the wavenumber, both integrands behave similarly. This suggests the following. If $g(k, r) \approx f(k, r)$ as $k \rightarrow \infty$, and if $\int_0^\infty g(k, r) dk = G(r)$, then

$$\int_0^\infty f(k, r) dk = \int_0^\infty [f(k, r) - g(k, r)] dk + G(r)$$

$$\int_0^\infty f(k, r) dk \approx \int_0^{k_{\max}} [f(k, r) - g(k, r)] dk + G(r)$$

where k_{\max} is such that now the integral

$$\int_{k_{\max}}^\infty [f(k, r) - g(k, r)] dk$$

is negligible.

There are now two choices to be made: the value of k_{\max} and whether or not to use the asymptotic integration trick.

The choice of k_{\max} requires a tradeoff between being accurate and being efficient. At low frequencies, the choice should depend on the vertical distance term, h . On the other hand, at high frequencies, the real part of $v_a |h|$ becomes large, and a frequency - depth dependent limit may be appropriate.

One strategy that seems to work and to be efficient is as follows: Define $|h|$ to be the absolute value of the difference in the source and receiver depths in the model. Also define H to be a mean thickness of layers in the model. Also let $k_{v_{\min}}$ be the wavenumber associated with the minimum wave velocity (usually the S-wave velocity, but may be the P-wave velocity of a fluid layer) at the current angular frequency ω and let $k_{v_{\min}}^U$ be the wavenumber associated with the minimum wave velocity but at the maximum desired frequency in the synthetics, ω_{\max} .

The steps are now as follow.

a) Estimate a test variable $k_m = \frac{5}{H} + \text{FAC } k_{v_{\min}}$.

b)

if $k_m h > 5$

$$k_1 = \frac{6.0}{|h|}$$

$$k_2 = \frac{2.5}{|h|}$$

$$k_{\max} = k_m$$

else

$$k_1 = 20k_{v_{min}}^U$$

$$k_2 = 5k_{v_{min}}^U$$

if $k_1|h| > 5$

$$k_1 = \frac{6.0}{|h|}$$

$$k_2 = \frac{5.0}{|h|} + 4k_{v_{min}}$$

$$k_{max} = k_2$$

if $k_{v_{min}} > k_1$

Do not use asymptotic integration technique

else

Do use asymptotic integration technique

The purpose of this logic is simple. If the user specified, frequency dependent upper limit, k_m , is large enough then the $\exp(-v_v|h|)$ term is small enough so that the truncation error is negligible. This technique is described in Apse and Luco (1983).

If this is not true, then use the asymptotic values to truncate the integral. Depending upon the particular Green's function, the function $g(k, r)$ is defined to be of the form $(A+Bk)\exp(-k|h|)$ or $(Bk+Ck^2)\exp(-k|h|)$. The two constants are estimated using the k_1 and k_2 values. The numbers 6.0 and 2.5 were chosen since $\exp(-6.0)$ and $\exp(-2.5)$ differ sufficiently to define the constants but neither is so small that one runs into lack of significance in using single precision arithmetic. The particular form chosen for k_m is designed to be economical at high frequency, but also to guarantee sufficient sampling at low frequencies.

When the difference in the source and receiver depths is small, using an upper limit proportional to $|h|^{-1}$ would lead to excessive computational effort. Thus a decision is made to tie the computations to the wavenumber of the highest frequency.

The FAC parameter also controls the upper limit, and requires some judgment. If FAC is made too small, then $\left(k_m^2 - k_v^2\right)^{1/2}$ will not be close enough to k_m , in which case a truncation error will introduce spurious low velocity arrivals. On the other hand, $FAC > 1$ is required to include a Rayleigh-wave pole. a $FAC = 3$ or 4 seems to work well.

If one considers the range of integration in the two-dimensional $\omega - k$ domain, a triangular region is sampled when $|h|$ is large, and a somewhat rectangular region when it is small. Since the upper wavenumber limit depends on the highest frequency, increasing the frequency content of a

signal, while keeping the length of the time series and the wavenumber sampling fixed, will increase the computational effort quadratically.

Bouchon Integration Scheme

Bouchon (1981) analyzed the use of a trapezoidal integration rule to evaluate the integrals in (1). Bouchon proved that

$$\sum_{n=0}^{\infty} \varepsilon_n f(k_n) J_m(k_n r) \Delta k = \int_0^{\infty} F(k) J_m(kr) dk + \int_0^{\infty} F(k) J_m(kr) \left\{ \sum_{n=1}^{\infty} 2(\cos(nkL)) \right\} dk$$

where $\Delta k = 2\pi/L$, $\varepsilon_0 = \frac{1}{2}$, $\varepsilon_j = 1$ for $j > 0$, and $k_n = n\Delta k$. By considering the Sommerfeld integral, it can be shown by large wavenumber approximations to the integrals that the cosine term introduces a sequence of noise arrivals corresponding to rings of sources at distances $L, 2L, \dots$, which introduce waves propagating toward and away from the origin. From this consideration, Bouchon (1981) recommended that the parameter, L , be chosen such that

$$L > 2r$$

and

$$\left[(L-r)^2 + z^2 \right]^{1/2} > vt,$$

where z is the vertical distance between the source and the receiver, r is the radial distance, t is the maximum time for which the trace is to be generated, and v is the velocity of the wave. When these rules are evaluated for a more complicated model, then the z represents the total vertical path of the last significant arrival and v is the fastest velocity. The choice of L is a matter of experiment.

Herrmann and Mandal (1986) modified the Bouchon (1981) expression by using a shifted rectangular rule because of the appearance of non-causal arrivals (a $k=0$ contribution) in some of the integrands, such as RDS. This noise arrival may be inherent to the use of a rectangular or trapezoidal rule, but may also be linked to the scheme used to truncating the limits of integration. They used

$$\sum_{n=0}^{\infty} \varepsilon_n f(k_n) J_m(k_n r) \Delta k = \int_0^{\infty} F(k) J_m(kr) dk$$

$$+ \int_0^{\infty} F(k) J_m(kr) \left\{ \sum_{n=1}^{\infty} 2 \cos(n(k - k_0)L) \right\} dk$$

where $\Delta k = 2\pi/L$, $\epsilon_0 = \frac{1}{2}$, $\epsilon_j = 1$ for $j > 0$, and $k_n = n\Delta k + k_0$. The value for k_0 was determined empirically to be $k_0 = 0.218\Delta k$.

Other Integration Schemes

The use of the Bouchon (1981) integration scheme is not computationally efficient at large distances and high frequencies, because of the required sampling in the $k-\omega$ domain. Another approach is to approximate the integrand by a higher order polynomial in the interval from k to $k + \Delta k$. If one part of the integrand is oscillatory, e.g., the Bessel function, then a Filon integration scheme can be developed. Apsel and Luco (1983) used a fourth order polynomial to model the non-oscillatory part of the integrand.

Mallick and Frazer (1987) suggested the use of Filon rule based on a linear approximation to the non-oscillatory part of the integrand. Thus if the integrand is of the form

$$\int_{k_1}^{k_2} F(k) e^{-ikr} dk,$$

it can be approximated in the case of $r \neq 0$ as

$$\frac{1}{r^2} \frac{\delta F(k)}{\delta k} \delta[e^{-ikr}] + \frac{i}{r} \delta[F(k) e^{-ikr}],$$

where $\delta X = X(k_2) - X(k_1)$. Mallick and Frazer (1987) and Saikia (1993) used this form together with the asymptotic expansion of the Bessel or Hankel functions to evaluate the wavenumber integrals of the type discussed in this paper.

Integrands for Large Offset

Bouchon's (1981) mathematical development demonstrated there can be inwardly propagating noise arrivals because of integrating the Bessel function. At large distances, r , cleaner seismograms may arise by using the following approximation:

$$\int_0^{\infty} F(k) J_m(kr) dk \approx \frac{1}{2} \int_{0+}^{\infty} F(k) H_m^{(2)}(kr) dk,$$

where $H_m^{(2)}(z)$ is the Hankel function of the second kind. This is a standard approximation, which can be justified from physical grounds that only outwardly propagating signals are desired. The mathematical justification arises from applying both the physical requirement and the stationary phase

approximation to drop the first order Hankel function from the identity

$$2J_m(z) = H_m^{(1)}(z) + H_m^{(2)}(z).$$

Phase Velocity Filtering

One final modification of the integrand is due to Fuchs and Müller (1971). This is the concept of computing synthetics with a range of phase velocities bounded by $[c_{\max}, c_1, c_2, c_{\min}]$. These can be used to define a window function, $W(k)$ defined by

$$W(k) = \begin{cases} 0 & k < \frac{\omega}{c_{\max}} \\ \frac{1}{2} \left(1 - \cos \left(\pi \frac{k - \frac{\omega}{c_{\max}}}{\frac{\omega}{c_1} - \frac{\omega}{c_{\max}}} \right) \right) & \frac{\omega}{c_{\max}} \leq k < \frac{\omega}{c_1} \\ 1 & \frac{\omega}{c_1} \leq k < \frac{\omega}{c_2} \\ \frac{1}{2} \left(1 - \cos \left(\pi \frac{k - \frac{\omega}{c_2}}{\frac{\omega}{c_2} - \frac{\omega}{c_{\min}}} \right) \right) & \frac{\omega}{c_2} \leq k < \frac{\omega}{c_{\min}} \\ 0 & k \geq \frac{\omega}{c_{\min}} \end{cases}$$

This windowing is useful if only a part of the seismogram corresponding with certain ray phase velocities is required is desired. When this is used, the upper limit in the integrand is defined by c_{\min} , and the parameter FAC and the asymptotic integral technique is not used. The use of the Hankel, rather than Bessel, function is recommended when phase velocity filtering is performed. The filtering will cause numerical noise, but will also have the advantage that the upper limit of wavenumber integration will be reduced, and hence the computations will be accomplished faster.

Examples

To illustrate these concepts, consider the RDD Green's function for a wholespace, (1b) and (3b). The model consists of P-velocity of 6.0 km/s, an S-velocity of 3.5 km/s, and a density of 2.8 gm/cm³. The source is 5 km beneath the receiver, and FAC = 3.0. A 128 point time series is generated with a sampling interval of 1.0 sec, and a triangular pulse with $\tau = 2.0$ sec is used to generate velocity time histories in units of cm/s for a source moment of 10²⁰ dyne-cm, at distances of 1 - 500 km. The time domain damping parameter $\alpha = 0.02$ so that the periodicity effect is reduced by a factor of $\exp(-2.54)$. The RDD Green's function is a good choice to illustrate the problems of numerical noise because the and S-wave arrival falls off more rapidly with distance than the P-wave arrival.

Figure 4 shows the time histories when $L = 250\text{km}$ is used. The Bouchon (1981) box bounded in distance by $L/2$ and in time by $L/2V_p$ is shown by the long dashed lines. This rectangular box is used since one often computes a record section rather than a single trace, and thus the size of the acceptable time window is constrained by the distance trace. The direct and wavenumber integration periodicity arrivals are indicated by the light solid and short dashed lines, with the latter indicating those arrivals that have been wrapped around due to the temporal periodicity properties. The extent of the periodicity problems is readily apparent, as is the fact that the signal within the Bouchon box is relatively clean. Part of the "simplicity" of the waveforms is due to the fact that the choice of α reduced the amplitude of the arrivals folded in time.

Figure 5 shows the same model, except that $L = 500\text{km}$. Because of the change in L , the Bouchon box becomes larger, and the seismograms are given to a larger distance. A P-wave noise arrival due to the temporal and spatial periodicity appears prior to the direct P-wave arrival. Figure 5 also shows some of the $k = 0$ noise at distances greater than 300 km at an arrival time of about 1 sec. This noise (Herrmann and Mandal, 1986) was reduced using the modified integration rule, but is a low frequency arrival, and is reduced further by making L smaller. Figure 6 is a similar plot, but uses a reduction velocity of 6.0 km/sec. The reduced travel time will provide a cleaner beginning of the trace history, but will not give any additional respite from the Bouchon condition.

Figure 7 shows the effect of using the Hankel function rather than the Bessel function together with a phase velocity filter. The phase velocity filter window of [16, 8, 2, 1] km/s was appropriate, since at large offset, the rays corresponding to P- and S-wave arrivals would propagate at 6.0 and 3.5 km/s respectively. The Hankel function was used in the integration when its argument, e.g., kr , was greater than 6.0. Otherwise the Bessel function is used. Since this can generate some low frequency noise near $k \approx 0$, the time domain damping parameter was set to $\alpha = 0.01$ rather than the $\alpha = 0.02$ used in the preceding figures. This reduces the amplitude of late arriving noise, but also increases the amplitude of the time domain periodicity noise.

There are two impressive points that can be made comparing Figures 6 and 7. First, the wavenumber integration synthetics, left side of Figure 7, agree very well with the analytic time histories, Figure 7 right, in the distance range of 25 - 350 km, and in the time window up to 83 seconds after the P-wave. This is significantly better in time and distance than the Bouchon window shown in Figure 6. This is in spite of the fact that the computational effort is roughly the same since in this case $FACk_{v_{min}} \approx \omega/1$. The implication is that if the range of interest were 1 - 250 km and the time window were still 41.67 sec, e.g., the Bouchon box, then it should be possible to use a smaller

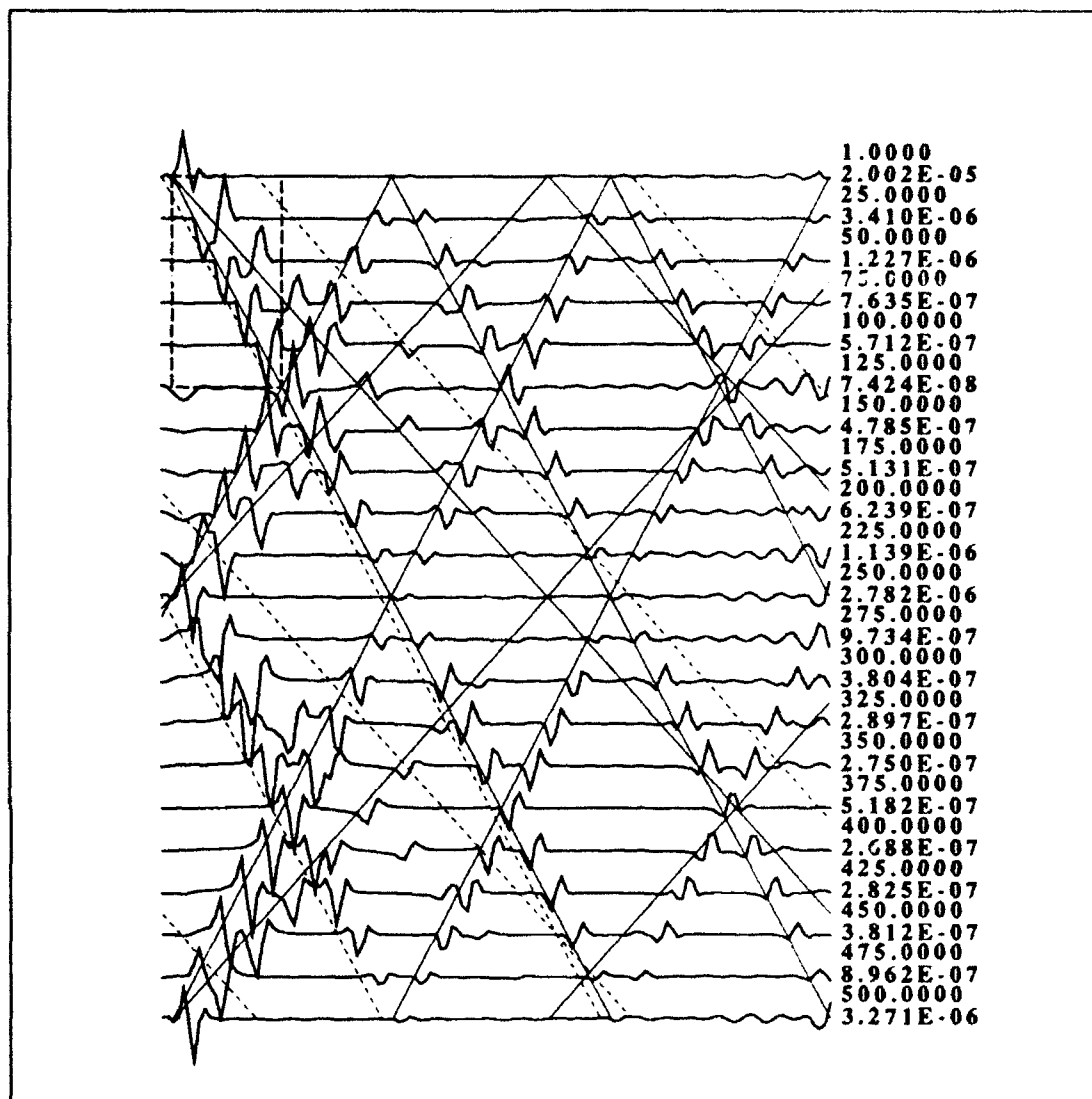


Fig. 4. RDD Green's functions for $L = 250$ km. All traces start at -2.0 sec and end at 125 sec. The distances and peak velocities (cm/s) are given to the right of each trace. The long dashed box shows the Bouchon window, the light solid lines indicate the direct arrivals and those expected from periodicity in space due to wavenumber integration, and the light short-dashed lines the folding of these arrivals due to the temporal periodicity due to the use of a discrete Fourier transform.

value of L to not only increase the time window but to also reduce the computation time.

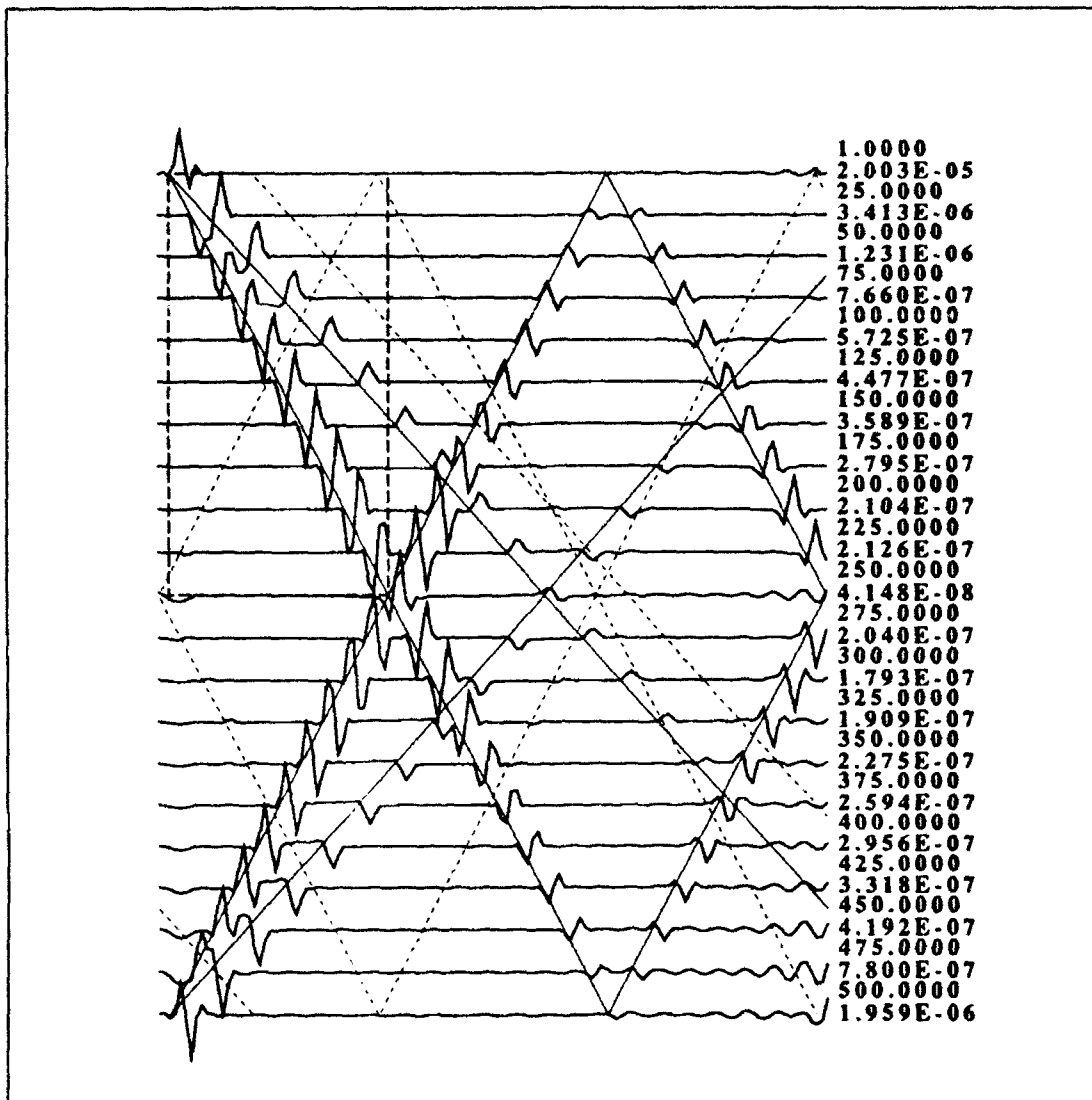


Fig. 5. RDD Green's functions for $L = 500$ km. All traces start at -2.0 sec and end at 125 sec. The distances and peak velocities (cm/s) are given to the right of each trace. The long dashed box shows the Bouchon window, the light solid lines indicate the direct arrivals and those expected from periodicity in space due to wavenumber integration, and the light short-dashed lines the folding of these arrivals due to the temporal periodicity due to the use of a discrete Fourier transform.

Guidance in Choosing Correct Parameters

If high frequency synthetic seismograms are desired, computer runs will necessarily be lengthy. The criteria for choosing the time-domain damping

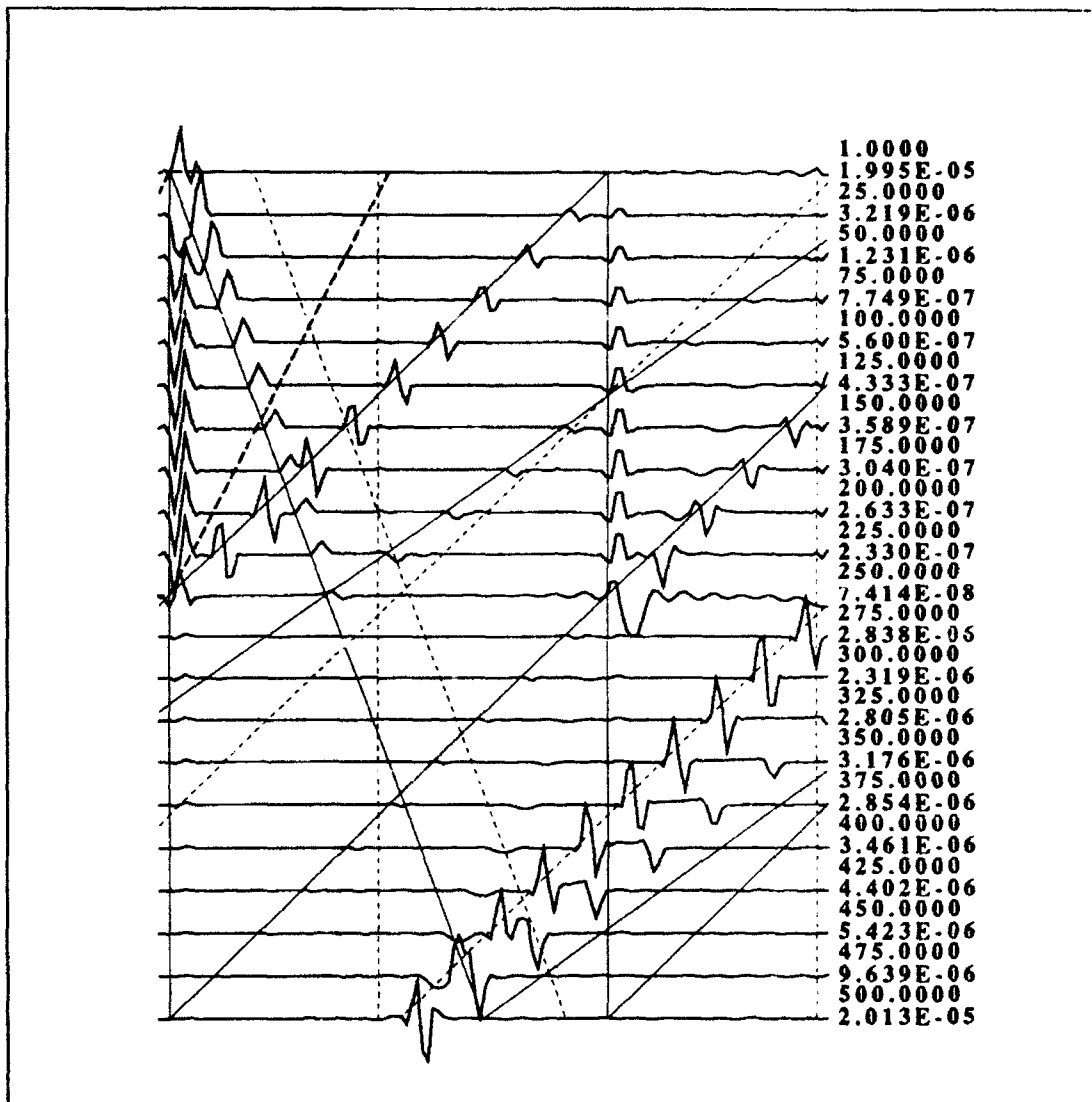


Fig. 6. RDD Green's functions for $L = 500$ km. A reduced travel time plot is used. The start time of each trace is $r/6.0 - 2.0$ seconds after the origin time; r is the epicentral distance in km. All traces are 123 seconds long. All traces start at The distances and peak velocities (cm/s) are given to the right of each trace. The long dashed box shows the Bouchon window, the light solid lines indicate the direct arrivals and those expected from periodicity in space due to wavenumber integration, and the light short-dashed lines the folding of these arrivals due to the temporal periodicity due to the use of a discrete Fourier transform.

parameter α is straightforward. The choice of the wavenumber sampling parameter L is not as simple. One useful technique used to settle upon a

the layer thicknesses. For a layered medium the propagator matrices contain hyperbolic sine and cosine terms when $k > k_v$, where V is either the P- or S-wave velocity. At high frequencies or large values of $v_v d$, where d is the layer thickness, the size of the hyperbolic terms can quickly exceed the size of floating point numbers in a computer.

This problem is handled very effectively by introducing an extended floating point notation. The SH propagator matrix, given in the Appendix, is of the form:

$$A(z) = \begin{bmatrix} \cosh X & b \sinh X \\ a \sinh X & \cosh X \end{bmatrix}$$

For large values of X , this can be rewritten as

$$A(z) = \frac{1}{2} e^X \begin{bmatrix} \begin{pmatrix} 1 + e^{-2X} \end{pmatrix} & b \begin{pmatrix} 1 - e^{-2X} \end{pmatrix} \\ a \begin{pmatrix} 1 - e^{-2X} \end{pmatrix} & \begin{pmatrix} 1 + e^{-2X} \end{pmatrix} \end{bmatrix}$$

Note that now the exponential terms within the matrix will now only underflow, and can be set to zero when X is sufficiently large. However, the leading e^X term is not multiplied, but the X value is saved. The $A(z)$ matrix will now look like

$$A(z) = e^X A'(z)$$

and matrix multiplication of two such propagators will give

$$A(z_1)A(z_2) = e^{X_1+X_2} A'(z_1)A'(z_2)$$

Computationally a "modified matrix product" is saved as are the $\sum X_i$. Since the expression for receiver displacements for SH waves (38) is a ratio of two sets of propagator matrices, the resultant expression will look like

$$U_s = e^{\sum \text{NUM}_i - \sum \text{DEN}_i} \text{well_defined_number.}$$

If the exponential term is too small, U_s is set to zero.

This artifice works well. However, there is an assumption inherent in the use of (38) or (19) or (20), and that is that the exponential eigenfunctions always decrease from the source to the receiver, since the propagators are taken from the base of the layer stack to the surface and the above factorization assumes that they increase upwards. Thus there may be some problems with sme models having low velocity zones.

Another computational problem arises with the use of propagator matrices. Harkrider (personal communication) mentioned the inherent instability of the compound P-SV matrices at low frequencies. While this may be a

problem in single precision, we have not found it to be so when computations are performed in double precision.

REFERENCES

- Apsel, R. J., and J. E. Luco (1983). On the Green's functions for a layered half-space. Part II., *Bull. Seism. Soc. Am.* **73**, 931-951.
- Bouchon, M. (1981). A simple method to calculate Green's functions for elastic layered media, *Bull. Seism. Soc. Am.* **71**, 959-971.
- Brigham, E. O. (1974). *The Fast Fourier transform*, Prentice-Hall, Englewood Cliffs.
- Fuchs, K., and G. Müller (1971). Computation of synthetics seismograms with the reflectivity method and comparison with observations, *Geophys. J.* **23**, 417-433.
- Haskell, N. A. (1963). Radiation patters of Rayleigh waves from a fault of arbitrary dip and direction of motion in a homegeneous medium, *Bull. Seism. Soc. Am.* **53**, 619-642.
- Haskell, N. A. (1964). Radiation pattern of surface waves from point sources in a multi-layered medium, *Bull. Seism. Soc. Am.* **54**, 377-393.
- Herrmann, R. B. (1975). A student's guide to the use of P and S wave data for focal mechanism determination, *Earthquake Notes* **46**, 29-40.
- Herrmann, R. B., and B. Mandal (1986). A study of wavenumber integration techniques, *Earthquake Notes* **57**, 33-40.
- Herrmann, R.B., and C. Y. Wang (1985). A comparison of synthetic seismograms, *Bull. Seism. Soc. Am.* **75**, 41-56.
- Hudson, J. A. (1969). A quantitative evaluation of seismic signals at teleseismic distances - I. Radiation from point sources. *Geophys. J. Roy. astr. Soc.* **18**, 233-239.
- Kennett, B. L. N. (1983). *Seismic Wave Propagation in Stratified Media*, Cambridge University Press, Cambridge.
- Mallick, S., and L. N. Frazer (1987). Practical aspects of reflectivity modeling, *Geophysics* **52**, 1355-1364.

- Phinney, R. A. (1965). Theoretical calculation of the spectrum of first arrivals in layered elastic mediums, *J. Geophys. Res.* **70**, 5107-5123.
- Pujol, J., and R. B. Herrmann (1990). A student's guide to point sources in inhomogeneous media, *Seism. Res. Letters* **61**, 209-224.
- Saikia, C. K. (1993). Modified frequency-wavenumber algorithm for regional seismograms using Filon's quadrature - Modeling of Lg waves in eastern North America, *Geophys. J. Int.* (in review).
- Wang, C. Y., and R. B. Herrmann (1980). A numerical study of P-, SV-, and SH-wave generation in a plane layered medium, *Bull. Seism. Soc. Am.* **70**, 1015-1036.
- Watson, T. H. (1970). A note on fast computation of Rayleigh wave dispersion in the multi-layered elastic half-space, *Bull. Seism. Soc. Am.* **60**, 161-166.

APPENDIX

P-SV Propagator

The components of the 4x4 P-SV propagator from Haskell (1964) are as follow:

$$a_{11} = \gamma \cosh v_\alpha z - (\gamma - 1) \cosh v_\beta z$$

$$a_{12} = -(\gamma - 1) \sinh v_\alpha z / v_\alpha + \gamma v_\beta \sinh v_\beta z / k^2$$

$$a_{13} = -(\cosh v_\alpha z - \cosh v_\beta z) / \rho$$

$$a_{14} = \left((k^2 \sinh v_\alpha z / v_\alpha - v_\beta \sinh v_\beta z) \right) / \rho$$

$$a_{21} = \gamma v_\alpha \sinh v_\alpha z - k^2 (\gamma - 1) \sinh v_\beta z / v_\beta$$

$$a_{22} = -(\gamma - 1) \cosh v_\alpha z + \gamma \cosh v_\beta z$$

$$a_{23} = \left(-v_\alpha \sinh v_\alpha z + k^2 \sinh v_\beta z / v_\beta \right) / \rho$$

$$a_{24} = -k^2 a_{13}$$

$$a_{31} = \rho \gamma (\gamma - 1) (\cosh v_\alpha z - \cosh v_\beta z)$$

$$a_{32} = \rho \left(-(\gamma - 1)^2 \sinh v_\alpha z / v_\alpha + \gamma^2 v_\beta \sinh v_\beta z / k^2 \right)$$

$$a_{33} = a_{22}$$

$$a_{34} = -k^2 a_{12}$$

$$a_{41} = \rho \gamma^2 v_\alpha \sinh v_\alpha z / k^2 - \rho (\gamma - 1)^2 \sinh v_\beta z / v_\beta$$

$$a_{42} = -a_{31} / k^2$$

$$a_{43} = -a_{21} / k^2$$

$$a_{44} = a_{11}$$

The compound matrix of a 4x4 matrix, a_{ij} is a 6x6. However, the structure of the compound matrix $A|_{kl}^{\bar{ij}} = a_{ik} a_{jl} - a_{il} a_{jk}$, permits a reduction to a 5x5

matrix, (Watson, 1970), which reduces the number of matrix multiplications required. Associating compound matrix doublets (12, 13, 14, 23, 24, 34), with the indices {1, 2, 3, 4, 5, 6}, and defining $A_{ij} = A|_{ij}^{(ij)}$, using the above mapping, we see that

$$A_{3j} = -A_{4j} / k^2, \quad j \neq 3, 4$$

$$A_{i3} = -k^2 A_{i4}, \quad j \neq 3, 4$$

$$A_{33} = A_{44},$$

$$A_{34} = -(A_{44} - 1) / k^2$$

In addition, $A_{ij} = A_{7-j, 7-i}$ for $i = 2$ to 6 and $j = 8 - i$ to 6.

When this matrix is multiplied by a vector, e.g., the elements of the compound **H** matrices, we note that the third element of the product, G_3 , is related to the fourth element, G_4 , by the relation $G_3 = -k^2 G_4$. For the compound **H** matrix, the third and fourth elements are related by $H_4 = -k^2 H_3$. The 1x6 and 6x6 multiplication, $G^T A$ yields the same results as multiplying a 1x5 by a 5x5, $G'^T A'$ if we do the following to the **G** vector and the **A** matrices:

- Drop the third element of the compound **G**.
- Drop the third row and column of **A** to form the initial 5x5.
- Multiply the off diagonal elements of the third row of the new **A'** by 2.
- Define the third diagonal element $A'_{33} = 2A_{44} - 1$.

Thus the original 6x6 compound matrix

$$A = \begin{bmatrix} a_{11} & a_{12} & a_{13} & a_{14} & a_{15} & a_{16} \\ a_{21} & a_{22} & a_{23} & a_{24} & a_{25} & a_{26} \\ a_{31} & a_{32} & a_{33} & a_{34} & a_{35} & a_{36} \\ a_{41} & a_{42} & a_{43} & a_{44} & a_{45} & a_{46} \\ a_{51} & a_{52} & a_{53} & a_{54} & a_{55} & a_{56} \\ a_{61} & a_{62} & a_{63} & a_{64} & a_{65} & a_{66} \end{bmatrix}$$

becomes

$$A' = \begin{bmatrix} a_{11} & a_{12} & a_{14} & a_{15} & a_{16} \\ a_{21} & a_{22} & a_{24} & a_{25} & a_{26} \\ 2a_{41} & 2a_{42} & 2a_{44} - 1 & 2a_{45} & 2a_{46} \\ a_{51} & a_{52} & a_{54} & a_{55} & a_{56} \\ a_{61} & a_{62} & a_{64} & a_{65} & a_{66} \end{bmatrix}$$

The original compound

$$\mathbf{G} = \begin{bmatrix} g_{11}, g_{12}, g_{13}, g_{14}, g_{15}, g_{16} \end{bmatrix}$$

becomes

$$\mathbf{G}' = \begin{bmatrix} g_{11}, g_{12}, g_{14}, g_{15}, g_{16} \end{bmatrix},$$

and the original compound

$$\mathbf{H}^T = \begin{bmatrix} h_{11}, h_{21}, h_{31}, h_{41}, h_{51}, h_{61} \end{bmatrix}$$

becomes

$$\mathbf{H}'^T = \begin{bmatrix} h_{11}, h_{21}, 2h_{41}, h_{51}, h_{61} \end{bmatrix}.$$

We will compute the propagators using the primed matrices. To evaluate (19) or (20), we can quickly define the needed unprimed vector from

$$\begin{bmatrix} r_1 \\ r_2 \\ r_3 \\ r_4 \\ r_5 \\ r_6 \end{bmatrix} = \begin{bmatrix} r'_1 \\ r'_2 \\ -k^2 r'_3 \\ r'_3 \\ r'_4 \\ r'_5 \end{bmatrix}$$

The elements of the modified 5x5 compound propagator matrix are as follow:

$$A'_{11} = \text{CPCQ} - (A'_{33} - 1)/2$$

$$A'_{12} = (-\text{CQX} + k^2 \text{CPY})/\rho$$

$$A'_{13} = -[(2\gamma - 1)(1 - \text{CPCQ}) + \gamma \text{XZ}/k^2 + (\gamma - 1)k^2 \text{WY}]/\rho$$

$$A'_{14} = (\text{CPZ} - k^2 \text{CQW})/\rho$$

$$A'_{15} = -[2(1 - \text{CPCQ})k^2 + \text{WY}k^4 + \text{XZ}]/\rho^2$$

$$A'_{21} = \rho[-(\gamma - 1)^2 \text{CQW} + \gamma^2 \text{CPZ}/k^2]$$

$$A'_{22} = \text{CPCQ}$$

$$A'_{23} = -[(\gamma - 1)\text{CQW} - \gamma \text{CPZ}/k^2]$$

$$A'_{24} = -\text{WZ}$$

$$A'_{25} = A'_{14}$$

$$A'_{31} = 2\rho[\gamma(\gamma-1)(2\gamma-1)(1-CPCQ) + \gamma^3 XZ/k^2 + (\gamma-1)^3 k^2 WY]$$

$$A'_{32} = 2[\gamma CQX - k^2(\gamma-1)CPY]$$

$$A'_{33} = 1 + 2[2\gamma(\gamma-1)(1-CPCQ) + \gamma^2 XZ/k^2 + (\gamma-1)^2 k^2 WY]$$

$$A'_{34} = -2k^2 A'_{23}$$

$$A'_{35} = -2k^2 A'_{13}$$

$$A'_{41} = \rho[-\gamma^2 CQX/k^2 + (\gamma-1)^2 CPY]$$

$$A'_{42} = -XY$$

$$A'_{43} = -\frac{1}{2} A'_{32}/k^2$$

$$A'_{44} = A'_{22}$$

$$A'_{45} = A'_{12}$$

$$A'_{51} = -\rho^2 \left[(\gamma-1)^2 \left(2(1-CPCQ)\gamma^2 + (\gamma-1)^2 WYk^2 \right) + \gamma^4 XZ/k^2 \right] / k^2$$

$$A'_{52} = A'_{41}$$

$$A'_{53} = -\frac{1}{2} A'_{31}/k^2$$

$$A'_{54} = A'_{21}$$

$$A'_{55} = A'_{11}$$

where we define

$$CPCQ = \text{COSP} * \text{COSQ}$$

$$CPY = \text{COSP} * Y$$

$$CPZ = \text{COSP} * Z$$

$$CQW = \text{COSQ} * W$$

$$CQX = \text{COSQ} * X$$

$$XY = X * Y$$

$$XZ = X * Z$$

$$WY = W * Y$$

$$WZ = W * Z$$

and

$$\begin{aligned} \text{COSP} &= \cosh v_\alpha z & X &= v_\alpha \sinh v_\alpha z \\ \text{COSQ} &= \cosh v_\beta z & Y &= \sinh v_\beta z / v_\beta \\ W &= \sinh v_\alpha z / v_\alpha & Z &= v_\beta \sinh v_\beta z \end{aligned}$$

For a fluid layer, the values of the vertical displacement and stress must be propagated, but reduce the need for complicated *if* constructs in the program, the radial stress and displacement values are propagated unchanged in this modified matrix. The true 2x2 propagator matrix for a fluid consists of the inner 2x2 submatrix. The propagator used is as follows:

$$a(z) = \begin{bmatrix} 1 & 0 & 0 & 0 \\ 0 & \cosh v_\alpha z & -v_\alpha \sinh v_\alpha z / \rho & 0 \\ 0 & -\rho \sinh v_\alpha z / v_\alpha & \cosh v_\alpha z & 0 \\ 0 & 0 & 0 & 1 \end{bmatrix}$$

The corresponding 5x5 modified compound propagator matrix is

$$A(z) = \begin{bmatrix} \cosh v_\alpha z & -v_\alpha \sinh v_\alpha z / \rho & 0 & 0 & 0 \\ -\rho \sinh v_\alpha z / v_\alpha & \cosh v_\alpha z & 0 & 0 & 0 \\ 0 & 0 & 1 & 0 & 0 \\ 0 & 0 & 0 & \cosh v_\alpha z & -\rho \sinh v_\alpha z / v_\alpha \\ 0 & 0 & 0 & -v_\alpha \sinh v_\alpha z / \rho & \cosh v_\alpha z \end{bmatrix}$$

SH Propagator

The components of the 2x2 SH propagator follow the Herrmann (1979) modification of the Haskell (1964) matrices to factor out an apparent singularity at $\omega = 0$:

$$A(z) = \begin{bmatrix} \cosh v_\beta z & \sinh v_\beta z / \rho \beta^2 v_\beta \\ \rho \beta^2 v_\beta \sinh v_\beta z & \cosh v_\beta z \end{bmatrix}$$

If the top or bottom layers of the structure are fluid, a *pseudo*-propagator is introduced for SH to avoid the use of complicated *if* structures in the source program with the following matrix:

$$A(z) = \begin{bmatrix} 1 & 0 \\ 0 & 1 \end{bmatrix}$$

Functional Form of Integrands as $\omega \rightarrow 0$ or $k \gg k_{v_{\min}}$

Explicit expressions for the earthquake and explosion double couples for surface receiver and a buried source in a halfspace were given by Herrmann and Wang (1985). This required care in taking the limits of all the terms in

the specific expressions.

For each Green's functions, we may wish to evaluate an integral of the form:

$$J_n K_m = \int_0^{\infty} k^m e^{-kh} J_n(kr) dk .$$

Specific forms can be found by integration and differentiation of the Sommerfeld integral with respect to r or z .

For the Green's functions, the asymptotic form was evaluated, and since only two wavenumber values, k_1 and k_2 , are used, two constants are defined needed. In addition, F_{12} and F_{16} vary as k^{-1} for large k . To handle this case stably the asymptotic fit is made to kF_{12} and to kF_{16} . Table A.1 shows the particular asymptotic coefficients evaluated. The lowest order term is k is that which results from taking the limits. By combining this table with the expression in (1), the necessary integrals are defined.

Table A.1. Functional fit to asymptotic trend

F_j	Asymptotic Fit	Function Fit
F_1	$(Bk + Ck^2)e^{-kh}$	F_1
F_2	$(A + Bk)e^{-kh}$	F_2
F_3	$(Bk + Ck^2)e^{-kh}$	F_3
F_4	$(A + Bk)e^{-kh}$	F_4
F_5	$(Bk + Ck^2)e^{-kh}$	F_5
F_6	$(A + Bk)e^{-kh}$	F_6
F_7	$(Bk + Ck^2)e^{-kh}$	F_7
F_8	$(A + Bk)e^{-kh}$	F_8
F_9	$(Bk + Ck^2)e^{-kh}$	F_9
F_{10}	$(A + Bk)e^{-kh}$	F_{10}
F_{11}	$(Bk + Ck^2)e^{-kh}$	F_{11}
F_{12}	$(A + Bk)e^{-kh}$	kF_{12}
F_{13}	$(A + Bk)e^{-kh}$	F_{13}
F_{14}	$(A + Bk)e^{-kh}$	F_{14}
F_{15}	$(A + Bk)e^{-kh}$	kF_{15}
F_{16}	$(Bk + Ck^2)e^{-kh}$	F_{16}

The necessary integrals are

n	m	JnKm
0	0	$\frac{1}{R}$
0	1	$\frac{R^3}{2h^2 - r^2}$
0	2	$\frac{R^5}{6z^3 - 9zr^2}$
0	3	$\frac{R^7}{R^7}$
1	-1	$\frac{r}{h + R}$
1	0	$\frac{1}{r} \left(1 - \frac{h}{R} \right)$
1	1	$\frac{R^3}{3hr}$
1	2	$\frac{R^5}{12rh^2 - 3r^3}$
1	3	$\frac{R^7}{R^7}$
2	0	$\frac{1}{R} \left(\frac{r}{h + R} \right)^2$
2	1	$\frac{1}{R^2} \left(1 - \frac{h}{R} \right)^2 \left(2 + \frac{h}{R} \right)$
2	2	$\frac{3r^2}{R^5}$
2	3	$\frac{15hr^2}{R^7}$

$$R^2 = r^2 + h^2$$

(This Page Blank)

SPECTRAL EXAMINATION OF THE 16 JUNE 1992 EARTHQUAKE AND QUARRY BLAST NEAR EVANSVILLE, INDIANA

K.D. Hutchenson and R.B. Herrmann

ABSTRACT

On 16 June 1992, an m_{Lg} 2.3 earthquake occurred in southwestern Indiana, near Evansville. This area is part of the Illinois Basin coal belt, an area of active surface mines with numerous strip-mine blasts daily. The co-location of earthquakes and strip-mine blasts enable spectral comparisons without significant concern for differences due to path propagation effects.

Discriminating between the two types of events can be done visually due to the distinctive appearance of the Rg phase in strip-mine blasts and high frequency coda of earthquakes. A strong Rg phase is indicative of shallow source depths. However, earthquakes previously located at shallow depths elsewhere within the Illinois Basin do not exhibit a distinctive Rg phase, indicating either poor control in focal depth determination or a fundamental difference in source mechanism. Visual and spectral examination shows that earthquakes are richer in energy at higher frequencies than strip-mine blasts. Earthquakes have significant energy at 20-30 Hz, while the significant energy content of blasts is closer to 10 Hz. The significant difference compared to previous earthquake-nuclear explosion discriminant studies is that the chemical explosion has reduced high frequency content compared to the earthquake.

INTRODUCTION

On 16 June 1992, an m_{Lg} 2.3 earthquake occurred in southwestern Indiana near Evansville. The earthquake was recorded by the Central Mississippi Valley Seismic Network (CMVSN) (Figure 1). Although this area is not as seismically active as the New Madrid Seismic Zone to the southwest, small earthquakes ($1.7 \leq m_{Lg} \leq 2.9$) are not infrequent, averaging one instrumentally located event every thirteen months since September 1982. This study was prompted by the fortuitous co-location of the 16 June earthquake (only the third digitally recorded earthquake located in this area) with a nearby strip-mine blast of similar size (m_{Lg} 2.65) which occurred just hours after the earthquake (Figure 2).

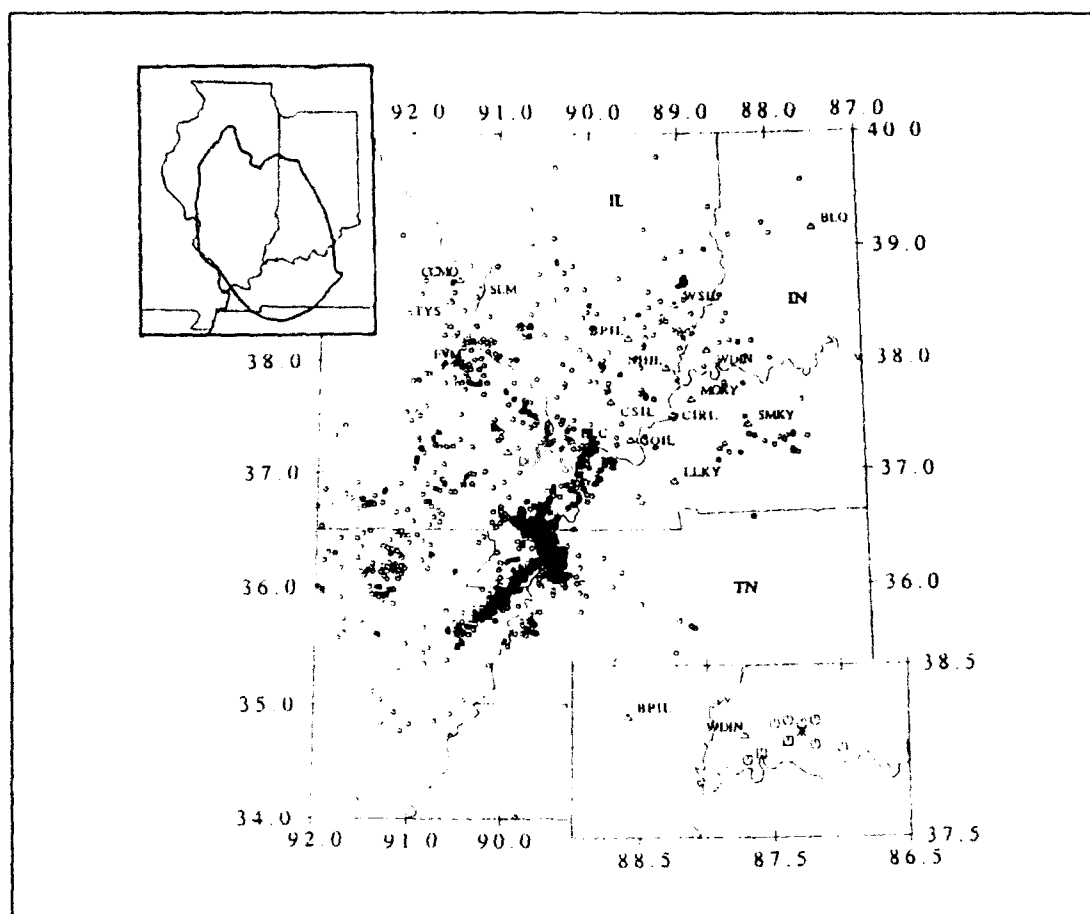


Fig. 1. Seismicity map for the New Madrid Seismic Zone, Illinois Basin, and surrounding areas showing the CMVSN stations. Two insets show the Illinois Basin outline (after Collinson *et al.*, 1988) and the area of study in eastern Illinois and southwestern Indiana (circles (o) show prior seismicity, with the two squares (□) denoting the 1 May 1985 and 16 June 1992 events; asterisks (*) show two strip mine blasts at the same location.

The primary purpose of this paper is to examine the distinguishing features between the earthquake (19:28:49.0 UT) and strip-mine blast (23:11:13.6 UT) of 16 June 1992 (Figure 1) on the basis of several attributes, including spectral differences. In addition, these results will be compared with similar events, both in the immediate area and elsewhere within the Illinois Basin. It will be shown that differentiating between these earthquakes and strip-mine blasts within the Illinois Basin is rather trivial.

The intent of this study is not to blindly apply regional nuclear explosion-earthquake discrimination results from other areas (*e.g.* Pomeroy *et al.*,

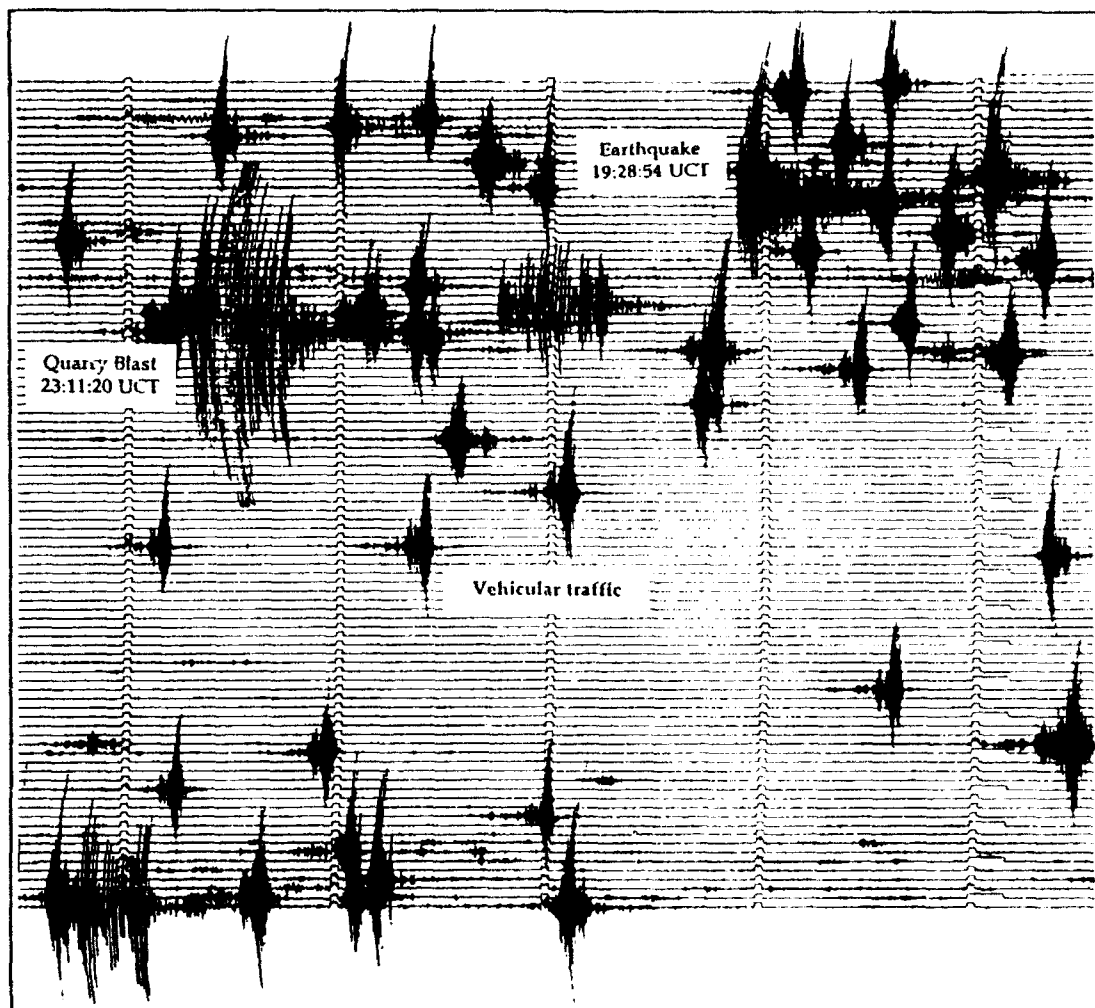


Fig. 2. WDIN analog record segment of 16 June 1992 showing the earthquake and several strip-mine blasts. The events with the low frequency "tail" (coda) are strip-mine blasts (three within 50 km; three more farther away). As shown by this seismogram segment, strip-mine blasts and earthquakes are quite different in appearance, primarily in the appearance of the surface wave with respect to the body wave arrivals. The majority of the "events" on this record are associated with vehicular traffic.

1982; Bennett and Murphy, 1986; Taylor *et al.*, 1989), but to examine observed characteristics which may aid in separating these two events. The differences are due to the nature of the source; low yield nuclear explosions are considered point sources while large strip-mine blasts are a series of sources. However, this area would provide a good test case for more detailed work, in that events have both similar size (m_{Lg}) and location, except for

depth. Discrimination studies undertaken elsewhere within the Illinois Basin and the New Madrid seismic zone have examined the classical discriminants (Amjad, 1991).

DESCRIPTION OF THE STUDY AREA

The Illinois Basin (600 km by 320 km) is located primarily in Illinois, extending into Indiana, and Kentucky (Collinson *et al.*, 1988) (Figure 1). The Paleozoic sedimentary fill (primarily carbonates with lesser amounts of siltstone/shale and sandstones) range in age from Early/Middle Cambrian to Early Permian. Parts of the basin are capped by Pleistocene loess deposits of varying thickness (Willman and Frye, 1970). The thickest sediments are along the southern border of the basin, in central and southern Illinois, southwestern Indiana, and western Kentucky, thinning both depositionally and erosionally towards the basin boundaries.

The Wabash River (boundary between Illinois and Indiana) area has been examined in prior geological and geophysical studies (Bristal and Buschbach, 1971; Bristal and Treworgy, 1979; Ault and Sullivan, 1982; Ault *et al.*, 1985; Nelson and Bauer, 1987). Many high-angle normal faults have been mapped trending NNE, subparallel to the Wabash River. Offsets along the faults may diminish with depth (Sexton *et al.*, 1988).

Seismic activity has been reported in the eastern Illinois, western Indiana area since the 1800's (Nuttli, 1983). The Wabash River Seismic Zone (WRSZ) was identified as a result of the seismic activity and the many mapped faults (Nuttli and Brill, 1981). The WRSZ has been considered a source zone in terms of hazard analysis (Barstow *et al.*, 1981). However, recent work (Taylor, 1991) has argued that the WRSZ is not a separate zone and should be included together with eastern Illinois as one zone. Seismic activity in eastern Illinois, including the largest event recorded by the CMVSN (Taylor *et al.*, 1989), may be associated with basement structures in the region (Hamburger and Rupp, 1988; Pratt *et al.*, 1989; Taylor, 1991).

In addition to the historical and instrumentally located seismic activity along the Wabash River, there are numerous strip mine blasts. Surface mines are quarrying coal from Pennsylvanian deposits (Hasenmueller and Carr, 1983; Hasenmueller and Wiegand, 1980 (rev. 1985); Harper, 1985). Many artificial events are recorded by the CMVSN on a weekly basis.

DATA PROCESSING AND RESULTS

Figure 1 shows the seismic activity in the New Madrid Seismic Zone and Illinois Basin area. Insets show the study area in southwestern Indiana and eastern Illinois, with the located seismicity and several strip-mine blasts. Also shown are the CMVSN stations, especially WDIN and BPIL, which are

used in the following analysis. WDIN (Wadesville, IN), is located approximately 40 km from the active strip mines, while BPIL (Belle Praise, IL) is farther away, nearly 100 km from the active mines.

Table 1
Station Locations

Station	Location	Lat (°N)	Lon (°W)
BPIL	Belle Praise, IL	38.20	88.59
CCMO	Creve Coeur, MO	38.72	90.47
CSIL	Creal Springs, IL	37.63	88.79
CIRL	Cave In Rock, IL	37.51	88.11
DON	Dongola, MO	37.18	89.93
ELC	Elco, IL	37.28	89.23
FVM	French Village, MO	37.98	90.43
GOIL	Rosebud, IL	37.29	88.58
NHIL	New Haven, IL	37.93	88.17
SLM	St. Louis, MO	38.64	90.24
TYS	Tyson Valley, MO	38.53	90.57
WDIN	Wadesville, IN	38.09	87.72
WDIL	West Salem, IL	38.50	88.07

While several permanent CMVSN stations are located along the Wabash River, most lie on the Illinois side (Table 1). The network has been in operation since 1974. All sites have vertical component seismometers (L4-C's) except for FVM and SLM which have three component Benioff seismometers. Data are telemetered to St. Louis University where they are digitized at 100 Hz.

Table 2 lists the parameters of all seismicity recorded in the study area, in addition to several strip-mine blasts. Only three of the earthquakes were digitally recorded. Of these, two are used in this study; the 13 February 1987 event is virtually unusable due to poor signal-to-noise.

Two digitally recorded earthquakes (1 May 1985 and 16 June 1992) and two recent strip-mine blasts of similar size are examined in this study. Each event was located using a version of FASTHYPO (Herrmann, 1979a) with the UPLANDS velocity model (Stauder *et al.*, 1991) and available CMVSN stations (Table 1 and Figure 1). In addition, station BLO (Bloomington, IN) reported phase data for several of the events (M. Hamburger, pers. comm.), as did several Kentucky stations (LLKY, MOKY, SMKY, and SOKY) (R. Street, pers. comm.), aiding in their location, especially with depth. Due to the station geometry, error ellipses for all events, both blasts and earthquakes in the Wabash River Valley, are generally oriented in a NE-SW direction.

Table 2
Earthquakes and strip mine blasts in southwestern Indiana

Date	Time) (UT)	Lat (°N)	Lon (°W)	Depth (km)	m _b	comments
2 Sep 1982	11:30:59.3	37.95	87.75	12.0	1.3	analog only
4 Jun 1984	19:16:48.9	38.02	87.03	5.0	2.3	analog only
30 Jul 1984	12:57:25.7	38.16	87.37	10.0	1.7	analog only
1 Sep 1984	18:27:44.2	38.04	87.29	10.0	1.8	analog only
1 May 1985	01:16:27.9	37.99	87.61	1.4	2.9	digital *
10 Jan 1986	19:54:52.0	38.16	87.58	10.0	2.5	analog only
13 Feb 1987	16:44:51.2	38.18	87.47	5.0	2.5	digital
16 Feb 1987	16:27:06.2	38.18	87.22	5.0	2.5	analog only
16 Jun 1992	19:28:49.0	38.06	87.46	2.0	2.3	digital *
16 Jun 1992	23:11:13.6	38.11	87.39	0.1	2.65	strip mine blast *
24 Jul 1992	15:23:15.4	38.11	87.31	0.1	2.50	strip mine blast *

* relocated with CMVSN, BLO, and KY stations; however depths are from archive files

Each of the four events selected for further processing were relocated as part of this study. When only the CMVSN stations were used, the earthquakes relocated with depths between 10-12 km and the strip-mine blasts at 0.0 km (at the surface). After adding BLO and the Kentucky stations, it was interesting to note that the earthquakes relocated at relatively shallow depths (≈ 2.0 km) while the strip-mine blasts located at much deeper depths (6-12 km) (Table 2). The velocity model for this area will need to be improved to accurately determine depths to the earthquakes without portable stations in the field.

Waveforms for the four selected events are shown in Figure 3 for stations WDIN and BPIL. Each trace is preceded by 1.0 second of background noise prior to the P-wave arrival. Strip-mine blasts occurring in the Illinois Basin are distinctive and easily recognizable from earthquakes (Figure 2 and Figure 3). All have a low-frequency Rg phase (a fundamental mode surface wave with a period of 0.25 to 3.0 seconds), usually with a larger amplitude Airy phase. Higher mode Rg phases are occasionally discernible in the time series. The shape of the Rg phase coda varies with distance and source location (due to differences in sediment thickness) within the Illinois Basin (Hutchenson *et al.*, 1990; Hutchenson and Herrmann, 1991). A distinctive Rg phase and coda are characteristic of shallow-source events (Båth, 1975; Shapiro, 1988; Kafka, 1990). Strip-mine blasts in open-pit mines are shallow source events, although not necessarily point sources.

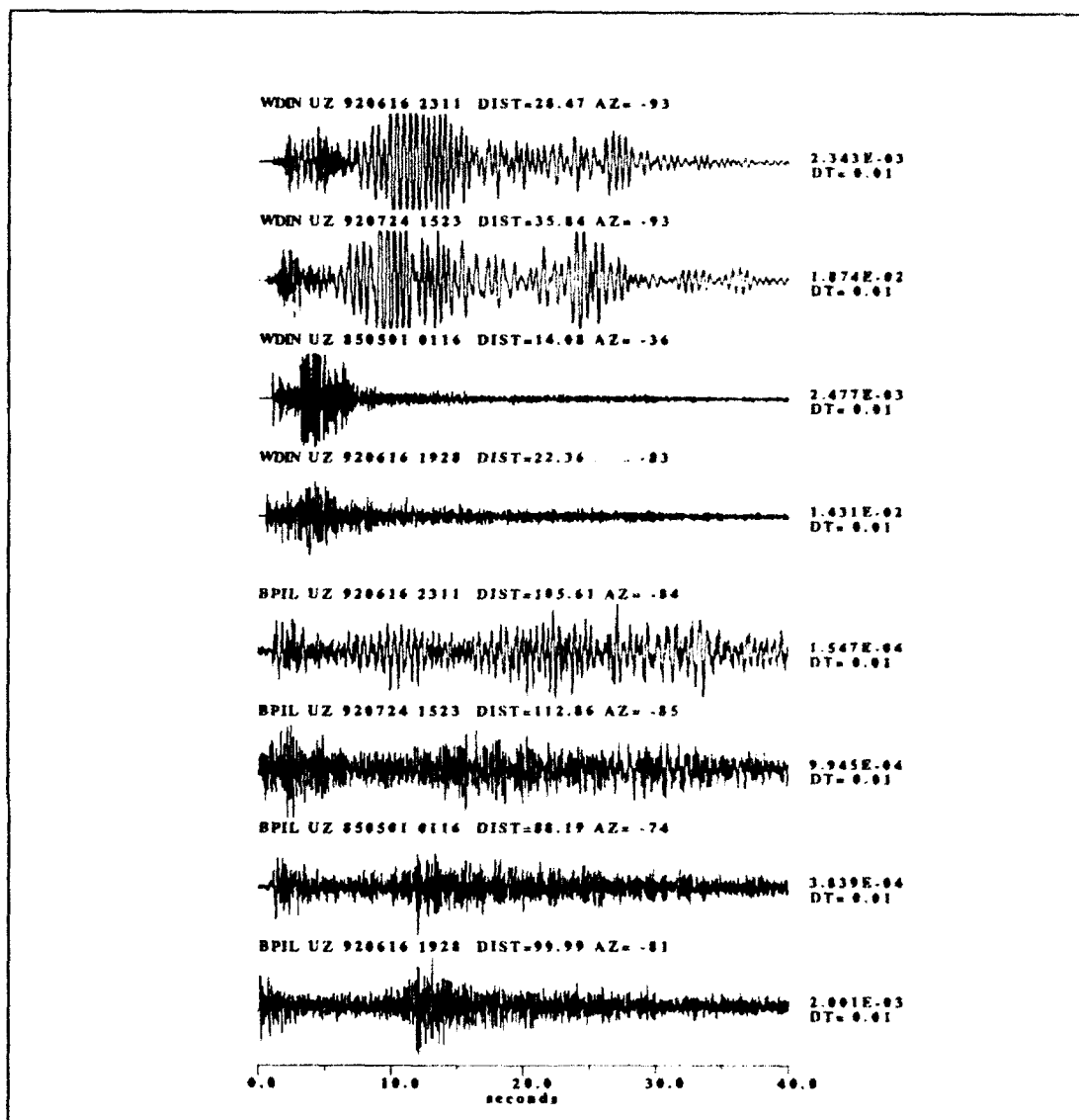


Fig. 3. A sequence of four time histories recorded at BPIL and WDIN. For each station, the upper two traces correspond to two different blast, and the lower two traces to two different earthquake recordings. The June 16, 1992 earthquake and blast time histories are included. Annotation shows distance (DIST), azimuth (AZ), maximum ground motion (in cm/sec) and sample rate (DT). The low frequency Rg coda is very pronounced in the blasts at WDIN. The Rg coda is not as pronounced at BPIL for the two blasts, but the S phase arrivals on the two earthquakes are more distinct.

Earthquakes generally occur at greater depths than blasts. As such, earthquakes do not usually have the characteristic low-frequency Rg coda associated with shallow-source events. Reported shallow-source earthquakes are discussed later in this section. The frequency content of earthquakes is higher, with P-, S-, and sometimes Lg, as the only identifiable phases. Finally, the earthquake codas decay much more rapidly.

The signals of the earthquake and strip-mine blast of 16 June 1992 were first examined using multiple filter analysis to permit something like a sonogram display (Dziewonski *et al.*, 1969). Herrmann (1973, 1987) modified the technique to estimate spectral amplitudes of various modes. This moving window analysis is normally used for obtaining surface-wave dispersion but also indicates apparent velocities of body waves. The displacement in the time domain caused by a dispersed, propagating, multimode wave at a distance r can be represented by

$$f(t, r) = \frac{1}{2\pi} \int_{-\infty}^{\infty} F(\omega, r) e^{i\omega t} d\omega \quad (1)$$

or

$$f(t, r) = \frac{1}{2\pi} \int_{-\infty}^{\infty} \sum_{j=0}^M A_j(\omega, r) e^{i(\omega t - k_j r)} d\omega \quad (2)$$

where t is time, ω is angular frequency, k_j is the wave number of the j 'th mode, A_j is the complex amplitude of the j 'th mode, and M is the highest mode in the signal (a total of $M + 1$ modes). The signal is then filtered with a symmetric Gaussian band-pass signal $H(\omega)$ of the form

$$H(\omega) = \begin{cases} \exp(-\alpha (\omega - \omega_0)^2 / \omega_0^2) & |\omega - \omega_0| \leq \omega_c \\ 0 & |\omega - \omega_0| > \omega_c \end{cases} \quad (3)$$

where α is a filter parameter, ω_0 is the filter center frequency, and $\omega = \omega_0 \pm \omega_c$ is the cutoff frequency for the filter. The resultant time filtered signal representing a multi-mode signal is of the form

$$g(t, r) = \frac{\omega_0}{2\pi} \left(\frac{\pi}{\alpha} \right)^{1/2} \sum_{j=0}^M A_j(\omega_0, r) \cdot \quad (4)$$

$$\exp[i(\omega_0 t - k_{0j} r)] \exp \left[-\frac{\omega_0^2}{4\alpha} \left(t - \frac{r}{U_{0j}} \right)^2 \right]$$

where U_{0j} is the group velocity of the j 'th mode at frequency $\omega = \omega_0$.

The envelope of the signal is formed using the Hilbert transform. The group velocity of a particular phase is determined from the time of the peak envelope amplitude. To define or separate various phases or modes, a minimum separation of $2t_d$ is required, where

$$t_d = \left(\frac{4\pi\alpha}{\omega_o} \right)^{1/2} = T_o \left(\frac{\alpha}{\pi} \right)^{1/2} \quad (5)$$

T_o is the period corresponding to frequency ω_o . For separations less than $2t_d$, the observed envelope maxima will not be the true mode maxima, but a complex sum of the modal amplitudes (Herrmann, 1973).

The envelope maxima for both the earthquake and strip-mine blast recorded at WDIN on 16 June, 1992, are shown in Figures 4a and 4b. In this display, the contours of constant amplitude are shown. The small square, circle and triangle and plus symbols indicate the largest through the fourth largest spectral peaks, respectively, at a given filter period. The apparent P-phase velocity of the earthquake is shown with a velocity between 6.0 to 6.3 km/sec, while that of the blast is slightly slower, a high frequency arrival near 6.3 km/sec, similar to the earthquake, but with strong secondary arrivals between 5.6 to 6.0 km/sec. At this short distance, this may reflect a slightly different ray path from the source to station because of the shallowness of the blast and because of the very thick sedimentary rock section in the region (> 3 km).

The Lg/S-phase arrival times for each event are similar, both traveling near 3.5 to 3.75 km/sec. However, note the large difference in frequency content in the signal. The Lg-phase arrival of the earthquake is not obvious below 15 Hz while the strip-mine blast shows several maxima between 3 to 15 Hz with little signal content above 15 Hz.

Two body wave arrivals are shown on both the earthquake and strip-mine blast with velocities near 4.6 and 5.0 km/sec. These arrivals are also observable in the time series waveform. Both arrivals exhibit similar velocities, regardless of source location. The arrivals may be reflections or refractions from several of the known groups in the vicinity, for example, the Chattanooga shale or Eau Claire formation (Sexton *et al.*, 1986).

The fundamental mode Rg-phase and at least one, strong higher mode are visible for the blast. The fundamental mode is visible (extreme lower left-hand corner of the contour plot) with a group velocity between 1.0 to 2.0 km/sec and frequency between 0.5 and 2.0 Hz. The higher mode is visible (the next maxima towards the upper right of the figure) with a group velocity between 1.5 to 2.9 km/sec and frequency of 1.0 to 3.2 Hz.

Other contours represent incoherent energy due to either noise or scattering. As a particular feature of the contouring, the incoherent energy may

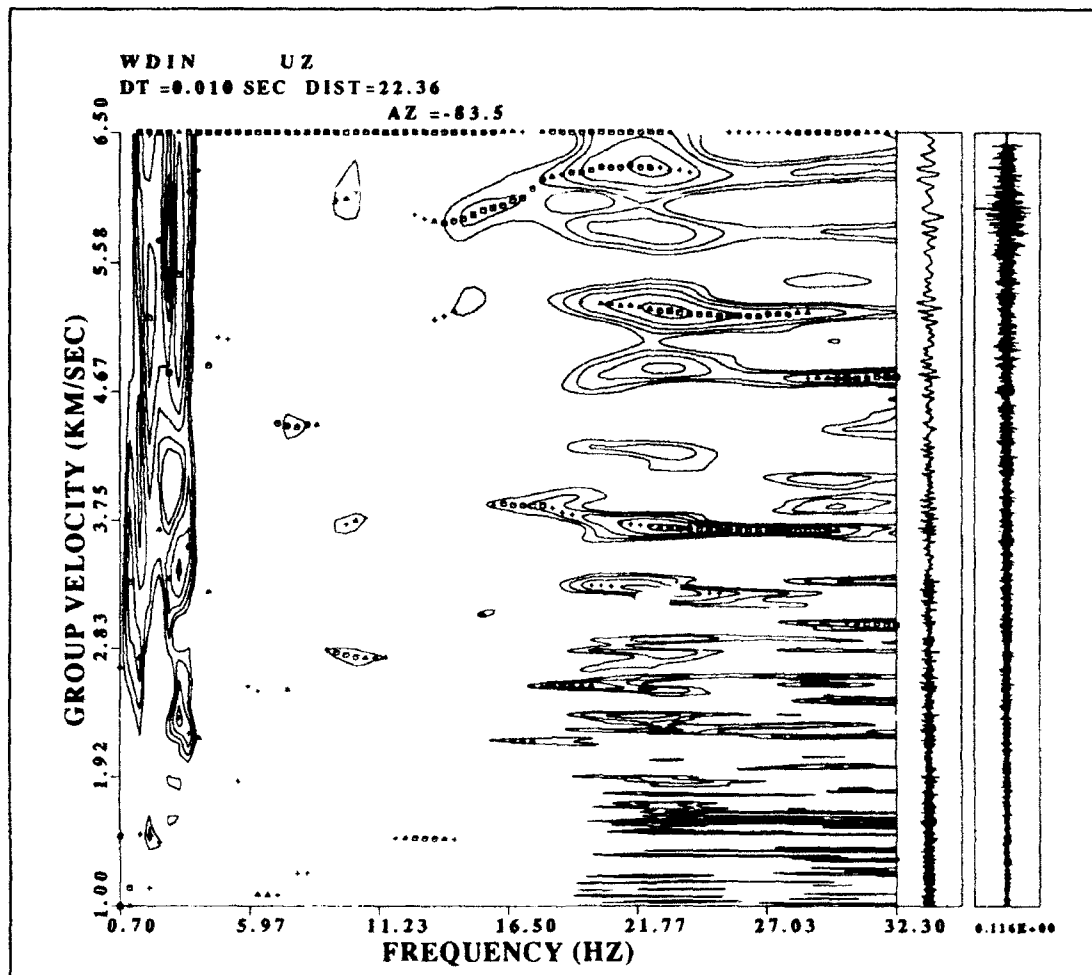


Fig. 4a. Envelope maxima as a function of frequency for the earthquake of 16 June 1992 at WDIN. The 40.96 seconds of recorded signal are shown on the far right in linear time. To its left is the same signal plotted as a function of group velocity to assist in relating the observed signal arrivals to specific group velocities.

be at a higher level than any coherent energy. For example, note the low frequency (0.70 to 3.0 Hz) band on the earthquake (Figure 4a). It is not coherent but is low frequency information with an apparent group velocity greater than 2.0 km/sec. Likewise, the points along the top margin at all frequencies represent noise energy with apparent group velocities greater than 6.5 km/sec. The apparent absence of information in the 3 to 12 Hz band is a direct result of the incoherent energy mapped along the top of the figure. In this same band for the explosion (Figure 4b), the coherent information is at a

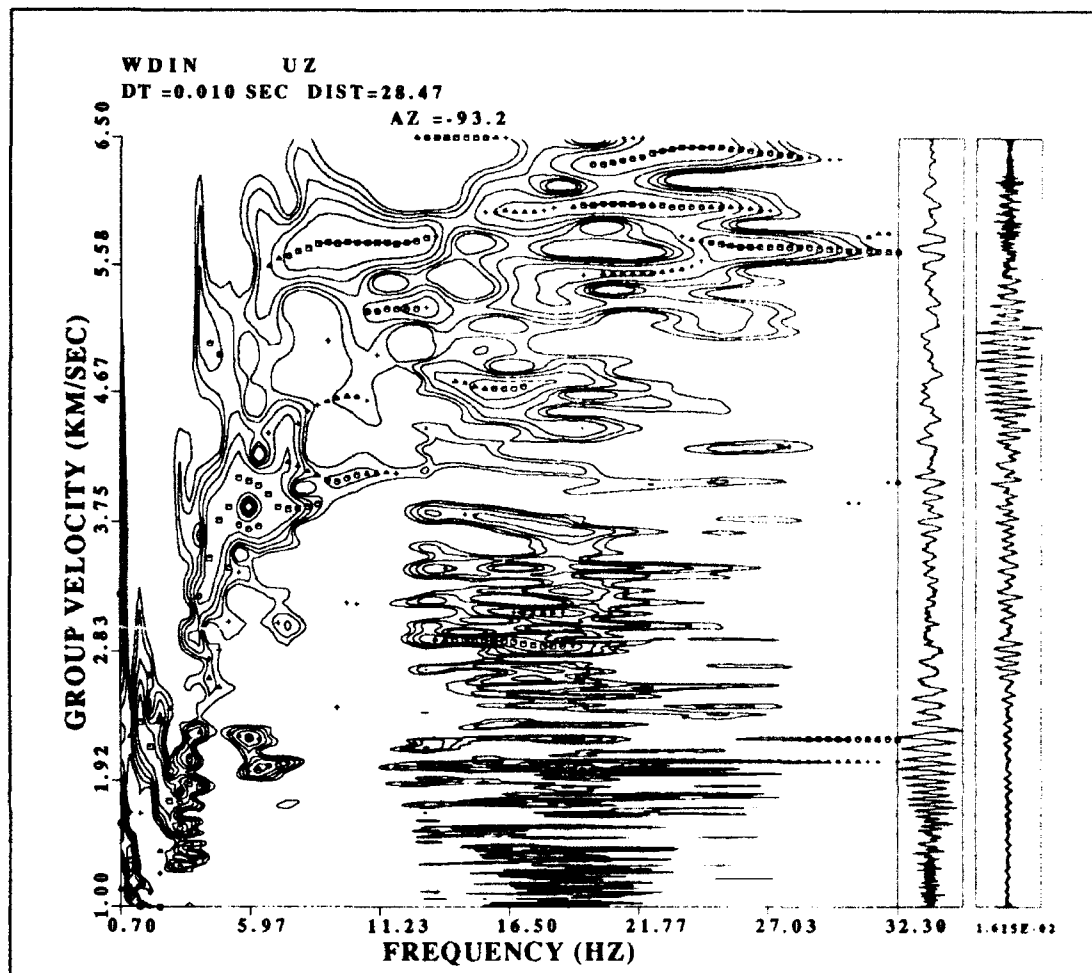


Fig. 4b. Envelope maxima as a function of frequency for the strip-mine blast of 16 June 1992 at WDIN. A well-developed fundamental and at least one higher mode are visible in the lower left corner of the group velocity contours, between 1.0 to 2.9 km/sec and 0.5 to 3.2 Hz.

higher level than the incoherent noise. Information observable from the contours is also directly observable in individual spectra.

The spectral content of the P, Lg, and Rg phases were examined in additional detail at both WDIN and BPIL. Each spectra contains 512 data samples, obtained from a velocity window using the limits defined by the group velocity maxima of each phase (Dziewonski *et al.*, 1969; Herrmann, 1973). The P-phase spectra were windowed between 5.0 and 6.5 km/sec at both stations. The Lg phase spectra were windowed between 2.5 to 4.0 km/sec at WDIN and 3.0 to 4.0 km/sec at BPIL. Finally, the Rg phase spectra were

windowed between 0.5 to 2.5 km/sec, the window nearly overlapping with those of the Lg phase at WDIN.

The windowed time series were detrended, then tapered with a 10% cosine taper applied to each end of the window to help remove high frequencies associated with edge effects. A Fast Fourier Transform technique (Herrmann, 1987) was used to calculate each of the displacement spectra. Finally, the spectra were corrected to ground motion at the observed distance by removing instrument effects. No distance correction is applied since source estimates are not made. Spectra for each phase, event, and station are shown on the same scale in Figures 5 through 8.

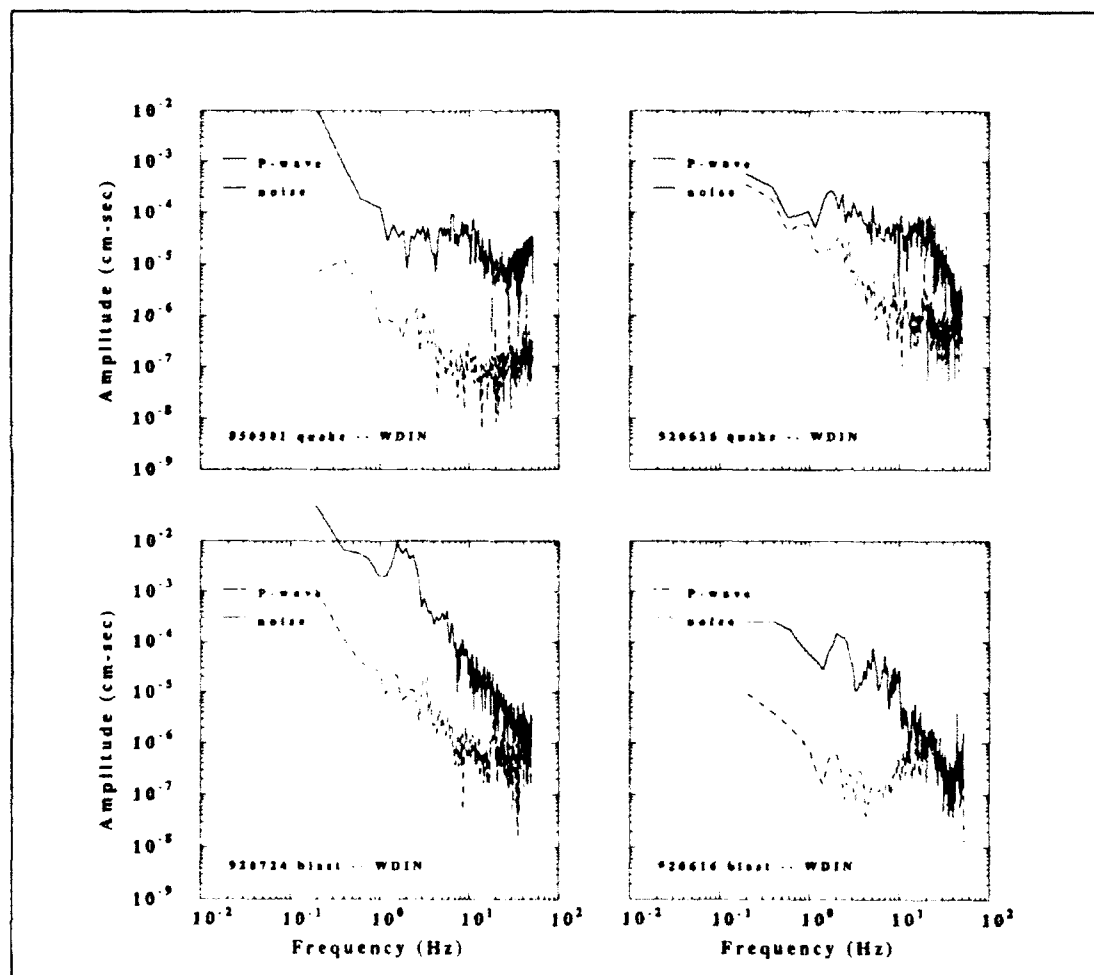


Fig. 5. P-phase spectra, WDIN for the traces shown in Figure 3.

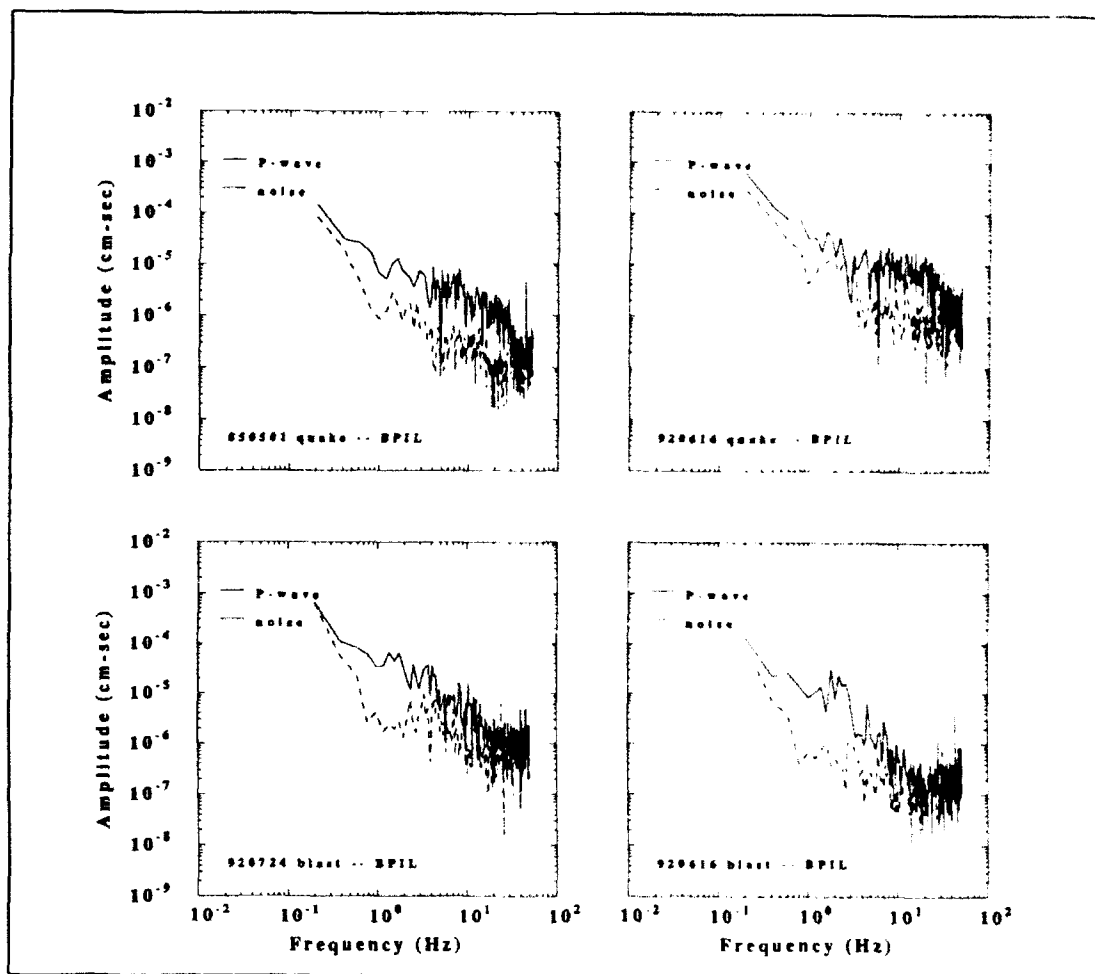


Fig. 6. P-phase spectra, BPIL for the traces shown in Figure 3.

The spectra for each phase and station confirm the frequency content observed in the seismograms (Figures 2 and 3). These earthquakes generally have P-phase corner frequencies near 10 Hz, with significant energy up to 20-30 Hz. Strip-mine blasts, however, have much lower P-phase corner frequencies, closer to 4-6 Hz, and high frequency energy is usually not obvious above 10 Hz.

A comparison of the recordings of the same event at the different stations shows similarity in spectra, with the exception of the 920724 blast because of the low S/N ratio at BPIL. In addition, at a given station, the spectra of the two blasts and of the two earthquakes are also very similar. Thus the site effects at the stations are either not affecting the spectral shapes or are affecting them in the same manner. The blast spectra at BPIL and WDIN

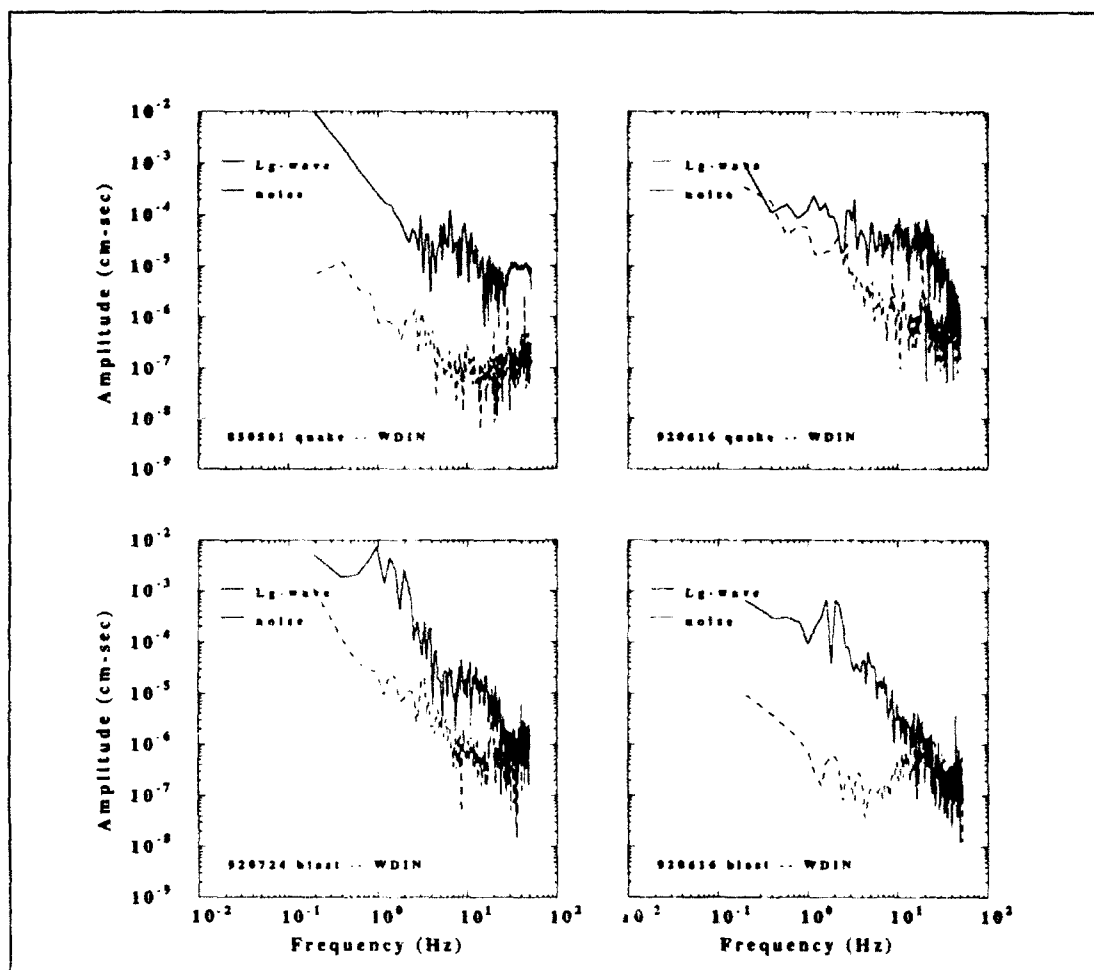


Fig. 7. Lg-phase spectra, WDIN for the traces shown in Figure 3.

show a pronounced, isolated spectral peak between 1.5 and 3.5 Hz. Since this is not as apparent in the noise or earthquake spectra, this must be a feature of the strip-mine explosion. In fact, the modulation of the WDIN recordings of the 920616 blast between 1 and 8 Hz is characteristic of that due to ripple firing (Baumgardt and Ziegler, 1988).

The significant conclusion, then, from examining the P-wave spectra is that the earthquakes are richer in higher frequencies than the strip-mine blasts with higher corner frequencies. This is opposite of the results one would expect from theoretical spectral estimates between earthquakes and nuclear explosions (Evernden *et al.*, 1986). Studies for nuclear explosions and earthquakes in the western United States suggest similar findings (Murphy and Bennett, 1982; Bennett and Murphy, 1986, Taylor *et al.*, 1989; Chael,

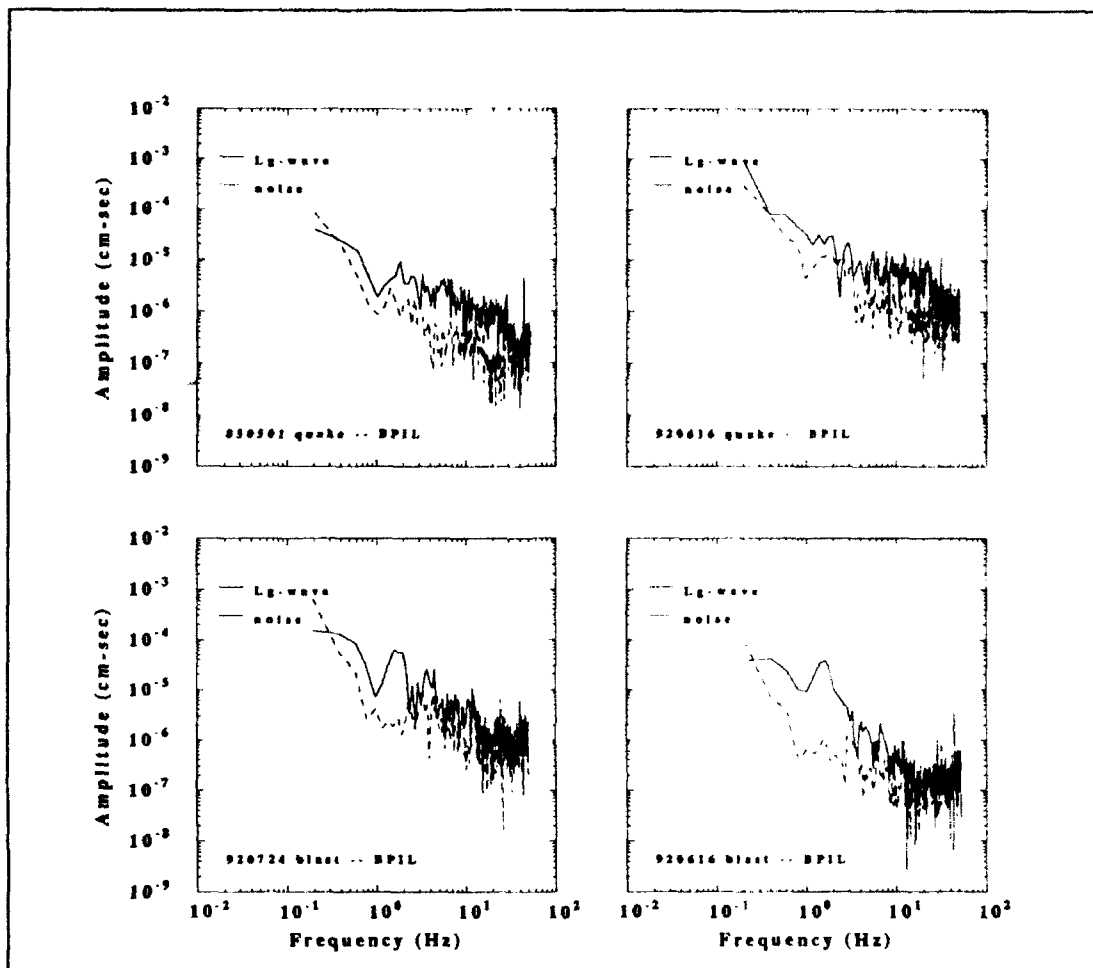


Fig. 8. Lg-phase spectra, BPIL for the traces shown in Figure 3.

1988, 1991).

Results for the Lg phase are similar. The Lg spectra for the blasts show significantly higher low frequency energy (0.8 to 5 Hz) while the earthquake spectra are richer in energy at higher frequencies (> 8 Hz). This is similar to the trends observed in the P-wave spectra. A spectral peak is seen in some of the blast spectra in the 1 - 3 Hz range, but the spectral modulation is not readily apparent. Another interesting feature is that the Lg- and P-wave spectral levels are about the same for the same station-event tuple.

The Rg and Lg spectral results are similar in terms of frequency content. However, note that at station BPIL, the farthest from the source, the spectral level is almost indistinguishable from the background noise for the

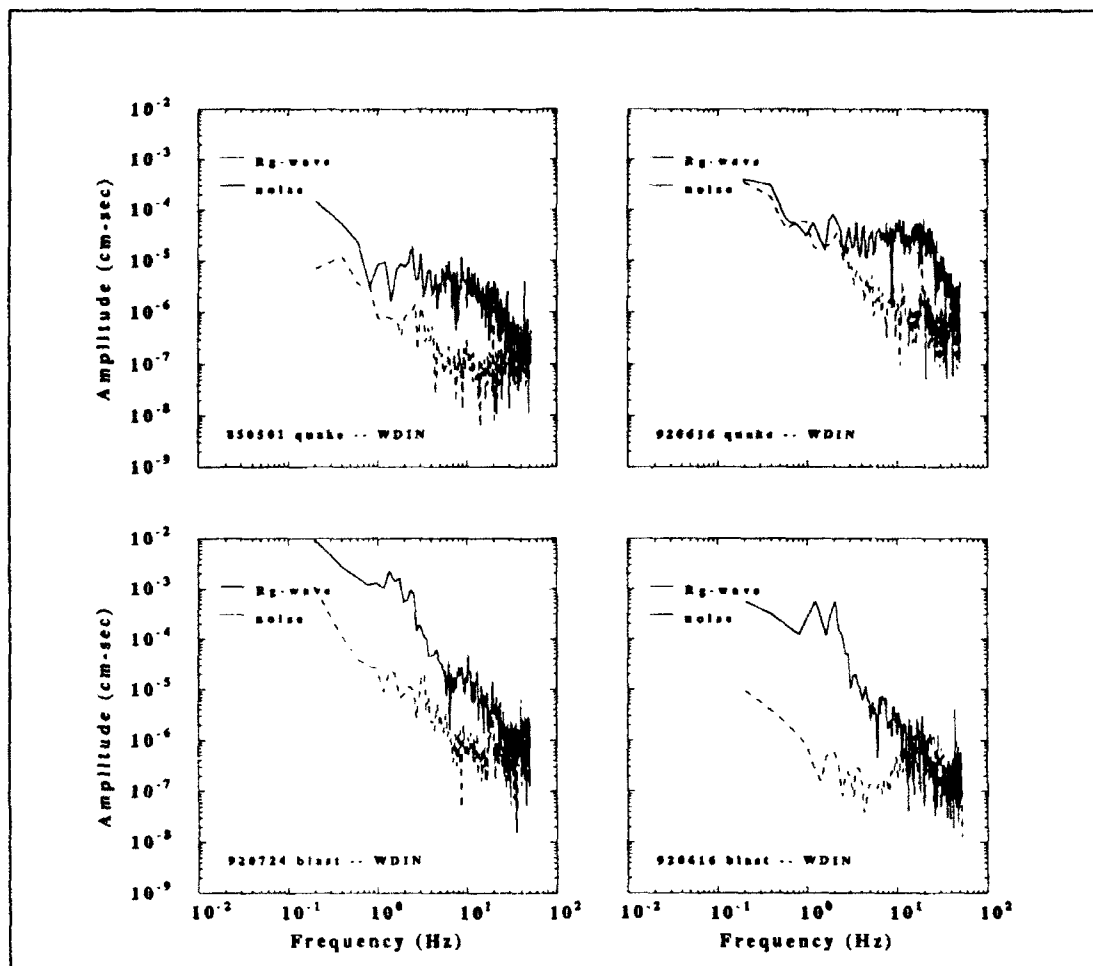


Fig. 9. Rg-phase spectra, WDIN for the traces shown in Figure 3.

earthquake; only the strip-mine blast spectra shows energy in the 0.4 to 2 Hz band.

No focal mechanisms have been obtained for earthquakes in this area due to the size of the events and the CMVSN station distribution. It is assumed in this study that the earthquakes all have similar mechanisms, with fault planes trending NNE or NNW. This assumption is based on the general NNE trend of mapped faults and basement structures in the immediate area (Pratt *et al.*, 1989; Sexton *et al.*, 1986; Nelson and Lumm, 1984), or from extending the La Salle Anticlinal Belt through the basement in this area (Hamburger and Rupp, 1988). Most workers agree that current seismicity is the result of reactivated N-S trending basement faults, dissimilar to the E-W structures of the Cottage Grove-Rough Creek Fault Systems (Nelson

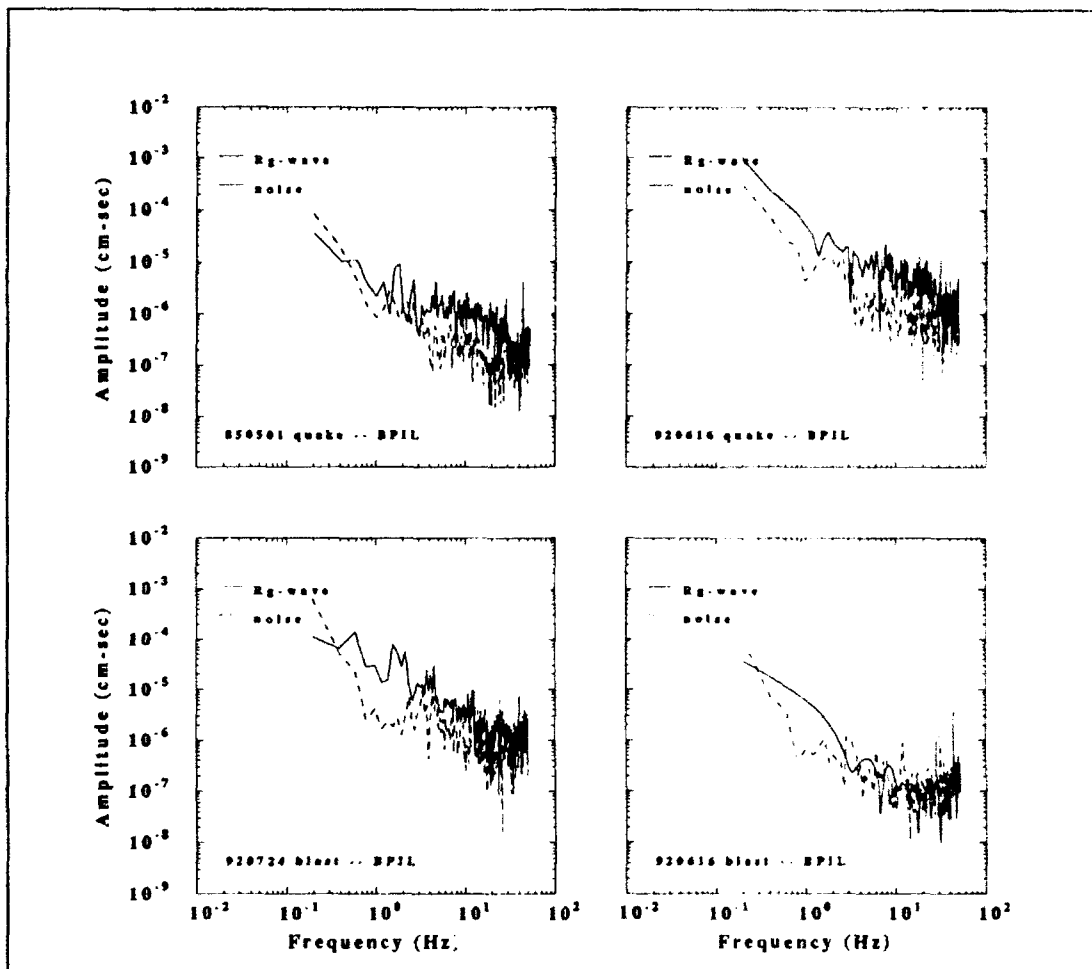


Fig. 10. Rg-phase spectra, BPIL for the traces shown in Figure 3.

and Lumm, 1984). The few focal mechanisms for the nearest earthquakes in Illinois (Herrmann, 1979b; Taylor *et al.*, 1989) may be associated with the La Salle Anticlinal Belt (Hamburger and Rupp, 1988). Thus, the relative event levels at a given station should reflect effects of the source-time function, not radiation patterns. If true, then the earthquake spectra can be directly compared.

This may not be the case for the strip-mine blasts. Many of the strip mine shots are patterned averaging three rows, two decks, and approximately a hundred holes per shot. Azimuthal effects may be important, but they cannot be resolved with this data set.

A remaining question of importance is whether shallow earthquakes in the region exhibit similar Rg codas. One hundred one (101) events were found in the CMVSN event catalog with depths less than 4.0 km between 37° to 40° N latitude and 86.5° to 92.5° W longitude. Many of these are within the Illinois Basin (Figure 11). Well-located earthquakes in the basin generally locate at average depths of approximately 10.0 to 11.0 km. The catalog shows a strong correlation of depths at 2.5, 5.0, and 10.0 km, the default location depths. No shallow-depth earthquakes have been reported by the CMVSN in Indiana; however, it is recognized that depth is poorly constrained outside the coverage area of the CMVSN stations. All events used in this study were relocated, with particular emphasis on depth.

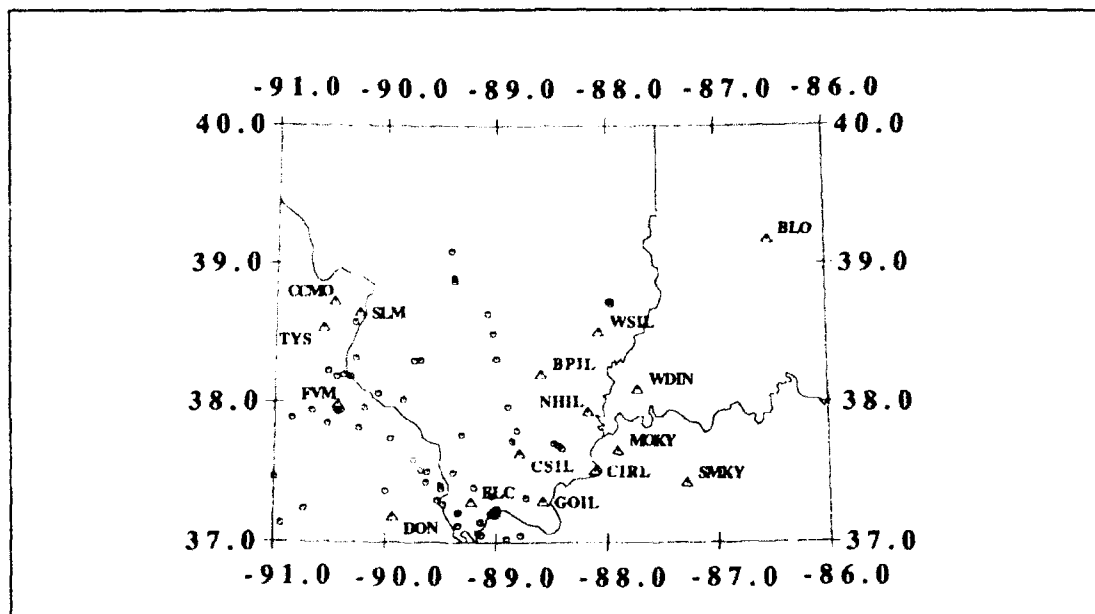


Fig. 11. Shallow earthquakes reported in the the Illinois Basin and eastern Missouri in relation the CMVSN stations.

Waveforms for several reported "shallow-depth" events (Table 3) are shown in Figures 12 through 14 at various CMVSN stations. Although nominally shallow (< 4.0 km), none have the low-frequency Rg coda typical of shallow events. The implication is that either the sources were deeper than the layered sedimentary rock waveguide, or, more likely, the published bulletin depths are in error due to poor depth control.

Shallow earthquakes do occur within or on the boundaries of the Illinois Basin. An earthquake that occurred on 14 August 1965 in southern Illinois produced a short period dispersed surface wave on a World Wide

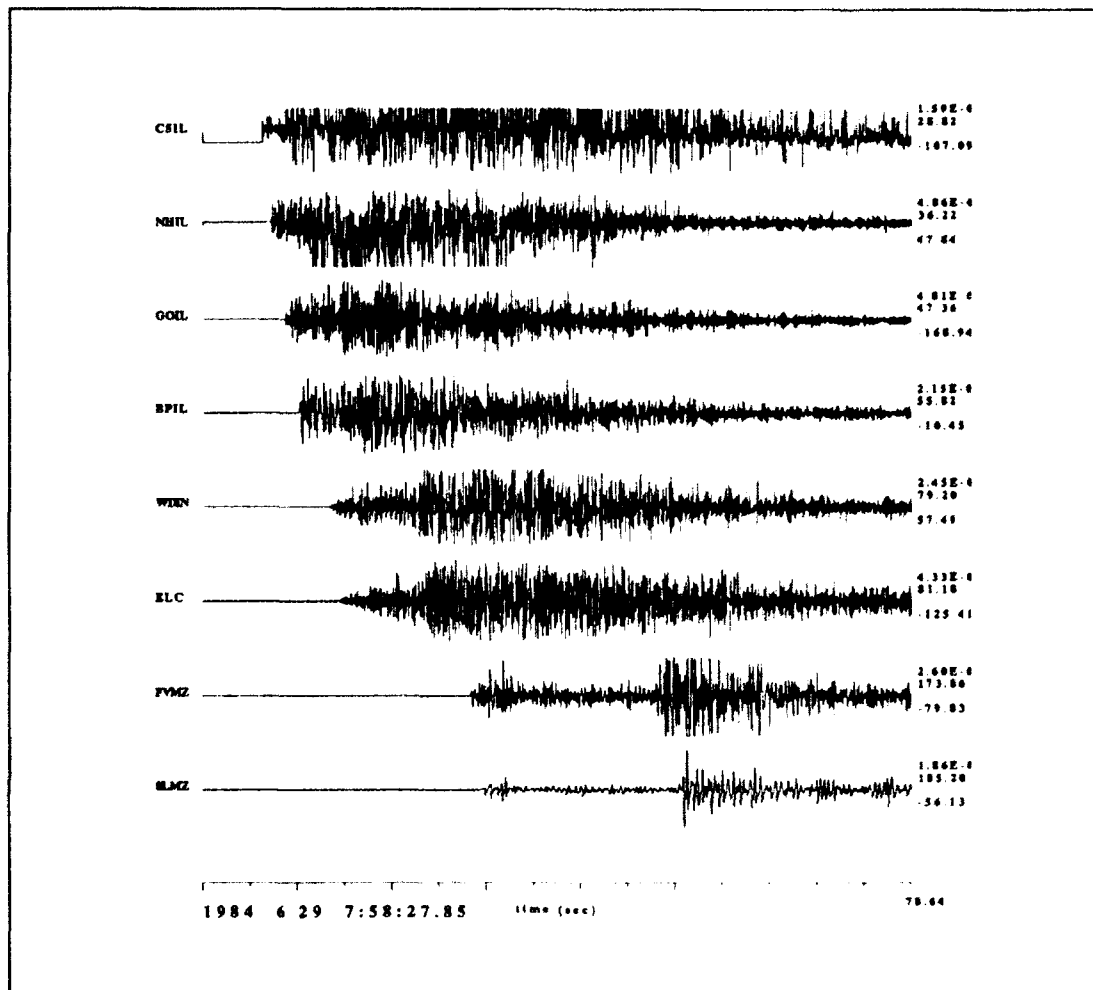


Fig. 12. Time series of the earthquake of 29 June 1984 in southeastern Illinois at various CMVSN stations. The traces are annotated with station name, peak velocity in cm/sec, epicentral distance, and azimuth ($^{\circ}$ s relative to north). Note that the waveforms at stations FVMZ and SLMZ have a noticeably different character. Both have a narrower instrument response with a lower passband. As a result, the high frequency information seen in the other CMVSN stations is not observed. However, short period Rg waves are not seen either.

Standard Seismic Network (WWSSN) long-period (LP) instrument (FLO in St. Louis) for a path length of 200 km (Herrmann, 1974; Herrmann and Nuttli, 1975). This observation was possible only because the LP instrument filtered out the high-frequency Lg signal. This m_b 3.8 event was assigned a depth of 1.0 km based on surface-wave modeling (Herrmann, 1974). No broader bandwidth recordings of this event exist since the CMVSN was not installed until 1974 (Stauder *et al.*, 1991).

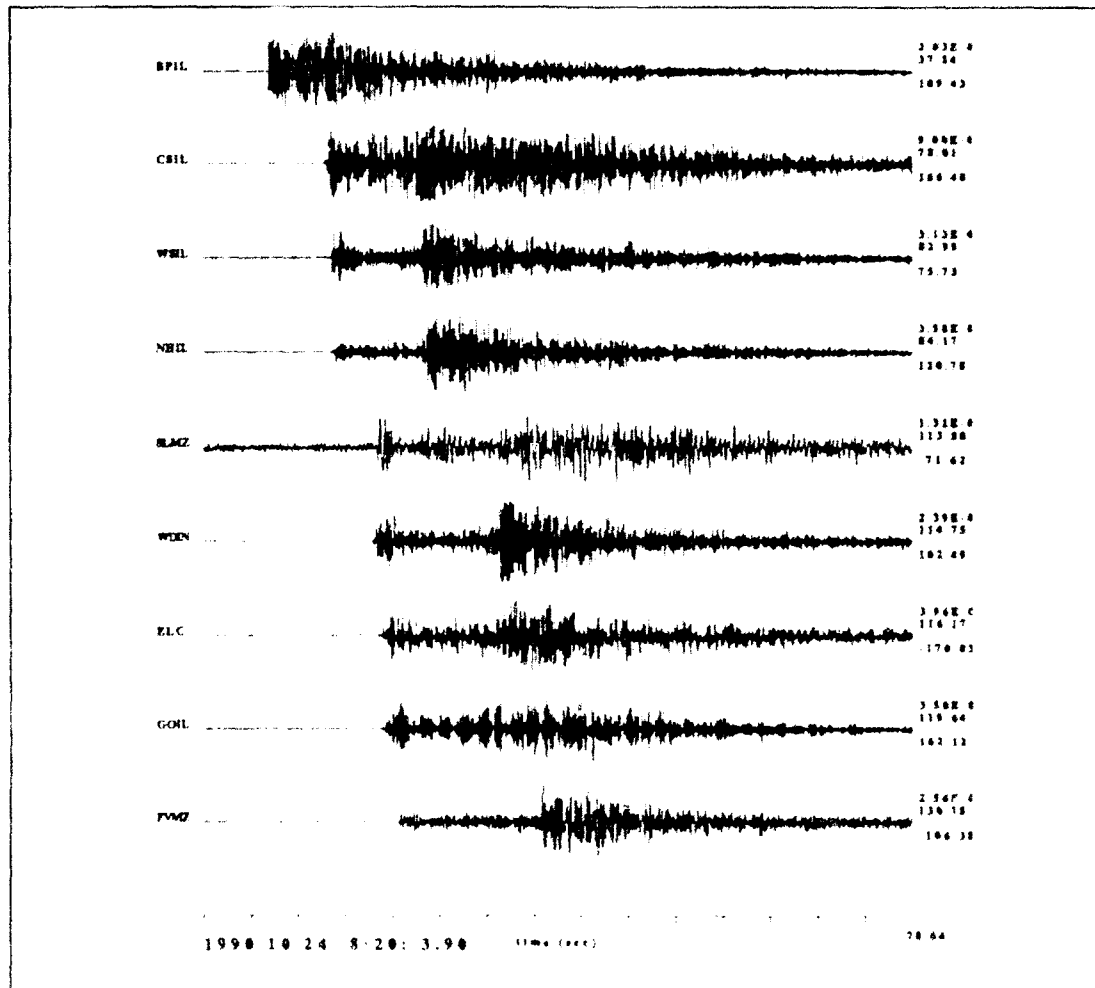


Fig. 13. Time series of the earthquake of 24 October 1990 in central Illinois at various CMVSN stations.

DISCUSSION AND CONCLUSIONS

The occurrence of earthquakes in the same region as active strip mines allows a direct comparison of the appearance and spectral content of each event type. Arguments that differences in signal character of body waves are due to path propagation effects are weakened when both types of events are located in the same vicinity, assuming that the depth effect is small, and when the same stations record both types of events. Events similarly located also reduce the variability found in phase onsets, phase appearance, and particular phases found from various sites (Gupta and Hartenberger, 1981). Results in this study are similar in these respects to similar studies using

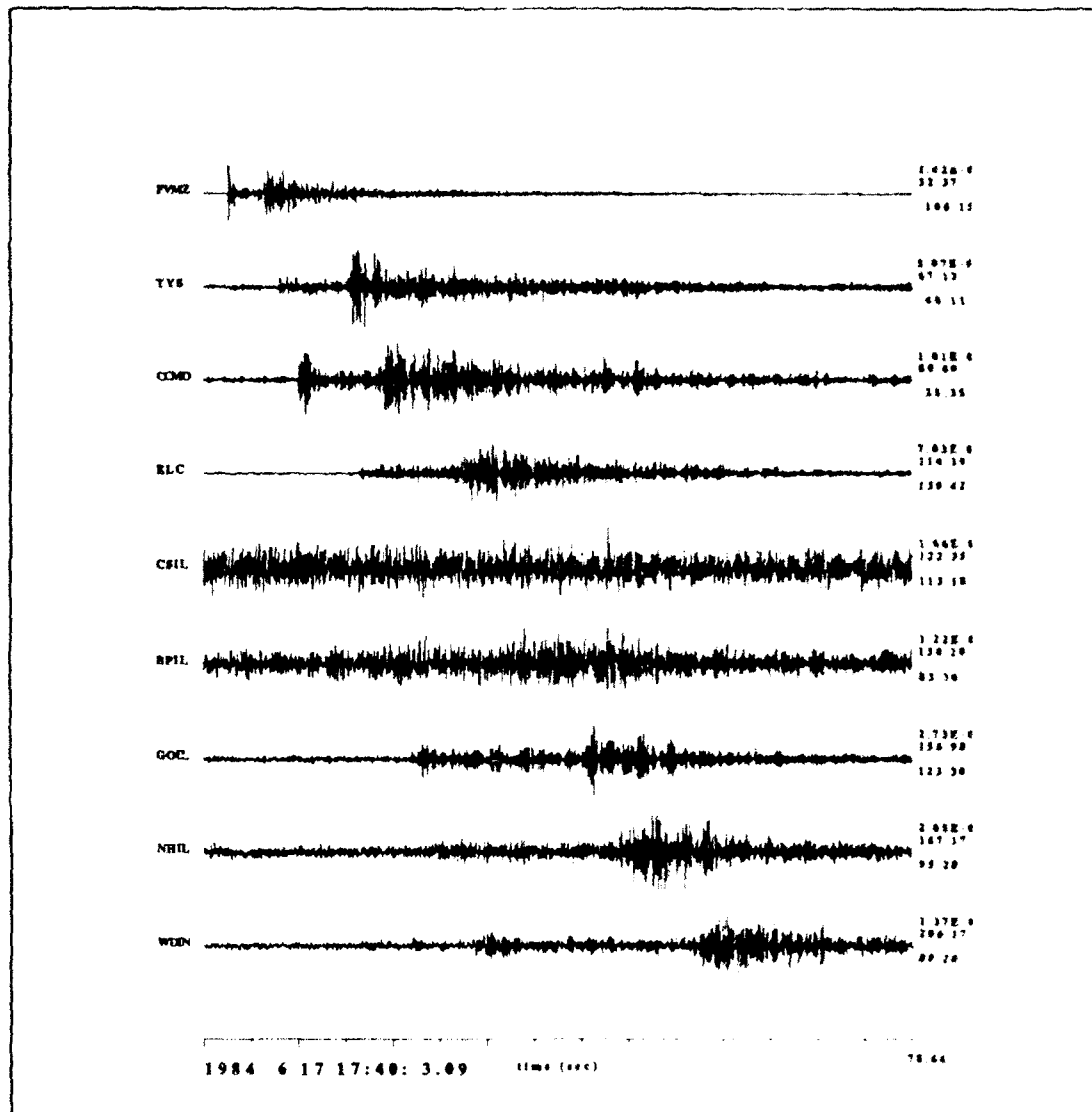


Fig. 14. Time series of the earthquake of 17 June 1984 in western Illinois at various CMVSN stations.

nuclear explosion and earthquakes (*i.e.* Chael, 1988, 1991).

On analog or digital recordings (Figures 2 and 3), the appearance of the strip-mine blast and earthquake signals allow for visual discrimination between the two. Signals from strip-mine blasts have a distinctive Rg phase, most with a large-amplitude Airy phase, indicative of shallow-source events (Båth, 1975; Shapiro, 1988; Kafka, 1990). Earthquakes, even presumably shallow earthquakes in the Illinois Basin, lack the well-developed Rg phase

and have rapidly decaying codas. The lack of a well-developed Rg phase in reported shallow earthquakes quite probably indicates poor depth control in the earthquake catalog; these events, reported at a shallow depth, are thus inferred to occur much deeper. At least one demonstrably shallow earthquake prior to the installation of the CMVSN has produced surface waves (Herrmann, 1974; Herrmann and Nuttli, 1975), indicating most earthquakes are deeper. Finally, the onset of the P, S, and sometimes Lg, phases are more impulsive for earthquakes than for the strip-mine blasts.

Aside from visual discrimination, the spectral content also shows differences. The corner frequencies of the P-wave spectra are lower for the blast than for the earthquakes. In addition, the energy content in the high-frequency passband (10-30 Hz) is higher for earthquakes than for strip-mine blasts. This result is similar to prior studies of regional discriminants in the Western U.S. and Central Asia (Balapan) designed to distinguish between nuclear explosions and earthquakes (Bennett *et al.*, 1992). These studies have shown both Pg and Lg spectra richer in higher frequency energy, especially between 3 to 6 Hz (Murphy and Bennett, 1982; Bennett and Murphy, 1986; Bennett *et al.*, 1992), in comparisons of spectral ratio in the 1 to 2 Hz and 6 to 8 Hz passbands (Taylor *et al.*, 1989), and at frequencies between 10 to 30 Hz (Chael, 1988, 1991).

Results for Lop Nor, the Chinese test site, indicate the opposite (Bennett *et al.*, 1992). Earthquakes exhibit greater low frequency energy while the nuclear explosions were enhanced at the higher frequencies. In addition, the raw waveforms showed a more prominent Rg phase (larger amplitude, but not larger than S or Lg) than the explosions at one of the stations.

Theoretical source models suggest that explosions should be richer in high frequency energy primarily due to the differences in corner frequency and spectral rolloff rates (Evernden *et al.*, 1986; Walter and Priestly, 1991). In this case, the earthquake has lower high frequency content than the explosion at fixed low frequency levels because of the larger source dimension (lower stress drop) of the earthquake relative to the point source nuclear explosion. Our study finds the opposite effect for the same reason. For a given high frequency level, used to assign the event magnitude, the earthquake appears as a point source while the strip-mine explosion appears as an extended source. This is not surprising, given the large spatial dimensions of the strip-mine shots as well as the time delays inherent to ripple-firing.

This observation may serve to distinguish point sources from distributed sources for small events. The implication in a proliferation environment is that one must look at attributes other than P- or Lg-wave spectral content to define the nuclear explosion (path attenuation, earthquake radiation patterns, etc.). The appearance of the Rg wave and signal complexity may provide an answer.

Finally, the occurrence of earthquakes in this region, and elsewhere within the Illinois Basin, are apparently the result of movement along existing Paleozoic basement structures (Hamburger and Rupp, 1988; Pratt *et al.*, 1989; Taylor, 1991). While a concern of the public, it cannot be reasonably argued that earthquakes in this region are a result of any current blasting or mining activity. Unlike other areas where a spatial association with mining exists (ie McGarr, 1984; Gibowicz, 1990), no temporal association between earthquakes and strip-mine blasts have been found in this area. The spatial association is due to the location of Paleozoic basement structures beneath easily obtainable surface coal resources.

While seismicity has been associated with active mining operations (McGarr, 1984; Gibowicz, 1990), it is rare with surface mining (Gibowicz, 1990). Events have occurred as a result of coal mining operations in Poland. However, the induced events in that area appear to be triggered by two actions, a decrease in the vertical stress, caused by the removal of the overburden (nearly 300 meters) and an increase in the effective stress, due to decreasing pore pressure as a result of groundwater withdrawal (Gibowicz, 1990). Obtainable coal resources (strip-mines, not underground mines) occurs at shallower depths in Illinois and Indiana, about a third less overburden is removed.

ACKNOWLEDGMENTS

Special thanks go to Ms. Melanie Whittington for her help in obtaining and archiving seismic data. Thanks also to both M. Hamburger and R. Street for providing phase and waveform data for several of the events discussed in the text. Improvements in the manuscript are the result of comments by M. Hamburger, T.J. Bennett, and an anonymous reviewer. This research has been sponsored by the Air Force Phillips Laboratory under Contract No. F19628-90-K-0040.

REFERENCES

- Amjad, M. (1991). Discrimination between earthquakes and explosions in the central United States, *Ph.D Dissert.*, St. Louis University, St. Louis, MO.
- Ault, C.H. and D.M. Sullivan (1982). Faulting in southwest Indiana, *U.S. Nuclear Reg. Comm. Report*, NUREG/CR-2908, 50 pp.
- Ault, C.H., D. Harper, C.R. Smith, and M.A. Wright, 1985, Faulting and jointing in near surface mines of southwest Indiana, *U.S. Nuclear Reg. Comm. Report*, NUREG/CR-4117, 27 pp.

- Barstow, N.L., K.G. Brill, Jr., O.W. Nuttli, and P.W. Pomeroy (1981). An approach to seismic zonation for siting nuclear electric power generating facilities in the eastern United States, *U.S. Nuclear Reg. Comm. Report*, NUREG/CR-1577.
- Båth, M. (1975). Short period Rayleigh waves from near surface events, *Phys. Earth Planet. Inter.*, **10**, 369-376.
- Baumgardt, D.R. and K.A. Zeiglar (1988). Spectral evidence for source multiplicity in explosions: application to regional discrimination of earthquakes and explosions, *Bull. Seism. Soc. Am.*, **78**, 1773-1795.
- Bennett, T.J. and J.R. Murphy (1986). Analysis of seismic discrimination capabilities using regional data from western U.S. earthquakes, *Bull. Seism. Soc. Am.*, **76**, 1069-1986.
- Bennett, T.J., A.K. Campanella, J.F. Scheimer, and J.R. Murphy (1989). Demonstration of regional discrimination of Eurasian seismic events using observation at Soviet IRIS and CDSN stations, *Phillips Laboratory Report (Final)*, PL-TR-92-2090. ADA253275
- Bristol, H.B. and T.C. Buschbach (1971). Structural features of the Eastern Interior Region of the United States, in Bond, D.C., chairman, *Background materials for symposium on future petroleum potential of NPC Region 9 (Illinois Basin, Cincinnati Arch, and northern part of the Mississippi Embayment)*, Illinois State Geological Survey Illinois Petroleum 96, 63 p.
- Bristol, H.M. and J.D. Treworgy (1979). The Wabash Valley fault system in southeastern Illinois, *Circular 509*, Illinois State Geological Survey, Champaign, IL, 19 pp.
- Chael, E.P. (1988). Spectral discrimination of NTS explosions and earthquakes in the southwestern United States using high-frequency regional data, *Geophy. Res. Letters*, **15**, 625-628.
- Chael, E.P. (1991). Effects of explosion source parameters on high-frequency Pg spectra, in, Taylor, S.R., H.J. Patton, and P.G. Richards, *Explosion Source Phenomenology*, Geophysical Monograph 65, Am. Geophys. Union, 211-217.
- Collinson, C., M.L. Sargent, and J.R. Jennings (1988). Illinois Basin region, in, Sloss, L.L., ed., *Sedimentary Cover -- North American Craton, U.S.:*

Geological Society of America, The Geology of North America, v. D-2, Boulder, CO, 383-426.

- Dziewonski, A.M., S. Bloch, and M. Landisman (1969). A technique for the analysis of transient seismic signals, *Bull. Seism. Soc. Am.*, **59**, 427-444.
- Evernden, J.F., C.B. Archambeau, and E. Cramswick (1986). An evaluation of seismic decoupling and underground nuclear test monitoring using high-frequency seismic data, *Rev. Geophys.*, **24**, 143-215.
- Gibowicz, S.J. (1990). Seismicity induced by mining, in Dmowska, R. and B. Saltzman, eds., *Advances in Geophysics*, **32**, 1-74.
- Gupta, I.N. and R.A. Hartenberger (1981). Seismic phases and scaling associated with small high-explosion surface shots, *Bull. Seism. Soc. Am.*, **71**, 1731-1741.
- Hamburger, M.W. and J.A. Rupp, (1988). The June 1987 Southeaster Illinois earthquake: possible tectonism associated with the La Salle Anticlinal Belt, *Seism. Res. Letters*, **59**, 151-157.
- Harper, D. (1985). The development of surface coal mining in Indiana, *Geological Survey Special Report 35*, Department of Natural Resources, 54 pp.
- Hasenmueller, W.A. and J.E. Wiegand (1980). Map of Southwestern Indiana showing locations of active coal mines, *Geological Survey Special Report*, Department of Natural Resources, (revised by W.A. Hasenmueller, 1985).
- Hasenmueller, W.A. and D.D. Carr (1983). Indiana, in Nielson, G.F., editor, *Keystone coal industry manual*: New York, McGraw-Hill, Inc., 1461 pp.
- Herrmann, R.B. (1973). Some aspects of band-pass filtering of surface waves, *Bull. Seism. Soc. Am.*, **63**, 663-671.
- Herrmann, R.B. (1974). Surface wave generation by central United States earthquakes, *Ph.D Dissert.*, St. Louis University, St. Louis, MO.
- Herrmann, R.B. (1979a). FASTHYPO - A hypocenter location program, *Earthquake Notes*, **50**, 25-38.

- Herrmann, R.B. (1979b). Surface wave focal mechanisms for eastern North American earthquakes with tectonic implications, *J. Geophys. Res.*, **84**, 3543-3552.
- Herrmann, R.B. (1987). *Computer Programs in Seismology*, St. Louis University, St. Louis, MO.
- Herrmann, R.B. and O.W. Nuttli (1975). Ground-motion modelling at regional distances for earthquakes in a continental interior, I. theory and observations, *Int. J. Earthq. Engrng and Struct. Dyn.*, **4**, 49-58.
- Hutchenson, K.D., S. Baqer, and R.B. Herrmann (1990). Structure of the Illinois Basin using quarry blasts (abs), *Seism. Res. Letters*, **61**, 151.
- Hutchenson, K.D. and R.B. Herrmann (1991). Illinois Basin structure from local quarry blasts (abs), *Trans. Am. Geophys. Un., EOS*, **72**, 268.
- Kafka, A. (1990). Rg waves as a depth discriminator for earthquakes and explosions: a case study in New England, *Bull. Seism. Soc. Am.*, **80**, 373-394.
- McGarr, A. (1984). Some applications of seismic source mechanism studies to assessing underground hazard, in Gay N.C. and E.H. Wainwright, eds., *Proc. 1st Int. Cong. Rockbursts and Seismicity in Mines*, Johannesburg: South African Inst Min. Met., pp. 199-208.
- Murphy, J.R. and T.J. Bennett (1982). A discriminant analysis of short-period regional seismic data recorded at Tonto Forest Observatory, *Bull. Seism. Soc. Am.*, **72**, 1351-1366.
- Nelson, W.J. and D.K. Lumm (1984). Structural geology of southeastern Illinois and vicinity, *U.S. Nuclear Reg. Comm. Report*, NUREG/CR-4333, 127 pp.
- Nelson, W.J. and R.A. Bauer (1987). Thrust faults in the southern Illinois basin -- results of contemporary stress?, *Geol. Soc. Am. Bull.*, **98**, 302-307.
- Nuttli, O.W. (1983). *Catalog of Central United States Earthquakes Since 1800 of $m_b > 3.0$* , St. Louis University, St. Louis, MO.
- Nuttli, O.W. and K.G. Brill, Jr. (1981). Earthquake source zones in the central United States determined from historical seismicity, in Barstow,

- N.L., K.G. Brill, Jr., O.W. Nuttli, and P.W. Pomeroy, An approach to seismic zonation for siting nuclear electric power generating facilities in the eastern United States, *U.S. Nuclear Reg. Comm. Report*, NUREG/CR-1577, 97-143.
- Pomeroy, P.W., W.J. Best, and T.V. McEvilly (1982). Test ban treaty verification with regional data--a review, *Bull. Seism. Soc. Am.*, **72**, S89-S129.
- Pratt, T., R. Culotta, E. Hauser, D. Nelson, L. Brown, S. Kaufman, J. Oliver, and W. Hinze (1989) Major proterozoic basement features of the eastern midcontinent of North America, revealed by recent COCORP profiling, *Geology*, **17**, 505-509.
- Stauder, W., R. Herrmann, M. Whittington, M. Wuenschel, and K. Taylor (1991). Central Mississippi Valley Earthquake Bulletin, Quarterly Bulletin No. 67, Appendix, St. Louis University.
- Sexton, J.L., L.W. Braile, W.J. Hinze, and M.J. Campbell (1986). Seismic reflection profiling studies of a buried Precambrian rift beneath the Wabash Valley fault zone, *Geophysics*, **51**, 640-660.
- Shapiro, A. (1988). Rg waves from rockbursts in South Africa, *Tectonophysics*, **156**, 367-273.
- Taylor, K. (1991). Seismotectonics of the Illinois Basin and the northern half of the Ozark Uplift, *Ph.D. Dissert.*, St. Louis University, St. Louis, MO.
- Taylor, K.B., R.B. Herrmann, M.W. Hamburger, G.L. Pavlis, A. Johnston, C. Langer, and C. Lam (1989). The southeastern Illinois earthquake of 10 June 1987, *Seism. Res. Letters*, **60**, 101-110.
- Taylor, S.R., M.D. Denny, E.S. Vergino, and R.E. Glaser (1989). Regional discrimination between NTS explosions and western U.S. earthquakes, *Bull. Seism. Soc. Am.*, **79**, 1142-1176.
- Walter, W.R and K.F. Priestly (1991). High-frequency P wave spectra from explosions and earthquakes, in, Taylor, S.R., H.J. Patton, and P.G. Richards, *Explosion Source Phenomenology*, Geophysical Monograph 65, Am. Geophys. Union, 219-228.
- Willman, H.B. and J.C. Frye (1970). Loess thickness in Illinois, Illinois State Geological Survey (map).

(This Page Blank)

DISCOURSE ON THE USE OF SHORT PERIOD SURFACE WAVES AS A DEPTH DISCRIMINANT

R.B. Herrmann

ABSTRACT

Consideration of the usefulness of short-period surface wave recordings in a regional discrimination environment is presented. These signals are not evidence of an explosion, but rather of shallow source depth. If independent estimates of the event seismic moment are available, the presence or absence of a short-period recording can be used as a depth constraint on the event, which of itself may be a strong discriminant.

INTRODUCTION

It is accepted that the observation of a short period surface wave is an indication of a shallow source depth. This general statement is based on numerous observations of mining activity which produce the characteristic short period surface waves seen on seismograms. The theoretical basis lies in the fact that the surface wave excitation can be related to the product of an eigenfunction sampled at source depth and another at receiver depth divided by a depth integral of an eigenfunction squared. Since short period surface wave eigenfunctions do not penetrate very deep, the surface wave recorded at the surface and generated by a shallow source will be significantly larger than one generated by a deeper source (Tsai and Aki, 1969; Herrmann, 1974).

This observation is typically used by regional seismologists to classify events as not being earthquakes. The strong assumption is that shallow earthquakes either do not occur, or have sufficient signal complexity to overwhelm the coherent short period surface wave. This is not always true.

Figure 1 presents WWSSN long-period recordings of a small, $m_{bLg} = 3.8$, earthquake that occurred near Cairo, Illinois on August 14, 1965 (Herrmann and Nuttli, 1975). This earthquake was only felt over a short distance of 15 km, but did cause intensity VII damage (Nuttli and Zollweg, 1974) and led to Nuttli's (1973) development of the m_{bLg} magnitude scale. This was an earthquake since no large coal strip mines were nearby which would have shot off greater than 100 tons of explosive. This earthquake did generate observable surface waves on long period WWSSN seismographs 1400 km away (Herrmann, 1974) and analysis yielded strike-slip focal mechanism, seismic moment of $2.9 \cdot 10^{21}$ dyne-cm and a depth of 1.5 km (Herrmann, 1979).

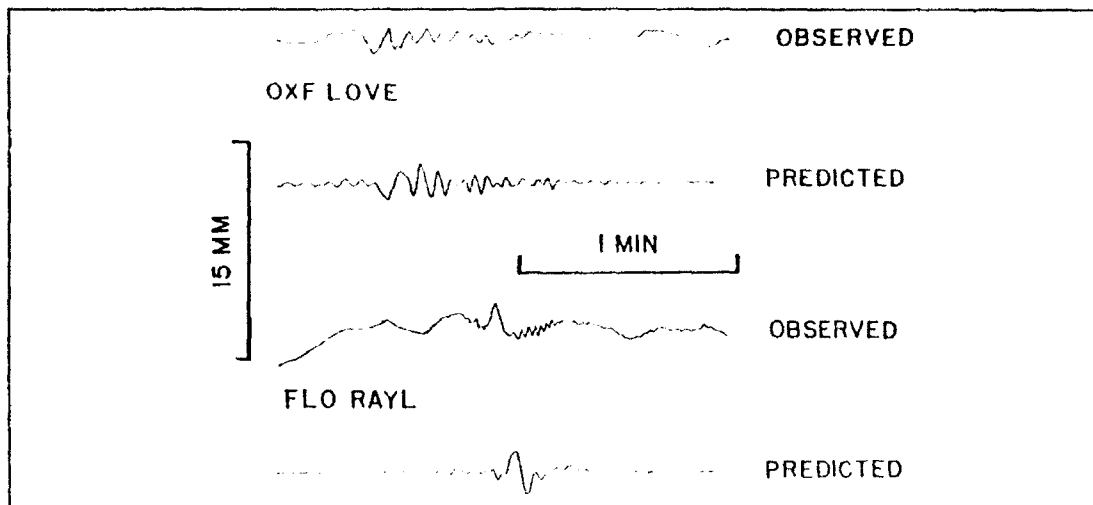


Fig. 1. Comparison of observed and predicted waveforms recorded on the OXF and FLO long-period instruments for the August 14, 1965 earthquake. The stations are 300 and 200 km, respectively, from the source. The 15-100 WWSSN LP seismographs had gains of 3.0K.

We conclude that shallow earthquakes can also generate short period surface waves that can be observed at regional distances. Hence one must be cautious about their use as an event type discriminant.

Another statement made concerning regional recordings is that there is little value in studying the short-period surface wave since it does not propagate to large distances. The previous example implies that under proper conditions of correct recording instrument and band and with a relatively uniform waveguide, as in the central United States, these waves can be observed.

If this is the case, then can they be useful for the discrimination problem?

DEPTH CONSTRAINTS

The key point is that the presence short-period surface wave is a source depth indicator and not a source classifier. In a discrimination context, if it can be shown that an event is greater than 3 km, perhaps, then the event is most likely not an explosion. The event can then be confidently identified as an earthquake and eliminated from further consideration. In the today's environment of automatic event location and classification, it would be interesting to consider how surface wave information can be incorporated.

The first step is to generate synthetic surface-wave seismograms for point earthquake and explosion sources as a function of source depth. The ground motions generated can then be passed through different instruments

and a peak recorded amplitude read off. The WWSSN short- and long-period responses are used in this example. Table 1 presents the crustal model used. This model is one that the author has used for synthetic seismogram program development and describes P-wave first arrivals and long-period surface-wave dispersion in the central U. S. well. The upper kilometer is assumed representative of the Paleozoic sedimentary section in the mid-continent.

Table 1
Central U. S. Earth Model

H (km)	V _P (km/s)	V _S (km/s)	ρ (gm/cm ³)	Q _P	Q _S
1	5.00	2.89	2.50	200	100
9	6.10	3.52	2.70	1200	600
10	6.40	3.70	2.90	1200	600
20	6.70	3.87	3.00	8000	4000
	8.15	4.70	3.40	8000	4000

Synthetic seismograms were generated at distances of 100 and 1000 km for a point explosion and for a strike-slip earthquake source observed at an azimuth of 22° from strike. The source time function had a duration of 0.4 seconds, which would not affect the long period recordings. It also should not affect the 1 Hz surface wave on the short period instrument. The duration may also be typical of an event with seismic moment of 10²² dyne-cm.

To present the results of the computations in a form useful for discrimination studies, a plot is made of the seismic moment required to produce a threshold amplitude on the seismogram for the event depth. This threshold is taken to be 0.1 cm, which is the limit of what can be seen and measured on photographic seismograms. Figure 2 presents such information. Figure 2a is for the long-period instrument and Figure 2b is for the short period instrument. The striking feature is that the explosion and strike-slip earthquake give identical observed amplitudes at shallow depth. Beneath the Paleozoic layer, differences are seen, with the explosion generating smaller surface waves.

These figures can be used very simply if the event's seismic moment is known. If the observed amplitude is greater than the threshold, then its depth must be to the left of the curve; if the signal is not observed, then the depth is in the region to the right of the curve. This is a simple binary decision. Changing the threshold will only change the set of master curves. To account for unknowns in the earth model, a suite of curves could be

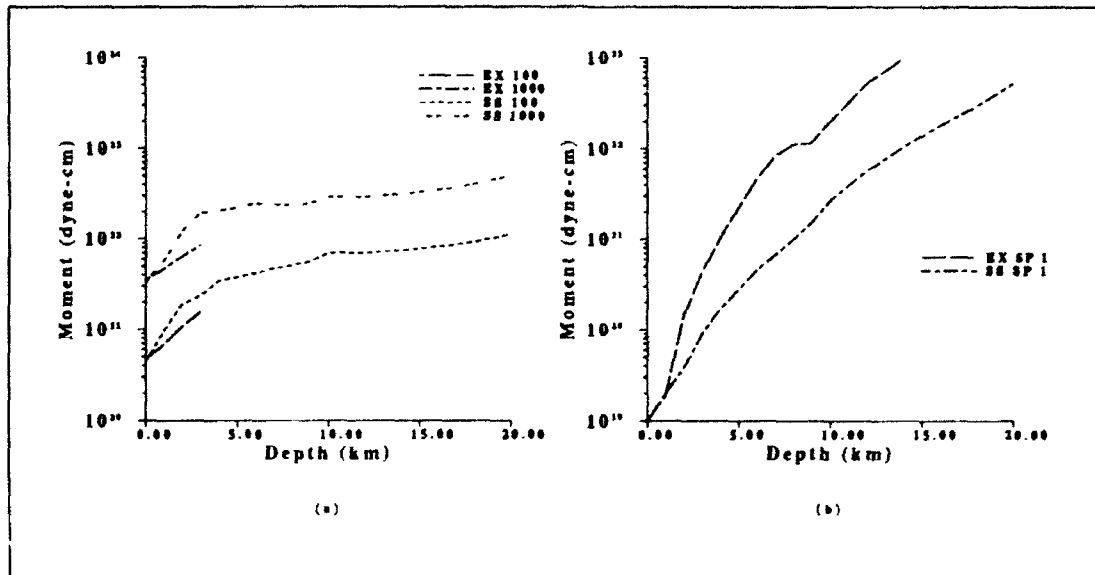


Fig. 2. (a) Plot of moment required to exceed a recorded surface-wave amplitude of 0.1 cm on a 1.5K 15-100 vertical component WWSSN LP seismograph at distances of 100 and 1000 km, and for explosion, EX, and vertical strike-slip, SS, sources. The receiver azimuth from the strike-slip source is 22.5° from strike.

(b) Plot of moment required to exceed a recorded surface-wave amplitude of 0.1 cm on a 50K vertical component WWSSN SP seismograph at a distance of 100 km, and for explosion, EX, and vertical strike-slip, SS, sources. The receiver azimuth from the strike-slip source is 22.5° from strike.

generated. This would lead to a distribution in possible depth for a given seismic moment. The absence of a signal at the threshold, perhaps due to its being obscured by noise, could then be assigned a conditional probability that its depth is greater than a certain value. The same distribution could be used with an actual observed amplitude to assign a depth through another set of curves. When combined with some *a priori* statement that an event with depth greater than 3 km, for example, is not an explosion, then the result would be a likelihood that the event is not an explosion.

DISCUSSION

This simple use of master curves shows how short period surface wave observations could be used to quantify depth estimates. The requirements are as follow:

- a) the regional surface-wave propagation characteristics are known, e.g., the crustal velocity and Q model is known.

- b) there is an independent estimate of the seismic source size, e.g., a moment-magnitude relationship.

The construction of master curves is simple with existing code. The incorporation of this technique into a rules based depth classification process is not too difficult.

Figure 2a indicates that it will be difficult to distinguish between shallow explosions and earthquakes on the basis of long period recordings. This permits an indirect thought experiment to tie an explosion yield to an m_{Lg} value for a small event. Herrmann et al (1992) analyzed a large number of 1 ton point chemical explosions and found that the isotropic moment was roughly $2 \cdot 10^{18}$ dyne-cm. Denny and Johnson (1991) proposed a one-to-one relation between seismic moment and yield. Thus the seismic moment for the August 14, 1965 event would be indicative of a 1 kT event. It is interesting, coincidental and certainly not well understood, that the assigned $m_{bLg} = 3.8$ number is roughly within the proper range for a 1 kT nuclear explosion. Thus one should be able to observe not only Lg but also surface waves from such a nuclear event in at regional distances.

There is another aspect to 1 kT explosions. They should be well observed in the 4 - 40 second period band if the upper crust is fairly uniform. Thus an examination of radiation patterns of the Love and Rayleigh waves would be able to distinguish the explosion from the earthquake. Thus may be the threshold for doing this because of reduced S/N for smaller events due to the presence of microseisms.

REFERENCES

- Denny, M. D., and L. R. Johnson (1991). The explosion seismic source function: models and scaling laws reviewed, in *Explosion Source Phenomenology*, S. R. Taylor, H. J. Patton and P. G. Richards (eds), American Geophysical Union, Washington, 268 pp.
- Herrmann, R. B. (1974). Surface wave generation by central united States earthquakes, *Ph. D. Dissert.*, Saint Louis University, 263 pp.
- Herrmann, R. B. (1979). Surface wave focal mechanisms for eastern North American earthquakes with tectonic implications, *J. Geophys. Res.* **84**, 3543-3552.
- Herrmann, R. B., and O. W. Nuttli (1975). Ground motion modeling in a continental interior, I. Theory and observations, *International Journal of Earthquake Engineering and Structural Dynamics* **4**, 49-58.

- Herrmann, R. B., G. Al-Eqabi, and K. Hutchensen (1992). Isotropic moment-yield relations for small chemical explosions, in *Quantification of $m_{I,2}$ for small explosions*, Scientific Report No. 1, PL-TR-92-2109, Phillips Laboratory, Air Force Systems Command, Hanscom Air Force Base, Massachusetts, 47 pp. ADA253915
- Nuttli, O. W. (1973). Seismic wave attenuation and magnitude relations for eastern North America, *J. Geophys. Res.* **78**, 876-885.
- Nuttli, O. W., and J. E. Zollweg (1974). The relation between felt area and magnitude for central United States earthquakes, *Bull. Seism. Soc. Am.* **64**, 73-85.
- Tsai, Y. B., and K. Aki (1970). Precise focal depth determination from amplitude spectra of surface waves, *J. Geophys. Res.* **75**, 5729-5743.

Prof. Thomas Ahrens
Seismological Lab, 252-21
Division of Geological & Planetary Sciences
California Institute of Technology
Pasadena, CA 91125

Prof. Keiiti Aki
Center for Earth Sciences
University of Southern California
University Park
Los Angeles, CA 90089-0741

Prof. Shelton Alexander
Geosciences Department
403 Deike Building
The Pennsylvania State University
University Park, PA 16802

Dr. Ralph Alewine, III
DARPA/NMRO
3701 North Fairfax Drive
Arlington, VA 22203-1714

Prof. Charles B. Archambeau
CIRES
University of Colorado
Boulder, CO 80309

Dr. Thomas C. Bache, Jr.
Science Applications Int'l Corp.
10260 Campus Point Drive
San Diego, CA 92121 (2 copies)

Prof. Muawia Barazangi
Institute for the Study of the Continent
Cornell University
Ithaca, NY 14853

Dr. Jeff Barker
Department of Geological Sciences
State University of New York
at Binghamton
Vestal, NY 13901

Dr. Douglas R. Baumgardt
ENSCO, Inc
5400 Port Royal Road
Springfield, VA 22151-2388

Dr. Susan Beck
Department of Geosciences
Building #77
University of Arizona
Tucson, AZ 85721

Dr. T.J. Bennett
S-CUBED
A Division of Maxwell Laboratories
11800 Sunrise Valley Drive, Suite 1212
Reston, VA 22091

Dr. Robert Blandford
AFTAC/IT, Center for Seismic Studies
1300 North 17th Street
Suite 1450
Arlington, VA 22209-2308

Dr. Stephen Bratt
Center for Seismic Studies
1300 North 17th Street
Suite 1450
Arlington, VA 22209-2308

Dr. Lawrence Burdick
IGPP, A-025
Scripps Institute of Oceanography
University of California, San Diego
La Jolla, CA 92093

Dr. Robert Burrige
Schlumberger-Doll Research Center
Old Quarry Road
Ridgefield, CT 06877

Dr. Jerry Carter
Center for Seismic Studies
1300 North 17th Street
Suite 1450
Arlington, VA 22209-2308

Dr. Eric Chael
Division 9241
Sandia Laboratory
Albuquerque, NM 87185

Dr. Martin Chapman
Department of Geological Sciences
Virginia Polytechnical Institute
21044 Derring Hall
Blacksburg, VA 24061

Prof. Vernon F. Cormier
Department of Geology & Geophysics
U-45, Room 207
University of Connecticut
Storrs, CT 06268

Prof. Steven Day
Department of Geological Sciences
San Diego State University
San Diego, CA 92182

Marvin Denny
U.S. Department of Energy
Office of Arms Control
Washington, DC 20585

Dr. Zoltan Der
ENSCO, Inc.
5400 Port Royal Road
Springfield, VA 22151-2388

Prof. Adam Dziewonski
Hoffman Laboratory, Harvard University
Dept. of Earth Atmos. & Planetary Sciences
20 Oxford Street
Cambridge, MA 02138

Prof. John Ebel
Department of Geology & Geophysics
Boston College
Chestnut Hill, MA 02167

Eric Fielding
SNEE Hall
INSTOC
Cornell University
Ithaca, NY 14853

Dr. Mark D. Fisk
Mission Research Corporation
735 State Street
P.O. Drawer 719
Santa Barbara, CA 93102

Prof Stanley Flatte
Applied Sciences Building
University of California, Santa Cruz
Santa Cruz, CA 95064

Dr. John Foley
NER-Geo Sciences
1100 Crown Colony Drive
Quincy, MA 02169

Prof. Donald Forsyth
Department of Geological Sciences
Brown University
Providence, RI 02912

Dr. Art Frankel
U.S. Geological Survey
922 National Center
Reston, VA 22092

Dr. Cliff Frolich
Institute of Geophysics
8701 North Mopac
Austin, TX 78759

Dr. Holly Given
IGPP, A-025
Scripps Institute of Oceanography
University of California, San Diego
La Jolla, CA 92093

Dr. Jeffrey W. Given
SAIC
10260 Campus Point Drive
San Diego, CA 92121

Dr. Dale Glover
Defense Intelligence Agency
ATTN: ODT-1B
Washington, DC 20301

Dr. Indra Gupta
Teledyne Geotech
314 Montgomery Street
Alexandria, VA 22314

Dan N. Hagedorn
Pacific Northwest Laboratories
Battelle Boulevard
Richland, WA 99352

Dr. James Hannon
Lawrence Livermore National Laboratory
P.O. Box 808
L-205
Livermore, CA 94550

Dr. Roger Hansen
HQ AFTAC/TTR
130 South Highway A1A
Patrick AFB, FL 32925-3002

Prof. David G. Harkrider
Seismological Laboratory
Division of Geological & Planetary Sciences
California Institute of Technology
Pasadena, CA 91125

Prof. Danny Harvey
CIRES
University of Colorado
Boulder, CO 80309

Prof. Donald V. Helmberger
Seismological Laboratory
Division of Geological & Planetary Sciences
California Institute of Technology
Pasadena, CA 91125

Prof. Eugene Herrin
Institute for the Study of Earth and Man
Geophysical Laboratory
Southern Methodist University
Dallas, TX 75275

Prof. Robert B. Herrmann
Department of Earth & Atmospheric Sciences
St. Louis University
St. Louis, MO 63156

Prof. Lane R. Johnson
Seismographic Station
University of California
Berkeley, CA 94720

Prof. Thomas H. Jordan
Department of Earth, Atmospheric &
Planetary Sciences
Massachusetts Institute of Technology
Cambridge, MA 02139

Prof. Alan Kafka
Department of Geology & Geophysics
Boston College
Chestnut Hill, MA 02167

Robert C. Kemerait
ENSCO, Inc.
445 Pineda Court
Melbourne, FL 32940

Dr. Karl Koch
Institute for the Study of Earth and Man
Geophysical Laboratory
Southern Methodist University
Dallas, Tx 75275

Dr. Max Koontz
U.S. Dept. of Energy/DP 5
Forrestal Building
1000 Independence Avenue
Washington, DC 20585

Dr. Richard LaCoss
MIT Lincoln Laboratory, M-200B
P.O. Box 73
Lexington, MA 02173-0073

Dr. Fred K. Lamb
University of Illinois at Urbana-Champaign
Department of Physics
1110 West Green Street
Urbana, IL 61801

Prof. Charles A. Langston
Geosciences Department
403 Deike Building
The Pennsylvania State University
University Park, PA 16802

Jim Lawson, Chief Geophysicist
Oklahoma Geological Survey
Oklahoma Geophysical Observatory
P.O. Box 8
Leonard, OK 74043-0008

Prof. Thorne Lay
Institute of Tectonics
Earth Science Board
University of California, Santa Cruz
Santa Cruz, CA 95064

Dr. William Leith
U.S. Geological Survey
Mail Stop 928
Reston, VA 22092

Mr. James F. Lewkowicz
Phillips Laboratory/GPEH
29 Randolph Road
Hanscom AFB, MA 01731-3010 (2 copies)

Mr. Alfred Lieberman
ACDA/VI-OA State Department Building
Room 5726
320-21st Street, NW
Washington, DC 20451

Prof. L. Timothy Long
School of Geophysical Sciences
Georgia Institute of Technology
Atlanta, GA 30332

Dr. Randolph Martin, III
New England Research, Inc.
76 Olcott Drive
White River Junction, VT 05001

Dr. Robert Masse
Denver Federal Building
Box 25046, Mail Stop 967
Denver, CO 80225

Dr. Gary McCartor
Department of Physics
Southern Methodist University
Dallas, TX 75275

Prof. Thomas V. McEvilly
Seismographic Station
University of California
Berkeley, CA 94720

Dr. Art McGarr
U.S. Geological Survey
Mail Stop 977
U.S. Geological Survey
Menlo Park, CA 94025

Dr. Keith L. McLaughlin
S-CUBED
A Division of Maxwell Laboratory
P.O. Box 1620
La Jolla, CA 92038-1620

Stephen Miller & Dr. Alexander Florence
SRI International
333 Ravenswood Avenue
Box AF 116
Menlo Park, CA 94025-3493

Prof. Bernard Minster
IGPP, A-025
Scripps Institute of Oceanography
University of California, San Diego
La Jolla, CA 92093

Prof. Brian J. Mitchell
Department of Earth & Atmospheric Sciences
St. Louis University
St. Louis, MO 63156

Mr. Jack Murphy
S-CUBED
A Division of Maxwell Laboratory
11800 Sunrise Valley Drive, Suite 1212
Reston, VA 22091 (2 Copies)

Dr. Keith K. Nakanishi
Lawrence Livermore National Laboratory
L-025
P.O. Box 808
Livermore, CA 94550

Dr. Carl Newton
Los Alamos National Laboratory
P.O. Box 1663
Mail Stop C335, Group ESS-3
Los Alamos, NM 87545

Dr. Bao Nguyen
HQ AFTAC/TTR
130 South Highway A1A
Patrick AFB, FL 32925-3002

Prof. John A. Orcutt
IGPP, A-025
Scripps Institute of Oceanography
University of California, San Diego
La Jolla, CA 92093

Prof. Jeffrey Park
Kline Geology Laboratory
P.O. Box 6666
New Haven, CT 06511-8130

Dr. Howard Patton
Lawrence Livermore National Laboratory
L-025
P.O. Box 808
Livermore, CA 94550

Dr. Frank Pilotte
HQ AFTAC/TT
130 South Highway A1A
Patrick AFB, FL 32925-3002

Dr. Jay J. Pulli
Radix Systems, Inc.
201 Perry Parkway
Gaithersburg, MD 20877

Dr. Robert Reinke
ATTN: FCTVTD
Field Command
Defense Nuclear Agency
Kirtland AFB, NM 87115

Prof. Paul G. Richards
Lamont-Doherty Geological Observatory
of Columbia University
Palisades, NY 10964

Mr. Wilmer Rivers
Teledyne Geotech
314 Montgomery Street
Alexandria, VA 22314

Dr. George Rothe
HQ AFTAC/TTR
130 South Highway A1A
Patrick AFB, FL 32925-3002

Dr. Alan S. Ryall, Jr.
DARPA/NMRO
3701 North Fairfax Drive
Arlington, VA 22209-1714

Dr. Richard Sailor
TASC, Inc.
55 Walkers Brook Drive
Reading, MA 01867

Prof. Charles G. Sammis
Center for Earth Sciences
University of Southern California
University Park
Los Angeles, CA 90089-0741

Prof. Christopher H. Scholz
Lamont-Doherty Geological Observatory
of Columbia University
Palisades, NY 10964

Dr. Susan Schwartz
Institute of Tectonics
1156 High Street
Santa Cruz, CA 95064

Secretary of the Air Force
(SAFRD)
Washington, DC 20330

Office of the Secretary of Defense
DDR&E
Washington, DC 20330

Thomas J. Sereno, Jr.
Science Application Int'l Corp.
10260 Campus Point Drive
San Diego, CA 92121

Dr. Michael Shore
Defense Nuclear Agency/SPSS
6801 Telegraph Road
Alexandria, VA 22310

Dr. Robert Shumway
University of California Davis
Division of Statistics
Davis, CA 95616

Dr. Matthew Sibol
Virginia Tech
Seismological Observatory
4044 Derring Hall
Blacksburg, VA 24061-0420

Prof. David G. Simpson
IRIS, Inc.
1616 North Fort Myer Drive
Suite 1050
Arlington, VA 22209

Donald L. Springer
Lawrence Livermore National Laboratory
L-025
P.O. Box 808
Livermore, CA 94550

Dr. Jeffrey Stevens
S-CUBED
A Division of Maxwell Laboratory
P.O. Box 1620
La Jolla, CA 92038-1620

Lt. Col. Jim Stobie
ATTN: AFOSR/NL
110 Duncan Avenue
Bolling AFB
Washington, DC 20332-0001

Prof. Brian Stump
Institute for the Study of Earth & Man
Geophysical Laboratory
Southern Methodist University
Dallas, TX 75275

Prof. Jeremiah Sullivan
University of Illinois at Urbana-Champaign
Department of Physics
1110 West Green Street
Urbana, IL 61801

Prof. L. Sykes
Lamont-Doherty Geological Observatory
of Columbia University
Palisades, NY 10964

Dr. David Taylor
ENSCO, Inc.
445 Pineda Court
Melbourne, FL 32940

Dr. Steven R. Taylor
Los Alamos National Laboratory
P.O. Box 1663
Mail Stop C335
Los Alamos, NM 87545

Prof. Clifford Thurber
University of Wisconsin-Madison
Department of Geology & Geophysics
1215 West Dayton Street
Madison, WI 53706

Prof. M. Nafi Toksoz
Earth Resources Lab
Massachusetts Institute of Technology
42 Carleton Street
Cambridge, MA 02142

Dr. Larry Turnbull
CIA-OSWR/NED
Washington, DC 20505

Dr. Gregory van der Vink
IRIS, Inc.
1616 North Fort Myer Drive
Suite 1050
Arlington, VA 22209

Dr. Karl Veith
EG&G
5211 Auth Road
Suite 240
Suitland, MD 20746

Prof. Terry C. Wallace
Department of Geosciences
Building #77
University of Arizona
Tucson, AZ 85721

Dr. Thomas Weaver
Los Alamos National Laboratory
P.O. Box 1663
Mail Stop C335
Los Alamos, NM 87545

Dr. William Wortman
Mission Research Corporation
8560 Cinderbed Road
Suite 700
Newington, VA 22122

Prof. Francis T. Wu
Department of Geological Sciences
State University of New York
at Binghamton
Vestal, NY 13901

AFTAC/CA
(STINFO)
Patrick AFB, FL 32925-6001

DARPA/PM
3701 North Fairfax Drive
Arlington, VA 22203-1714

DARPA/RMO/RETRIEVAL
3701 North Fairfax Drive
Arlington, VA 22203-1714

DARPA/RMO/SECURITY OFFICE
3701 North Fairfax Drive
Arlington, VA 22203-1714

HQ DNA
ATTN: Technical Library
Washington, DC 20305

Defense Intelligence Agency
Directorate for Scientific & Technical Intelligence
ATTN: DTIB
Washington, DC 20340-6158

Defense Technical Information Center
Cameron Station
Alexandria, VA 22314 (2 Copies)

TACTEC
Battelle Memorial Institute
505 King Avenue
Columbus, OH 43201 (Final Report)

Phillips Laboratory
ATTN: XPG
29 Randolph Road
Hanscom AFB, MA 01731-3010

Phillips Laboratory
ATTN: GPE
29 Randolph Road
Hanscom AFB, MA 01731-3010

Phillips Laboratory
ATTN: TSML
5 Wright Street
Hanscom AFB, MA 01731-3004

Phillips Laboratory
ATTN: PL/SUL
3550 Aberdeen Ave SE
Kirtland, NM 87117-5776 (2 copies)

Dr. Svein Mykkeltveit
NTNT/NORSAR
P.O. Box 51
N 2007 Kjeller, NORWAY (3 Copies)

Dr. Michel Bouchon
I.R.I.G.M.-B.P. 68
38402 St. Martin D'Herès
Cedex, FRANCE

Prof. Keith Priestley
University of Cambridge
Bullard Labs, Dept. of Earth Sciences
Madingley Rise, Madingley Road
Cambridge CB3 0EZ, ENGLAND

Dr. Michel Campillo
Observatoire de Grenoble
I.R.I.G.M.-B.P. 53
38041 Grenoble, FRANCE

Dr. Jorg Schlittenhardt
Federal Institute for Geosciences & Nat'l Res.
Postfach 510153
D-3000 Hannover 51, GERMANY

Dr. Kin Yip Chun
Geophysics Division
Physics Department
University of Toronto
Ontario, CANADA

Dr. Johannes Schweitzer
Institute of Geophysics
Ruhr University/Bochum
P.O. Box 1102148
4360 Bochum 1, GERMANY

Prof. Hans-Peter Harjes
Institute for Geophysics
Ruhr University/Bochum
P.O. Box 102148
4630 Bochum 1, GERMANY

Trust & Verify
VERTIC
8 John Adam Street
London WC2N 6EZ, ENGLAND

Prof. Eystein Husebye
NTNF/NORSAR
P.O. Box 51
N-2007 Kjeller, NORWAY

David Jepsen
Acting Head, Nuclear Monitoring Section
Bureau of Mineral Resources
Geology and Geophysics
G.P.O. Box 378, Canberra, AUSTRALIA

Ms. Eva Johannisson
Senior Research Officer
FOA
S-172 90 Sundbyberg, SWEDEN

Dr. Peter Marshall
Procurement Executive
Ministry of Defense
Blacknest, Brimpton
Reading FG7-FRS, UNITED KINGDOM

Dr. Bernard Massinon, Dr. Pierre Mechler
Societe Radiomana
27 rue Claude Bernard
75005 Paris, FRANCE (2 Copies)